Hydrodynamic Interactions in Salmonid Redds: Hyporheic Exchange Drivers and Embryo Habitat Optimization

A Dissertation

Presented in Partial Fulfillment of the Requirements for the

Degree of Doctor of Philosophy

with a

Major in Mechanical Engineering

in the

College of Graduate Studies

University of Idaho

by

Bishal Bhattarai

Approved by:

Major Professor: Tao Xing, Ph.D., P.E.

Committee Members: Ralph Budwig, Ph.D., P.E.; Daniele Tonina, Ph.D., P.E.;

William Reeder, Ph.D.

Department Administrator: Eric Wolbrecht, Ph.D., P.E.

December 2023

Abstract

Salmonids are known for their spawning behaviors, which involve creating dune-shaped egg nests called redds in streambed gravel. The survival of salmon embryos critically dependents on downwelling oxygen-rich stream water fluxes, which are influenced by a confluence of factors, including the redd's morphology, stream hydraulics, and hydraulic conductivity of the redd sediment (K). Our investigation encompasses three major aspects: (1) the impact of stream discharge and redd geometry on downwelling fluxes, (2) the influence of bed roughness, egg pocket location, and egg pocket permeability on the hyporheic flows, and (3) the evaluation of various Reynolds-Averaged Navier-Stokes (RANS) turbulence closures for accurately simulating the complex open channel flows over redds. To achieve this, we simulated the surface and subsurface flows with numerical hydraulic models linked through the near-bed pressure distribution quantified using a two-phase (air-water) two-dimensional surface water computational fluid dynamics (CFD) model, validated with experiments.

In the first part, we hypothesized that downwelling fluxes in the redds are influenced by stream discharge and the redd aspect ratio ($A_R = A/L$, with A, the redd amplitude and L, its length). We examined five different redd sizes ranging from ~1 to ~4 m long under varying discharge conditions, from shallow (0.1 m) and slow (0.15 m/s) to deep (8m) and fast (3.3 m/s). Our results confirmed that downwelling fluxes increase with discharge and A_R, due to the increased near-bed head gradient over the redd. Additionally, we proposed a regression equation involving stream flow Reynolds (Re) and Froude (Fr) numbers and A_R to predict these downwelling fluxes, which may help evaluate the impact of regulated and unregulated flows on hyporheic flows during embryo incubation.

In the second part, we addressed how salmon spawning activities, which alter streambed morphology to form redds, impact hyporheic fluxes. We examined the effects of streambed roughness, egg pocket permeability, and their location within the redd on the downwelling flows in egg pockets (q_{ep}). Our results indicated that the dimensionless flux into the egg pocket, $\bar{q}^*_{ep} = \frac{\bar{q}_{ep}}{K_D}$ increases noticeably with the downstream distance of egg pockets from the redd pit, and less strongly with $K_{EP}{}^* = \frac{K_{EP}}{K_D}$. The near-surface downwelling fluxes significantly increase with vertical roughness scaling (R_1), but minimally when the roughness is scaled both vertically and horizontally (R_2). This study suggests that the typical simplification of a smooth redd surface with uniform hydraulic conductivity is a valid approximation for predicting interstitial flows within redds.

The third part of our study evaluates the performance of various RANS turbulence models in simulating complex open channel flows over the redds. The models tested include the standard k–ω, SST k–ω, and realizable k–ε, as well as different wall treatments for the realizable k–ε model. Our analysis reveals that while all models capture the bulk flow characteristics, there are substantial differences in their precision for specific flow features. The realizable k-ε model, particularly with standard wall function and mesh resolving the viscous sublayer, excels in predicting near-wall flow separations and velocity fields, and the SST k–ω model provides best predictions of turbulent kinetic energy but tends to overestimate separation vortex magnitudes. This study highlights the variability in accuracy among turbulence models, emphasizing the need for careful model selection based on specific prediction regions.

Acknowledgments

I extend my sincerest gratitude to my major professor, Dr. Tao Xing, and committee members, Drs. Daniele Tonina, Ralph Budwig, and William Reeder, for their invaluable guidance and unwavering support throughout this research. Their expertise, encouragement, and critical insights have been instrumental in shaping the direction of my work and pushing me to achieve my full potential. I am immensely grateful for the invaluable intellectual contributions and guidance each of them provided. I also appreciate the collaborative efforts, discussions, and ideas of my colleague, Brandon Hilliard, that have significantly contributed to the development of this research.

I would also like to express my gratitude to the University of Idaho's Mechanical Engineering Department and the Center for Ecohydraulics Research for giving me this opportunity to work in this project, as well as to the California Water Board and the National Science Foundation for their financial support. Their assistance greatly contributed to my progress in the program and provided me with the necessary resources to pursue this research.

Dedication

To my loving parents, whose unwavering love and support have been a constant source of

strength and inspiration, I am forever thankful.

Table of Contents

List of Tables

List of Figures

Statement of Contribution

Author Contributions in the Published Works:

Conceptualization: Bishal Bhattarai, Benjamin T. Martin, Tao Xing, Daniele Tonina

Formal analysis: Bishal Bhattarai, Tao Xing, Daniele Tonina

Funding acquisition: Daniele Tonina

Methodology: Bishal Bhattarai, Tao Xing, Daniele Tonina

Project Administration: Benjamin T. Martin, Daniele Tonina

Resources: Benjamin T. Martin, Tao Xing

Software: Tao Xing

Supervision: Tao Xing, Ralph Budwig, Daniele Tonina

Validation: Bishal Bhattarai, Brandon Hilliard, William J. Reeder, Ralph Budwig, Tao Xing, Daniele Tonina

Visualization: Bishal Bhattarai, Brandon Hilliard

Writing- original draft: Bishal Bhattarai, Daniele Tonina

Writing- review & editing: Bishal Bhattarai, Brandon Hilliard, William J. Reeder, Ralph Budwig, Benjamin T. Martin, Tao Xing, Daniele Tonina

Nomenclature

L	Wavelength of redd (m)
A	Amplitude of redd (m)
A_R	Redd Aspect Ratio, $A_R = \frac{A}{L}$
K	Hydraulic conductivity of redd sediment (m/s)
K_D	Disturbed bed hydraulic conductivity
K_{UD}	Undisturbed bed hydraulic conductivity
K_{EP}	Egg pocket hydraulic conductivity
k	Permeability (m^2)
P	Pressure (Pa)
γ	Specific weight of water, $\gamma = \rho g$ (N/m^3)
μ	Dynamic viscosity (kg/m-s)
ρ	Density of water (kg/m^3)
g	Acceleration due to gravity (m/s^2)
Re	Reynolds number, $Re = \frac{v \cdot Y_0}{L}$
Fr	Froude number, $Fr = \frac{v}{\sqrt{g \cdot Y_0}}$
$\frac{A}{Y_0}$	Redd relative submergence

Y_0 — Water depth (m)

H_R — Relative total head, $H_R = H - (Y_0 + z)$ (m)

z — Difference between local streambed and the datum, sloped at same angle

ΔH_R — Redd induced relative total head drop (m)

$$\Delta H_R = H_{R,H} - H_{R,L}$$

$H_{R,H}$ & $H_{R,L}$ — Maximum and minimum relative total heads over redd

WSE_R — Relative water surface elevation (m)

H^* — Relative total head gradient, $H^* = \frac{\Delta H_R}{L}$

V_x — Streamwise velocity (m/s)

V_y — Vertical velocity (m/s)

V_s — Simulated velocity (m/s)

V_o — Observed velocity (m/s)

r_G — Grid refinement ratio, $r_G = \frac{\Delta x_2}{\Delta x_1} = \frac{\Delta x_3}{\Delta x_2}$, Δx is the grid distance between two elements and the subscripts 1, 2, and 3 represent the fine, medium, and coarse meshes, respectively.

R_G — Convergence ratio

P_G — Observed order of accuracy.

U_G	Numerical uncertainty estimate
$\lvert E \rvert$	Absolute relative error between the fine mesh and the experimental data, $\lvert E \rvert = \lvert S - D \rvert$
U_V	Validation uncertainty, $U_V = \sqrt{U_G^2 + U_D^2}$
q	Normal downwelling velocity (m/s)
q^*	Normal downwelling velocity normalized by its maximum value, $q^* = \dfrac{q}{q_{max}}$
$\bar{q}_d$	Averaged downwelling velocity over the entire redd
$\bar{q}_d^*$	$\dfrac{\bar{q}_d}{K}$
$\bar{q}_{d,ep}$	Averaged downwelling velocity over the portion that delivers water to the egg pocket (m/s)
$\bar{q}_{d,ep}^*$	$\dfrac{\bar{q}_{d,ep}}{K}$
x^*	Dimensionless distance, $x^* = \dfrac{x}{L}$
$\bar{q}_{ep}$	Mean spatial flux entering the egg pocket (m/s)
$\bar{q}^*{}_{ep} = \dfrac{\bar{q}_{ep}}{K_D}$	Dimensionless mean flux entering an egg pocket
$\bar{q}_{d,2d,ep}$	Mean spatial downwelling fluxes over the surfaces located at a depth two times the D_{50} of roughness ($\sigma_E = 13.3\ mm$) value below the redd surface

$\bar{q}_{d,3d,ep}$ Mean spatial downwelling fluxes over the surfaces located at a depth

three times the D_{50} of roughness ($\sigma_E = 13.3 \ mm$) value below the

redd surface

$\bar{q}_d^* = \dfrac{\bar{q}_d}{K_D}$ Dimensionless downwelling mean flux over the entire redd

$\bar{q}_{d,ep}^* = \dfrac{\bar{q}_{d,ep}}{K_D}$ Dimensionless downwelling mean flux toward the egg pockets at the

water-sediment interface

$\bar{q}_{d,2d,ep}^* = \dfrac{\bar{q}_{d,2d,ep}}{K_D}$ Dimensionless downwelling mean flux toward the egg pockets at a

surface located 2 times the median grain size below the streambed

location

$\bar{q}_{d,3d,ep}^* = \dfrac{\bar{q}_{d,3d,ep}}{K_D}$ Dimensionless downwelling mean flux toward the egg pockets at a

surface located 3 times the median grain size below the streambed

location

Chapter 1: Effect of Surface Hydraulics and Salmon Redd Size on Redd-Induced Hyporheic Exchange

1.1 Introduction

Salmon females bury their eggs in streambed gravel, forming an egg nest (Crisp & Carling, 1989; Deverall et al., 1993) having a typical dune-like shape (Figure 1). These dune-like features are commonly referred to as redd. To construct a redd the female excavates a hole, where she lays her eggs, by redirecting the surface flow with her tail (Burner, 1951; Chapman, 1988; Groot & Margolis, 1991). These egg pockets can range from 15 to 50 cm in depth, depending on fish size, species, and hydromorphological conditions (DeVries, 1997). After the eggs are fertilized by a salmon male, female salmons cover them (forming the hump, Figure 1) with the sediment moved by digging a new hole (forming the pit, Figure 1). This spawning activity results in a characteristic redd shape of a pit followed by a hump, called the tailspill (Figure 1) (Bjornn & Reiser, 1991), which has a higher permeability than the undisturbed sediments due to the winnowing away of fine grains and loosening of the sediment matrix (Coble, 1961; Merz et al., 2004; Tappel & Bjornn, 1983; Zimmermann & Lapointe, 2005a). The redd shape can be described by an amplitude, A, equal to the difference in elevation between the bottom of the pit and the top of the tailspill, i.e., crest, and its length, L, equal to the distance between the beginning of the pit and the end of the tailspill (Figure 1) (Crisp & Carling, 1989; DeVries, 1997) and their ratio $A_R=A/L$, which quantifies the aspect ratio. The higher hydraulic conductivity, K_D, of the redd sediment compared to that of surrounding undisturbed streambed material, K_{UD}, is beneficial to the

embryos because this increases the advection of oxygen-rich surface water to the egg pocket (Chapman, 1988; Zimmermann & Lapointe, 2005a) (Figure 1).

Salmonids may repeat their spawning activities several times resulting in more than one egg pocket in a single redd. In other cases, several spawners may use the same area to form superimposed redds (Hendry et al., 2004). Thus redd size may vary not only due to flow velocity and depth, excavating fish size, and sediment size (DeVries, 1997; Riebe et al., 2014), but also due to multiple spawning activities in the same location. This results in a potentially wide range of redd sizes from small redds of a few centimeters in amplitude and nearly 1 m long (e.g., sockeye salmon (*Oncorhynchus nerka*) (Hassan et al., 2015)) to large redds of decimeter amplitude and multiple meters in length (e.g., Chinook salmon (*Oncorhynchus tshawytscha*) (Bjornn & Reiser, 1991; DeVries, 1997, 2012; Evenson, 2001; Tonina & Buffington, 2009d)). This size range may cause different hydrodynamic properties of the redd because of different A_R values (Buxton, Buffington, Yager, et al., 2015), and different amplitudes protruding into the freestream flow.
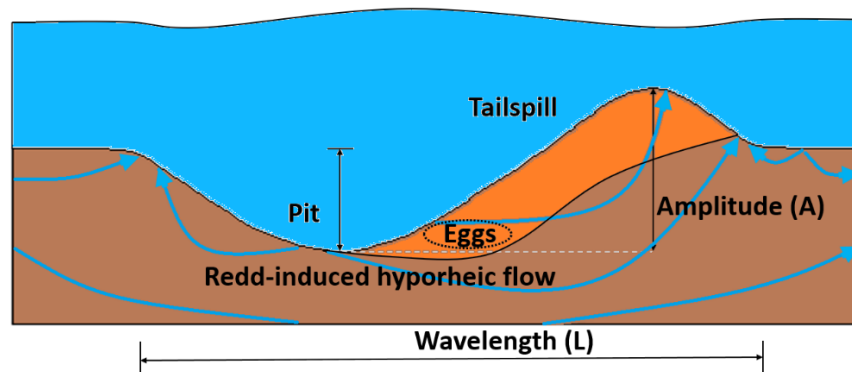
Figure 1: Sketch of a longitudinal profile of a redd along the plane intersecting the center of the redd with expected hyporheic flow lines (modified from Tonina and Buffington (Tonina & Buffington, 2009d)). The orange color indicates streambed material disturbed during spawning activity with higher hydraulic conductivity (K_D) than the undisturbed streambed (brown) material (K_{UD}).

Soon after spawning, the female salmon dies, while her embryos develop within the gravel over several weeks (Bjornn & Reiser, 1991; Boyd et al., 2010). Their successful development depends on hydrological and chemical characteristics within the redd (Bjornn & Reiser, 1991; Martin et al., 2017), whose organic environment is supported by oxygen-rich stream waters entering, flowing through, and exiting the streambed sediment (Coble, 1961; A. C. Cooper, 1965; Stuart, 1953b). This water exchange is known as hyporheic exchange (Boano et al., 2014; Tonina & Buffington, 2009c) and stems from the interaction between the freestream flow and the redd, causing large hydraulic head gradients over the upstream side of the tailspill, where stream water is driven into the sediment towards the egg pocket (Figure 1), and low hydraulic heads near the tailspill crest, where hyporheic water upwells back into the stream flow (Cardenas et al., 2016; A. C. Cooper, 1965; Stuart, 1953a) (Figure 1). This redd-induced hyporheic exchange is shallower than and superimposed over hyporheic exchange caused by large-scale streambed topography, like a pool and riffle (Tonina & Buffington, 2009d). This exchange is assumed to be discharge-dependent (Cardenas et al., 2016), but as discharge increases, both flow velocity and depth increase, and their relative importance on redd-induced hyporheic flows are not well understood. Since the redd morphology resembles a dune, Buxton et al. (2015a), recently modeled hyporheic flow through dunes using the equation of Elliot and Brooks (A. H. Elliott, 1990; 1997b, 1997a) which was derived from Fehlman's (1985) experiments for dune-like bedforms. The Elliot and Brooks equation suggests an increase in pressure difference - and thus hyporheic exchange - with an increase in velocity but a decrease with increasing water depth. Both pressure and velocity increase with an increasing discharge, but their relative increase depends on riverine morphology. Furthermore, Fehlman's (1985) experiments had two

similar dune sizes and very narrow ranges of flow velocities and depths. In contrast, besides having broad size ranges and aspect ratios, redd locations may experience shallow (a few centimeters) and deep (several meters) mean flow depths with slow (a few centimeters per second) and fast (a few meters per second) mean flow velocities. Consequently, the hydrological and morphological conditions of salmon redds go beyond those modeled by Fehlman's (1985) experiments. Thus, the equation proposed by Elliot and Brooks (A. H. Elliott, 1990; 1997a) may not be appropriate in predicting hyporheic exchange within redds under flow scenarios different from the shallow and slow freestream velocities used in the experiments.

This is an important limitation in predicting the impact of regulated flows (reservoir management or water extraction) on embryo survival because of their dependence on downwelling velocities (Coble, 1961; Martin et al., 2020). Many salmonid species may spawn in river reaches downstream of reservoirs or diversion dams, whose operations control stream discharge (Geist & Dauble, 1998; Yates et al., 2008). However, information on the impact of such management on the role of discharge on redd-induced hyporheic exchange is limited.

We aim to address this knowledge gap and study the impact of redd size and surface hydraulics on hyporheic flows within redds and the near-bed pressure gradient over redds. Previous works are limited to low discharges (< 0.5 m^3/s) with shallow depths (< 0.5 m) and slow velocities (< 0.5 m/s) for redd shape topography (Cardenas et al., 2016; Tonina & Buffington, 2009d) and velocities less than 0.8 m/s and depth less than 0.5 m for dune-like features (A. H. Elliott & Brooks, 1997b; Fehlman, 1985). This previous evidence suggests that downwelling fluxes should increase with surface velocity, and potentially decrease with

depth when velocity is kept constant, such that they should increase with discharge because the pressure difference between upstream and downstream the redd should increase. The inverse relationship with depth and direct relationship with velocity suggests that the Froude number should be a key index to characterize this process. Redd aspect ratio has been mostly overlooked, but it should also play an important role because redd length and amplitude affect the redd-induced pressure drop, such that the pressure drop should increase with A_R. Based on these observations, we hypothesize that downwelling fluxes increase with stream discharge and redd aspect ratio, and they can be predicted from a set of dimensionless numbers, including the freestream flow Reynolds and Froude numbers, the redd aspect ratio, and the redd relative submergence. Tonina and Buffington (Tonina & Buffington, 2009d) studied the effect of redd hydraulic conductivity on hyporheic exchange and showed that redd permeability has a key role in hyporheic fluxes. However, they did not show whether only the redd hydraulic conductivity is sufficient to explain the downwelling velocity when accounting for categorical heterogeneity between the redd and the surrounding undisturbed sediment. Thus, we investigate the effect of heterogeneous (dual) hydraulic conductivities between disturbed (within the redd) and undisturbed (surrounding streambed) sediments on hyporheic fluxes. We address our goal by simulating surface and subsurface flows with two-dimensional numerical hydraulic models linked through the near-bed pressure distribution quantified with a two-phase (air-water) surface water computational fluid dynamics model. We applied the modeling approach to five redd sizes which span the observed range in the field (from ~1 to ~4 m long) (Bjornn & Reiser, 1991; Deverall et al., 1993; DeVries, 1997, 2012; Evenson, 2001; Tonina & Buffington, 2009d) with L, M, S, VS and ES identifying the large, medium, small, very small and extremely small sizes with L of 3.9, 2.8, 1.82, 1 and

0.914 m and A_R of 0.77, 0.139, 0.265, 0.139 and 0.15, respectively. The imposed stream discharges span from shallow (0.1 m) and slow (0.15 m/s) to deep (8 m) and fast (3.3 m/s) waters. The paired depth-velocity values were selected from those observed near redd locations along the Sacramento River (California, USA) downstream of the Shasta dam. Results support our hypothesis of downwelling fluxes increasing with discharge or redd aspect ratio due to an increase in the near-bed head gradient over the redd.

1.2 Methods

We used a two-dimensional (2D) computational fluid dynamics (CFD) model (ANSYS®) to simulate surface (Reynolds averaged Navier Stokes equation, RANS) and groundwater (Darcian flow) hydraulics numerically. The two domains were simulated separately and linked via the near-bed pressure distribution (Janssen et al., 2012) induced by 2D simplified salmon redds (Cardenas et al., 2016), whose dimensions span those found in the literature. The surface model was validated by comparing CFD results with laboratory measurements of near-bed pressures from Fehlman (1985) as done by others (Cardenas & Wilson, 2007; Reeder et al., 2018; Trauth et al., 2013) and by data from experiments in our salmon redd physical model constructed with tetrafluoroethylene hexafluoropropylene vinylidene fluoride (THV), produced by 3M, grains in the laboratory. The results from the surface and subsurface models were interpreted with a set of dimensional numbers to generalize the results for the pressure drop around the redd and the interstitial downwelling fluxes through the redd (Monofy & Boano, 2021).

1.2.1   Surface flow hydraulics

Open channel flow surface hydraulics were modeled by solving the RANS equations with a

κ-ε realizable turbulence closure scheme incorporated within the finite volume ANSYS

software program. This turbulence closure was chosen because of its higher performance

over other schemes in terms of predicting flows with strong streamlines curvature, flow

separations, and with complex secondary flow features (*ANSYS Fluent Theory Guide*, 2019).

Surface water elevation of open channel flows with the fixed lid approach (Janssen et al.,

2012), which prescribes the water surface elevation with an impermeable, slip, and no-shear

wall condition, may not properly capture the spatial gradients that are present in open

channel flows (Meselhe & Odgaard, 1998; Monsalve & Yager, 2017). As a result, we treated

the system as a two-phase (air and water) problem and tracked the water surface elevation at

the air-water interface using the volume of fluid (VOF) approach (Hirt & Nichols, 1981). The

water surface profile was extracted at locations where the volume fraction is 0.5, with values

of 1 or 0 representing only water or air, respectively. We used a long flow domain with two

fixed-lid sections upstream and downstream of a 45 m long two-phase domain to train and

develop the flow (Figure 2a). We ran all simulations for at least two flow cycles throughout

the full domain to ensure that the flows were in equilibrium with the boundary conditions.

The water-sediment interface was specified as a smooth, no-slip impermeable boundary,

which is a typical condition for this problem (Cardenas & Wilson, 2007c; Chen et al., 2015),

because momentum and mass exchanges with porous sediment are small and have negligible

influence on surface hydraulics (Janssen et al., 2012). Grain roughness may impact local

exchange but at the redd-scale, which is important for the incubating eggs as they are several

median grain diameters below the surface, we assumed that the redd-shape induces the

exchange reaching the eggs. This is the case for dune-like bedform with a roughness size of 2 mm (Janssen et al., 2012). Water boundaries were defined as velocity inlet and velocity outlet conditions for the upstream and downstream locations, respectively, whereas air boundaries were specified as pressure outlets. The entire domain was sloped to resemble a streambed gravity flow (A. H. Elliott & Brooks, 1997b; Fehlman, 1985) with slope values ranging from 0.1 to 0.001% and estimated from Manning's *n* uniform flow equation using the known local velocity and flow depth. There are approximately two million quadrilateral cells with a mean cell size of about 2.4 cm in the horizontal direction. We employed a highly refined 1.5 mm cell size in the vertical direction at the air-water interface to accurately track water surface elevation and a very small vertical cell size of about 0.1 mm near the bottom boundary (Figure 2b). We ran mesh independence tests with three different mesh sizes (fine, medium, and coarse) by reducing the mesh dimensions by 30%, and compared their predicted pressure distributions, which resulted in a change of total head drop through the redd of less than 3% from the fine to coarse mesh. Therefore, all simulations were conducted with the medium mesh to save computational costs.
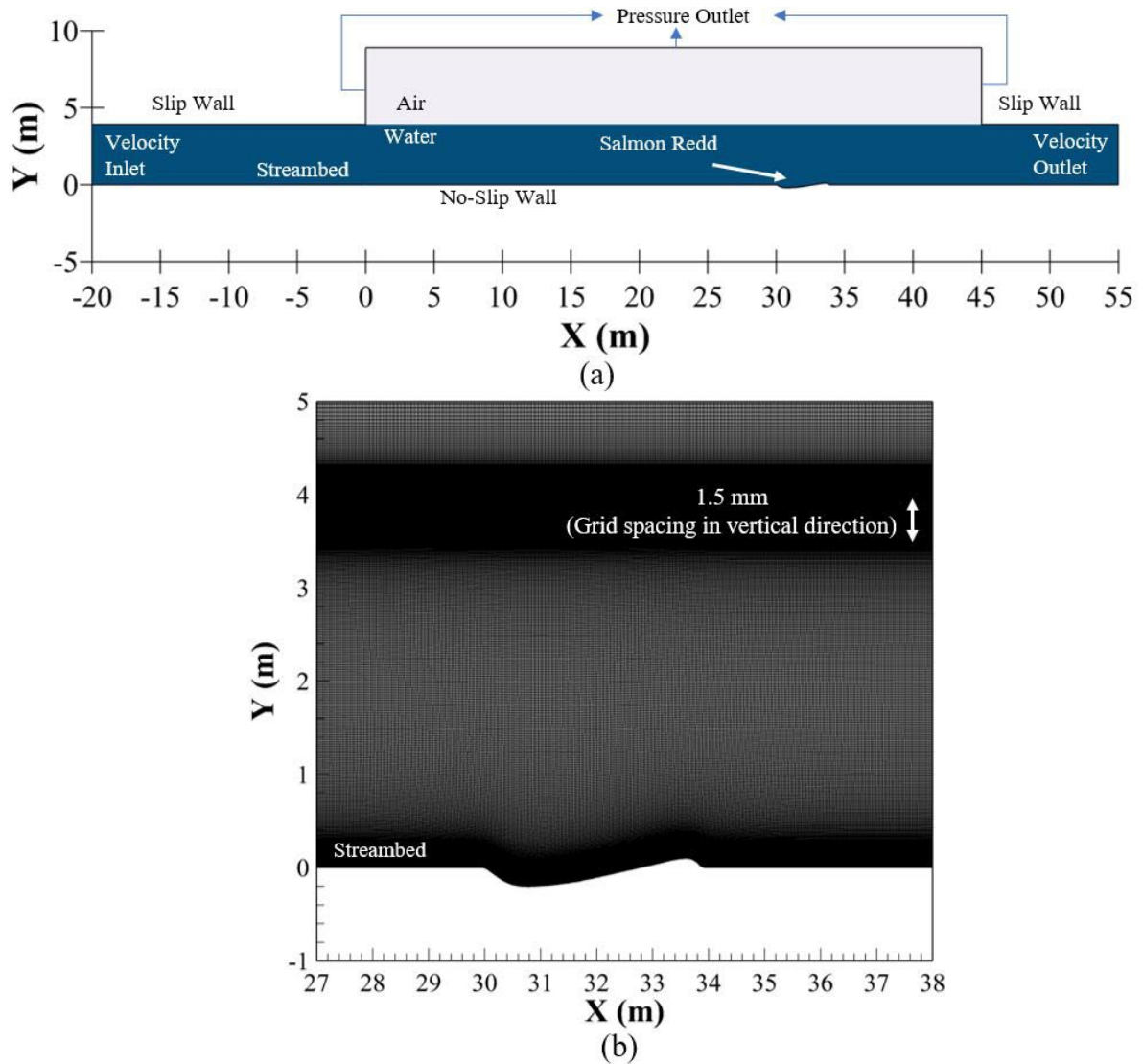
Figure 2*:* Simulation domain design: (a) surface flow domain with air colored in grey and water colored in blue along with the boundary conditions, and (b) Zoomed-in section near the redd showing the mesh. Flow is from left to right.

1.2.2   Groundwater flow hydraulics

A steady-state Darcian groundwater flow was solved to predict the redd-induced interstitial

flows (Cardenas et al., 2016; Tonina & Buffington, 2009d) in ANSYS. The water-sediment

interface was defined as a pressure inlet boundary condition with the specified pressure

distribution predicted from the CFD surface model. A periodic boundary condition, which

simulates an infinite periodic domain, was applied at the upstream and downstream locations of the subsurface domain boundaries with an ambient groundwater flow of about 0.001 mm/s, which mimics a large-scale longitudinal groundwater flow caused by a valley slope. The bottom boundary was treated as a no-slip impermeable wall positioned five meters below the flat water-sediment interface to not affect the redd-induced hyporheic flow. The average grid cell size was 2.4 cm horizontally and 1.5 cm vertically, resulting in approximately one million quadrilateral cells. The permeability, k, was set to be homogenous and isotropic, with a value of $5.1 \cdot 10^{-11}$ m^2, equivalent to a hydraulic conductivity of $K = 0.0005$ m/s. This value is within the range found in literature, with values ranging from $K = 0.00009$ to 0.0021 m/s (Geist, 2005a; Hanrahan et al., 2005; Malcolm et al., 2004) and even higher in restored systems 0.011 m/s (Harrison et al., 2019). The value of K does not impact the hyporheic morphology in the homogenous case but impacts the magnitude of fluxes and residence time. Thus, for a homogenous case the downwelling flux could be scaled by the redd hydraulic conductivity whereas, in the case of dual heterogeneity (disturbed and undisturbed sediment), the ratio between them could be added as an additional scaling parameter. We test whether this effect is important with the categorical heterogeneous case.

Due to the winnowing of fine material and loosening of the sediment matrix during the redd construction, newly formed redds have a higher hydraulic conductivity, K_D (disturbed sediment), than that of the undisturbed streambed material, K_{UD} (undisturbed sediment). These two different hydraulic conductivities form a categorical heterogeneous system, which may result in a higher mean downwelling flow than the homogenous case. To investigate this possibility, we studied a case of categorical heterogeneity for run 14, M (Table 4), a medium redd with a surface flow depth of 3.92 m and velocity of 1.49 m/s. The hydraulic

conductivity within the redd was increased by half an order of magnitude ($K_D = 5 \cdot K_{UD}$) and one full order of magnitude ($K_D = 10 \cdot K_{UD}$) as documented in the literature (Zimmermann & Lapointe, 2005a) from that of the surrounding undisturbed sediment ($K_{UD} = K = 0.0005$ m/s) (Figure 1). Because hyporheic flow is chiefly a near-surface process, we hypothesized that the hydraulic conductivity of the redd would dominate the redd-induced hyporheic flows and thus the effect of categorical heterogeneity between the disturbed and undisturbed sediment would be negligible, causing the system to be treated as homogenous with the hydraulic conductivity of the redd as the reference property. This heterogeneity is different from the internal heterogeneity caused by the redd internal architecture which may form zones of progressive lower hydraulic conductivity from the egg pocket to the redd surface (Chapman, 1988), potentially forming a gradient in the hydraulic conductivity within the redd.

1.3 CFD simulations verification and validation

We validated the CFD modeling by comparing flow hydraulics predicted by the model with those measured in the flume experiments with dune bedforms conducted by Fehlman (1985) as well as those of a redd bedform conducted by us in this study. We also quantified uncertainty due to measurement errors and validated the mesh and time-step used in the simulations.

1.3.1   *Fehlman's (1985) flume experiments*

We used Fehlman's (1985) data set which contains pressure distributions over dunes to test the performance of the CFD modeling in predicting surface hydraulics and thus near-surface pressure distribution, because dunes have similar geometry to redds. Although redds has

some differences from dunes, (1) they have a pit, (2) typically are present as single features whereas dunes are present as a series, and (3) they are formed during spawning activity and not formed by alluvial processes. However, they share an overall similar shape with a potential flow and pressure reversals downstream the crest. Although the experiments of Fehlman (1985) were for impermeable dunes whereas redds are permeable structures, the mass exchange through the redd is still small compared to the surface discharge. To address these limitations of Fehlman's (1985) experiments, we also tested the model with a real permeable redd (see section 3.2). From Fehlman's experiment, we selected two cases that have the same average flow depth of 0.22 m but two distinct average flow velocities of 0.29 m/s and 0.44 m/s (Fehlman, 1985). We simulated the entire flume experiment as an open channel flow and extracted the pressure and water surface profiles at the 8th (center) dune, out of 15 consecutive dunes as done experimentally by Fehlman (1985). Simulation performance was quantified with Nash-Sutcliffe coefficients (NSC) whose values indicate the quality of the model performance: very good (NSC > 0.75), good (0.65 < NSC ≤ 0.75), satisfactory (0.5 < NSC ≤ 0.65), and unsatisfactory (NSC ≤ 0.5) (Moriasi et al., 2007). The accuracy of the comparison by visual inspection between predicted and measured pressure distributions (Figure 3a) is comparable to that reported in the literature (Broecker et al., 2018; Cardenas & Wilson, 2007a; Reeder et al., 2018). The NSC of 0.7 and 0.6 for flows with velocities of 0.29 m/s and 0.44 m/s respectively also support the visual inspection. Unlike previous studies, we also modeled the respective water surface elevations to those reported by Fehlman (1985) with NSC values of 0.8 and 0.7 (Figure 3b). The root-mean-square error and standard deviation obtained for pressure distribution were found to be 10.37 Pa and 9.797 Pa for a flow velocity of 0.29 m/s, and 28.58 Pa and 25.8 Pa for a flow velocity of 0.44

m/s. The corresponding values for the water surface were 0.001 m and 0.0005 m for a flow velocity of 0.29 m/s and 0.002 m and 0.0017 m for a flow velocity of 0.44 m/s.

It is important to note that Fehlman's (1985) experiment does not capture the pressure dip at the crest due to the absence of pressure taps (Figure 3a near position 0.68 m). The adverse pressure gradient formed downstream of the crest affects both the water surface and pressure downstream of the crest and the simulations overestimate them. Conversely, simulations underestimate the water surface elevation and pressure upstream of the crest. These results are consistent with observations from other flume experiments (Huettel & Gust, 1992), which have reported an adverse pressure gradient near the pressure dip caused by eddy detachment. Cardenas and Wilson (2007a) have also used Fehlman's experiments for validation and have recognized the difficulty in capturing the crest as a singularity with an adverse pressure gradient both numerically and experimentally (Broecker et al., 2018; Cardenas & Wilson, 2007a; Reeder et al., 2018). The overall performance of our simulation is comparable to the published works.
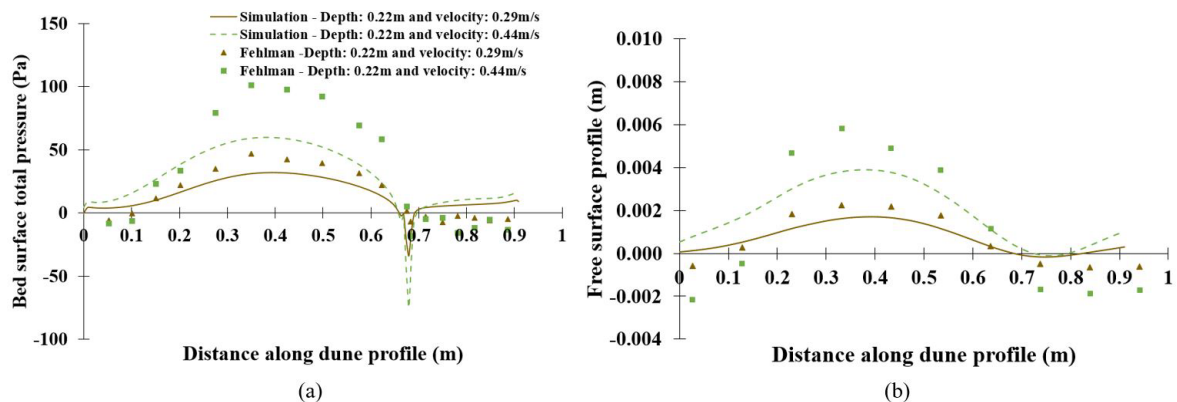
Figure 3: Comparison between simulations (lines) and Fehlman's experiments (symbols) for (a) total pressure and (b) free surface profiles at the 8th dune. Flow is from left to right.

1.3.2 Redd experiments

These experiments were designed to test the performance of the CFD modeling with a range

of flows and redd sizes realistic but not exactly matching a real case. We conducted four

experimental runs with four combinations of upstream flows: two depths of shallow (0.1 m)

and deep (0.2 m) waters and two velocities of slow (0.1 m/s) and fast (0.2 m/s) flow in a 7 m

long, 0.5 m wide, and 0.7 m deep recirculating flume (Table 1) at the Center for

Ecohydraulics Research (Bhattarai et al., 2022; Moreto et al., 2022). The flow conditions

were chosen to simulate a shallow flow whose water surface warps over the redd due to flow-

redd interaction and a deep flow with negligible impact on water surface elevation over the

redd. The velocities were limited by the capacity of the pump but were still near those

observed at redd locations (Deverall et al., 1993). The redd size was a 1/3-scaled version of

an average redd and was made with THV grains with uniform shape and size of 3 mm

diameter. THV has a specific gravity of about 2 and its refractive index, RI, is about 1.365.

The grains were stable after some transport, so the redd topography was established in the

flume with the flow regime after a small adjustment near the crest of the constructed redd.

We matched the RI by adding 14% by-weight of Epsom salt to fresh water. This resulted in

transparent grains once saturated with the fluid, allowing us to map the flow velocity near the

streambed with the non-intrusive imaging technique of stereo particles image velocimetry,

SPIV.

The rest of the sediment was made with a crushed glass of about 3 mm in size. The redd was

placed in the middle section of the flume to minimize boundary effects. The water passed

through a flow straightener before entering the flume while a weir gate regulated the

downstream boundary. SPIV was used to map the flow field downstream of the redd crest

where complex hydraulics occur to validate the CFD model. We measured the flow field at upstream (X = -1.14 m) and downstream (X = 1.42 m) locations to define boundary conditions for the streamwise (V_x) and vertical (V_y) velocities (V_y was less than 2% of V_x) as well as the turbulence kinetic energy (*TKE*) profiles for the CFD models (Figure 4a). 2,000 image pairs were collected during the SPIV experiments, which ensured the ergodicity of the flow field (Moreto et al., 2022).
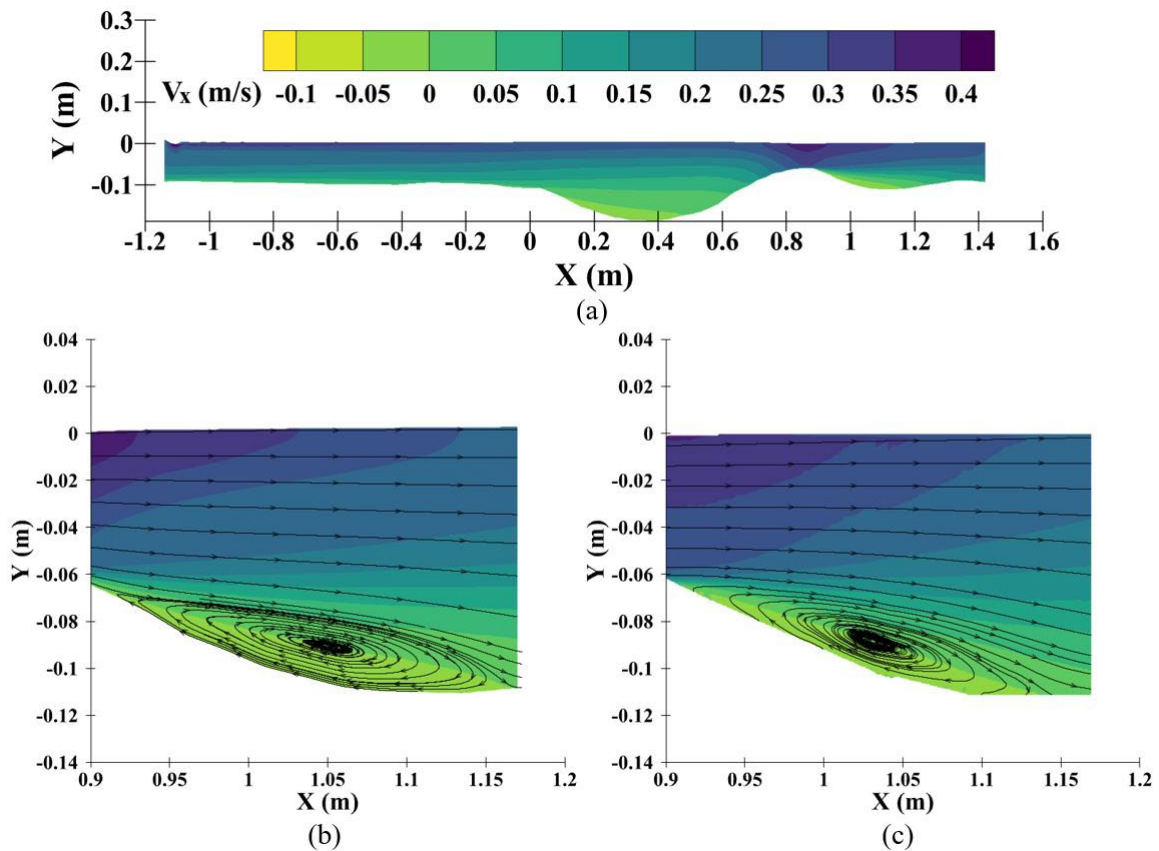
Figure 4: Velocity field for the shallow-fast case for (a) the entire simulation domain, and close-up views downstream of the redd crest simulated by (b) CFD and (c) measured with stereo particle image velocimetry. Flow is from left to right.

Table 1. Four experimental flow conditions used as CFD boundary conditions, with average depths (averaged between the upstream and downstream locations), average velocities, and average *TKE*.

Runs Description	Avg Depth (m)	Avg velocity (V_x) (m/s)		Avg TKE (m^2/s^2) $\times 10^{-4}$	
		Upstream	Downstream	Upstream	Downstream
Shallow-fast	0.105	0.191	0.209	2.13	20.4
Shallow-slow	0.098	0.103	0.109	0.638	6.18
Deep-fast	0.1974	0.175	0.169	0.933	4.77
Deep-slow	0.1972	0.085	0.081	0.194	1.26

Comparisons of the overall size of the separation vortex and reattachment locations show very good agreement between the measured and predicted flow fields downstream of the redd (Figure 4b and Figure 4c). Comparisons between streamwise velocity profiles just downstream of the crest ($X = 0.95$ m) and near the bottom of the hump ($X = 1.15$ m) for all four flow cases give very good NSC values of 0.954 and 0.969 for the shallow-fast flow, 0.824 and 0.967 for shallow-slow flow, 0.644 and 0.923 for deep-fast flow, and 0.6 and 0.845 for deep-slow flow at $X = 0.95$ m and $X = 1.15$ m, respectively (Figure 5). This confirms that our CFD model adequately predicted the flow field caused by the redd-flow interaction. The beginning of the flow separation, which leads to the formation of a separation vortex downstream, can be attributed to the slight deviation shown between the streamwise velocity profile prediction derived using the model and the experimental data at $X = 0.95$ m. Although the error is very minor, it is comparatively higher than the errors observed at other locations.
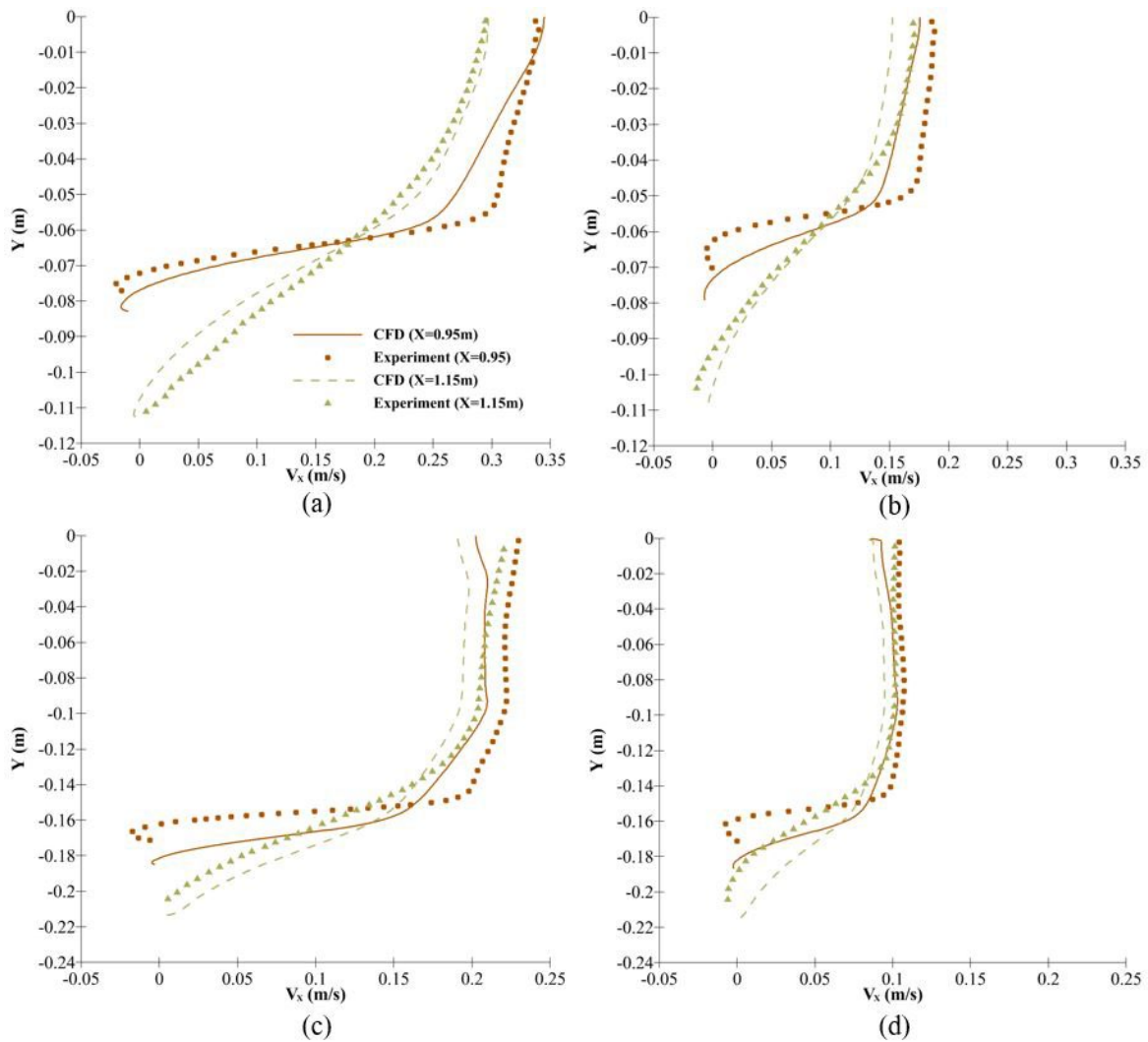
Figure 5: Comparison between the simulated (solid and dash) and experimental (symbols) streamwise velocity profiles at $X = 0.95$ m and 1.15 m for (a) shallow-fast, (b) shallow-slow, (c) deep-fast, and (d) deep-slow flows.

Matching the refractive index of the fluid and solid allowed us to test the performance of the groundwater modeling in predicting the hyporheic-flow path. We mapped the movement of two dye plumes within the redd sediment using planar laser-induced fluorescence, PLIF. For the shallow-fast flow case, we injected rhodamine B at the sediment-water interface 7 cm from the side wall of the flume (to avoid side wall effects). We mapped two hyporheic flow lines by tracking the movements of each plume front. Quantification of the local velocity was

done by dividing the dye front displacement between frames by elapsed time. This provides a Darcian-scale velocity field (i.e., velocities are averaged over several pores), which is comparable to that predicted by the numerical model. Visual inspection of the simulated and observed flow lines shows good agreement as observed by others (e.g., Janssen et al 2012), although, with some deviation likely due to local permeability heterogeneity (Figure 6).

We also compared the local Darcian velocities along the flow lines between simulation, V_s, and experiments, V_o and quantified their relative residuals, $Res_v = \frac{(Vo-Vs)}{Vo}.100$, expressed in %. We then quantified the average residual between the observed and the predicted local values along each experimental flow line. The averaged residuals were 13% and -14%, and standard deviations, 26% and 73% of the Res_v for flow lines 1 and 2 respectively. Comparison between travel times along modeled and observed flow lines also show very good match (Figure 6b) with errors of 1% (experiment, 35.5 s, and predicted, 35.13 s), and -1.4% (experiment, 97.5 s, and predicted, 98.88 s), for flow lines 1 and 2 respectively (Reeder et al., 2018). Given the uncertainty in local hydraulic conductivity, these comparisons suggest a good performance of the groundwater modeling.
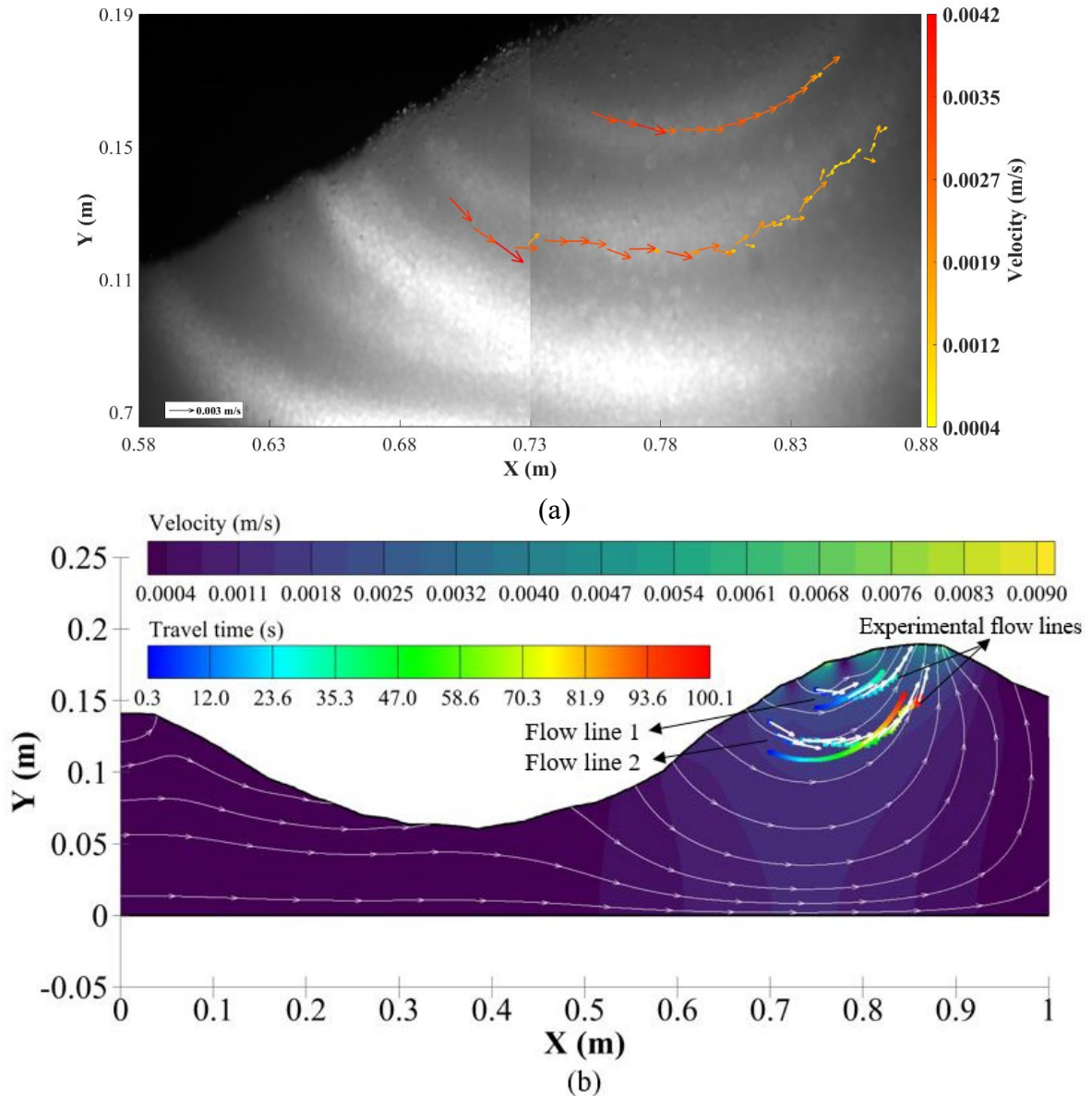
Figure 6: Subsurface flow visualization for the shallow-fast flow case representing (a) experimental flow lines with velocity magnitude-colored vectors and (b) simulated and experimental flow lines color-coded with travel times over contours of simulated velocity magnitude and streamlines. Vectors over the experiment flow lines represent the simulated local flow direction. Flow is from left to right.

1.3.3   Solution verification and validation

To ensure that the results are independent of mesh and time-step resolutions, we performed a solution verification for Vx on three systematically refined meshes (fine, medium, and

coarse) for the shallow-fast surface flow case, which is the most critical one. The overall grid size, the total number of grid points, and time step size used are given in Table 2. We used a grid refinement ratio, $r_G = \Delta x_2 / \Delta x_1 = \Delta x_3 / \Delta x_2 = 1.414$, where Δx is the grid distance between two elements and the subscripts 1, 2, and 3 represent the fine, medium, and coarse meshes, respectively. The overall procedure is as described in (Xing et al., 2008; Xing & Stern, 2010, 2011). The convergence ratio, denoted by R_G, is the ratio of solution differences for medium-fine and coarse-medium solution pairs. L2 norms (square root of the sum of the squares of the differences between the coordinates of the two points) of streamwise velocity profiles are used to calculate $\varepsilon_{G_{21}}$ and $\varepsilon_{G_{32}}$ to define the ratios for R_G and P_G (observed order of accuracy), i.e.,

$$\langle R_G \rangle = \left\| \varepsilon_{G_{21}} \right\|_2 / \left\| \varepsilon_{G_{32}} \right\|_2 \tag{1}$$

$$\text{where } \left\| \varepsilon_{G_{21}} \right\|_2 = \sqrt{\sum_{k=1}^{N}(P_1 - P_2)^2} \tag{2}$$

$$\langle P_G \rangle = \frac{ln(\left\| \varepsilon_{G_{32}} \right\|_2 / \left\| \varepsilon_{G_{21}} \right\|_2)}{\ln(r_G)} \tag{3}$$

where $\langle \rangle$ & and $\| \|_2$ denotes a profile-averaged quantity (solution change ratio based on L2 norms) and L2 norm, respectively (Wilson et al., 2001). N is the number of points along a single velocity profile and P_1 and P_2 are the point solutions (V_x) for meshes 1 and 2, respectively. U_G is the numerical uncertainty estimate and $|E|$ is the absolute relative error between the fine mesh and the experimental data, representing a measure of bias error between the numerical and experimental results ($|E| = |S - D|$), where S is the fine mesh streamwise average velocity, and D is the experimental streamwise average velocity. U_V is

the validation uncertainty ($U_V = \sqrt{U_G^2 + U_D^2}$), where U_D is the experimental uncertainty,

representing an average uncertainty of the numerical and experimental results. Validation is

achieved when $|E| < U_V$.

Table 2. Solution verification.

Grids	Grid Dimensions	Total Number of Points	Time step size (s)
1	869 × 220	191,180	0.002
2	615 × 155	95,325	0.002828
3	430 × 108	46,440	0.004

For the solution verification and validation study, we used four locations (X = 1 m, 1.05 m,

1.1 m, and 1.15 m). The grid triplet showed monotonic convergence ($0 < R_G < 1$) at all

horizontal locations with small grid uncertainty values ranging from 31.7 %D to 62.5 %D.

All four locations showed that the model was validated ($|E| < U_V$) (Table 3).

Table 3. Verification & Validation study for the longitudinal component of the velocity. Percentages
are calculated using experimental data (%D).

X-location (m)	R_G	P_G	U_G	U_G(%D)	U_D(%D)	$|E|$(%D)	U_V(%D)
1.0	0.23	4.14	0.0695	31.69	0.33	1.36	31.7
1.05	0.24	4.1	0.0638	32.68	0.41	2.56	32.68
1.1	0.27	3.74	0.066	36.17	0.5	3.57	36.17
1.15	0.39	2.72	0.11	62.53	0.55	2.70	62.53

1.4 Flow scenarios

We developed a set of 32 flow simulations using paired mean flow depth and velocity values

obtained at redd locations along the Sacramento River for Chinook salmon (*Oncorhynchus*

tshawytscha) (Table 4) (Data from NOAA, Andrew Pike, Winter-run Chinook salmon

Lifecycle model project, see data repository). The Sacramento River data (19 velocity-depth

sets) were augmented with one set of surface water information from the Columbia River

(Mueller, 2005), six sets of Fehlman's (1985) flume experimental runs, two sets from

Deverall's (Deverall et al., 1993) field data, and four additional depth-velocity sets to

increase the range to shallower flow conditions than those observed in the Sacramento River

data. These paired velocity-depth flows are mean reach scale values, of depth and flow and

not over the redd. Thus, they provide information on the surface flow hydraulics which can

be used as boundary conditions for numerical modeling. We used three redd sizes to account

for their natural variation: large, medium, and small, with lengths of 3.9, 2.8, and 1.82 m and

aspect ratios of 0.077, 0.139, and 0.265, respectively (Deverall et al., 1993; Evenson, 2001;

Tonina & Buffington, 2009d). These three sizes were augmented with two additional smaller

redd sizes for shallow water conditions to mimic egg nests built by salmonids, such as

sockeye salmon (*Oncorhynchus nerka*) which are smaller than Chinook salmon. The smaller

redds had wavelengths of 1.0 m and 0.914 m, with aspect ratios of 0.139 and 0.15,

respectively.

1.5 Data analysis

We expressed pressure (P) as a pressure head with a unit of meters of water, i.e., P/γ, where γ

is the specific weight of water. To compare the distributions among all scenarios, we

removed the effect of the hydrostatic pressure over the undisturbed inclined bed and the local

slope by defining the relative total head, $H_R = H-(Y_0+z)$, where H is the total head, Y_0 is the

undisturbed hydraulic depth away from the redd based on the inlet water depth and z is the

difference between the local streambed and the datum that are sloped at the same angle

(Figure 7). This is similar to Fehlman's (1985) approach, but while he referenced the

pressure to the depth at the dune crest, we used Y_0 and mean flow velocity, v, upstream

enough from the redd as a reference value. These values would be similar to those quantified

at the reach scale which would be available through one-dimensional hydraulic modeling or

discharge field surveys. The use of H_R eliminates the influence of the large static pressure

(Y_0) running over small near-bed pressure variations and mean streambed slope for all

simulations, allowing visualization of the pressure difference from its mean value. This

pressure gradient induces the hyporheic exchange (A. H. Elliott & Brooks, 1997b) (Figure 1).

The relative water surface elevation (WSE_R) is defined as the difference between the local

free surface elevation and the undisturbed free surface elevation based on water depth at the

inlet (Figure 7).
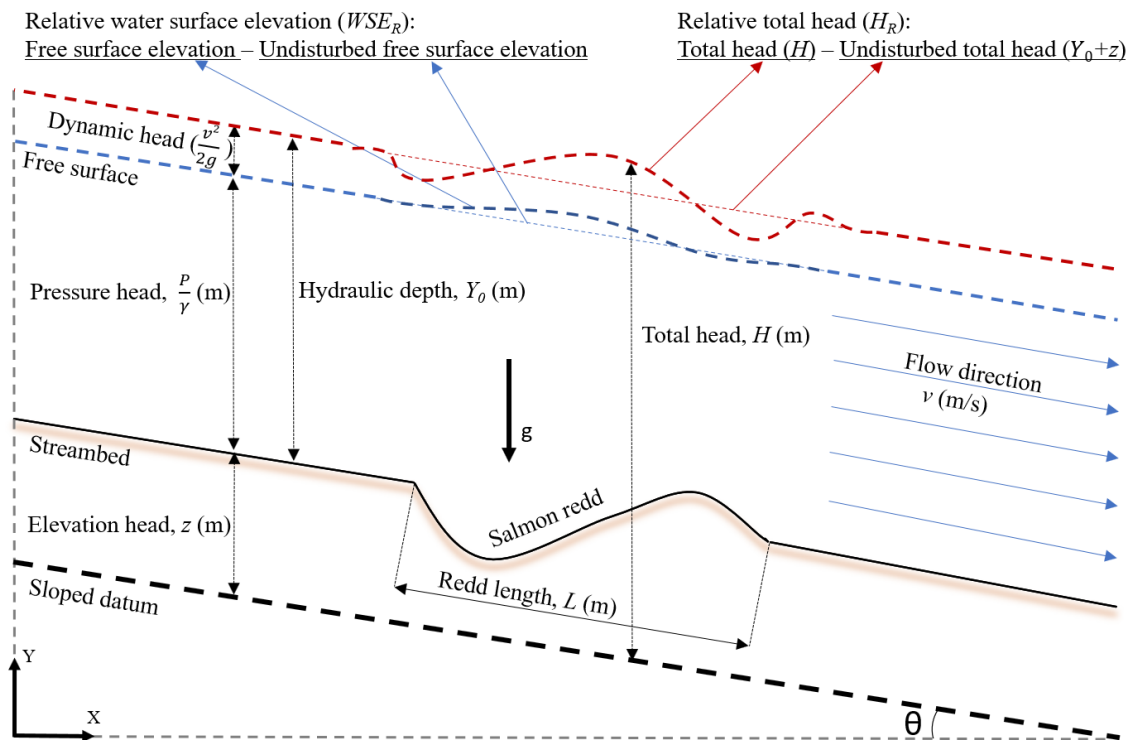
Figure 7: An illustration of all heads flowing across the redd in an open channel flow (the slope angle is so small such that the water depths in the vertical direction Y and normal direction of the slope are functionally identical). Flow is from left to right.

1.6 Dimensional Analysis

We used dimensional analysis to derive the functional relationship among our dependent

variables, hyporheic downwelling flux, and pressure gradient over the redd, and other

hydraulic variables. From a dimensional analysis of the problem, we found that the redd-

induced total head drop, $\Delta H_R = H_{R,\,H} - H_{R,\,L}$, with $H_{R,\,H}$, and $H_{R,\,L}$ being the maximum and

minimum relative total heads over the redd, respectively, depends on seven quantities: mean

cross-sectional velocity, v, undisturbed hydraulic depth, Y_0, gravity, g, dynamic viscosity, μ,

the density of water, ρ, redd amplitude, A, and redd length, L. The application of the

Buckingham theorem reduces them to a set of five dimensionless groups, which are the

pressure gradient, $H^* = \frac{\Delta H_R}{L}$, the redd aspect ratio, A_R, the redd relative submergence, A/Y_0,

freestream Reynolds number, $Re = \frac{v \cdot Y_0}{v}$ and the freestream Froude number, $Fr = \frac{v}{\sqrt{g \cdot Y_0}}$. A

similar analysis to predict the spatially averaged hyporheic downwelling fluxes over the

entire redd, $\bar{q}_d$, and over the portion that delivers oxygen-rich surface water to the egg

pocket, $\bar{q}_{d,ep}$, (both normalized by the redd hydraulic conductivity (K) of the streambed

sediment, $\bar{q}_d^* = \bar{q}_d/K$ and $\bar{q}_{d,ep}^* = \bar{q}_{d,ep}/K$) yields the same set of dimensionless independent

variables. The dimensionless downwelling velocity, q_d^*, also allows comparison between the

homogenous and categorical heterogeneous hydraulic conductivity cases. When

homogeneous q_d^* are plotted against those of the heterogeneous cases and fall on a 1:1 line,

the system does not depend on the effect of the categorical heterogeneity, but it is chiefly

governed by the redd hydraulic conductivity. In our analysis, we did not consider the

alluvium depth a hindrance and thus we neglected it. We performed regression analysis to

characterize the functional relationship between the dependent dimensionless variables and

the set of independent dimensionless variables, e.g., $H^* = f(Re, Fr, A_R, A/Y_0)$. The

simulations were split into two groups, one with 21 simulations to develop regression curves

and the other with 27 simulations to validate the curves.

Table 4. Summary of surface flow characteristics and redd sizes with L, M, S, VS, and ES identifying the large, medium, small, very small, and extremely small sizes. The 21 simulations utilized for validation from the independent set of calibration are marked with an asterisk (*) on the redd size. The data source for velocity-depth paired values are (Fehlman, 1985), (Deverall et al., 1993), Columbia River (Mueller, 2005), and Sacramento River (Data from NOAA, Andrew Pike, Winter-run Chinook salmon Lifecycle model project).

Run Number	Flow Depth (m)	Velocity (m/s)	Froude Number (Fr)	Reynolds Number (Re)	Redd Size	Source
1	0.25	0.15	0.10	37158	L*	Fehlman
2	0.25	0.29	0.19	72829	L*	Fehlman
3	0.38	0.58	0.30	218913	L, M*, S	Deverall
4	0.75	0.35	0.13	260729	L	Deverall
5	1.14	0.68	0.20	764308	L	Sacramento River
6	1.67	0.91	0.23	1514422	L	Sacramento River
7	1.94	0.40	0.09	761129	L*, M, S*	Sacramento River
8	2.06	1.12	0.25	2291632	L	Sacramento River
9	2.31	0.59	0.12	1351410	L, M*, S	Sacramento River
10	2.47	1.28	0.26	3140267	L	Sacramento River
11	2.88	0.91	0.17	2597395	L*, M, S*	Sacramento River
12	3.30	1.69	0.30	5539369	L	Sacramento River
13	3.47	1.27	0.22	4377164	L*	Sacramento River
14	3.92	1.49	0.24	5801389	L, M*, S	Sacramento River
15	4.04	1.90	0.30	7624205	L	Sacramento River
16	4.39	1.68	0.26	7325435	L	Sacramento River
17	4.73	2.03	0.30	9537110	L	Sacramento River
18	4.84	1.85	0.27	8893582	L	Sacramento River
19	5.22	2.00	0.28	10369555	L*, M, S*	Sacramento River
20	5.69	2.21	0.30	12490049	L	Sacramento River
21	6.51	2.60	0.33	16811790	L, M*, S	Sacramento River
22	7.03	2.87	0.35	20039960	L	Sacramento River
23	7.30	0.60	0.07	4350445	L	Columbia River
24	7.95	3.26	0.37	25742122	L*, M*, S	Sacramento River
25	0.1	0.15	0.15	14899	VS*	This study
26	0.1	0.3	0.3	29798	VS	This study
27	0.2	0.15	0.11	29798	VS*	This study
28	0.2	0.3	0.21	59595	VS	This study
29	0.27	0.16	0.10	44118	ES*	Fehlman
30	0.22	0.29	0.2	64715	ES*	Fehlman
31	0.32	0.36	0.2	114040	ES*	Fehlman
32	0.27	0.49	0.3	132272	ES*	Fehlman

1.7 Results

1.7.1   Modeled surface flow

Both relative water surface elevation, WSE_R, (Figure 8a), and relative total head, H_R, (Figure 8b) over the redd depend on flow depth and velocity. For the same water depth, both WSE_R and H_R amplitudes increase with stream velocity (Figure 8, compare runs 1 and 2). However, when keeping the same velocity, the H_R amplitude tends to remain constant with increasing depth, whereas WSE_R amplitude decreases with increasing depth (circle and downward triangle, runs 6 and 11). The deepest and fastest flow (diamond, run 24) causes the largest H_R amplitude over the redd (Figure 8b). As observed for dune-like bedforms, discharge regulates the magnitude of the pressure amplitude, which increases with discharge, but the shape of the pressure distribution remains the same regardless of discharge. Unlike dunes, which have only one minimum and one maximum pressure, redds have two minima, one at the head of the pit and one at the crest, and two maxima, one near the middle of the tailspill, and the other downstream of the crest, where the redd ends at the undisturbed bed (Figure 8b). The lowest minimum near-bed pressure occurs at the crest of the redd, and the highest near-bed pressure occurs along the middle of the tailspill.
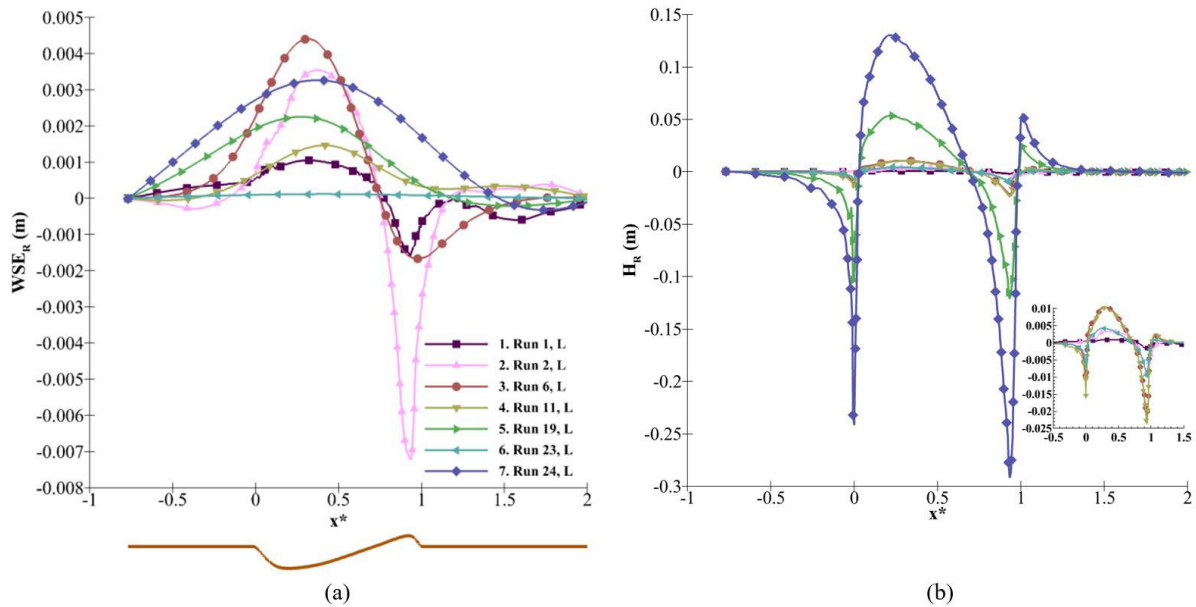
Figure 8: (a) Relative water surface elevation (WSE_R) and (b) Relative total head (H_R) as a function of dimensionless distance x^*, defined as the distance normalized by redd wavelength ($x^* = x/L$), over the large redd size (3.9 m) starting at $x^* = 0$. Flow is from left to right.

Redd aspect ratios affect the pressure drop magnitude, and large A_R values (~0.265) also have a profound impact on the shape of the pressure profile (Figure 9). The magnitude of the second maximum near-bed pressure value, which lies downstream of the crest, decreases as A_R increases until it disappears for A_R values between 0.14 and 0.26.

The interaction between surface flows and redd shapes and sizes (A_R) affects the flow velocity with stronger near-bed velocity gradients as either discharge or A_R increases (Figure 10). For each discharge and A_R, the highest velocity occurs on the crest of the redd, and the slowest velocity occurs in the pit. Another low velocity is detected just downstream of the redd's lee side. The size of the separation vortices within the pit increases as the surface flow velocity increases. The same is true with decreasing redd size, even for the same discharge. Another flow recirculation is developed just downstream of the tailspill for the smallest redd indicating that increasing discharges and A_R values result in increasing pressure amplitudes

over the redd. This process causes a systematic increase of the total head drop, H^*, with an increase in the Reynolds, Froude, and A_R numbers (Figure 11).
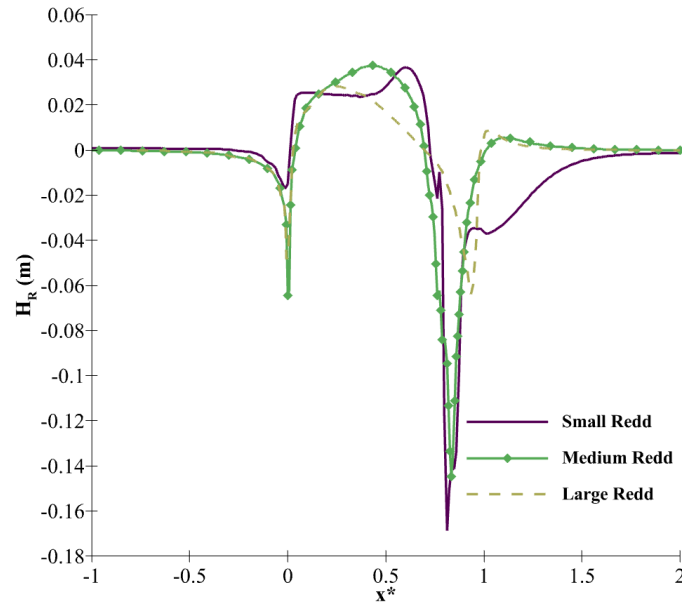
Figure 9: Relative total head (H_R) over three redd sizes (Small = 1.82 m, Medium = 2.8 m, and Large = 3.9 m) for Run 14. Aspect Ratios are A_R = 0.265, 0.139, and 0.077, respectively.
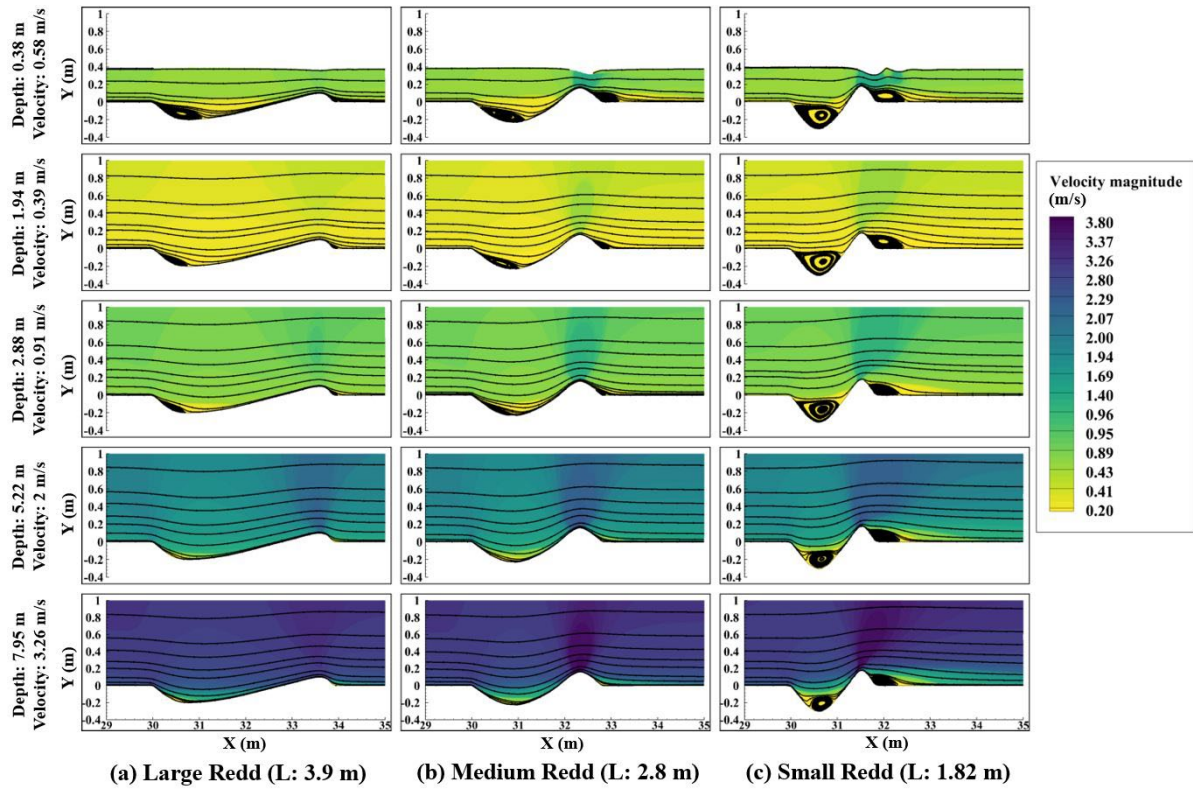
Figure 10: Surface flow characteristics for different surface hydrodynamics and different redd sizes. Flow is from left to right.
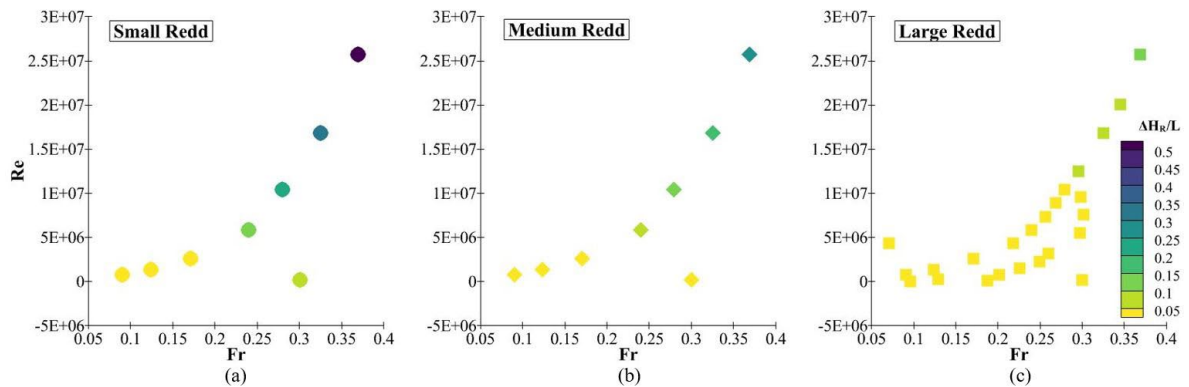
Figure 11: Dimensionless total head ($\Delta H_R/L$) as a function of Reynolds Number (Re), Froude Number (Fr), and Redd Aspect Ratio (A_R). Aspect Ratios are $A_R = 0.265$, 0.139, and 0.077 for small, medium, and large redd respectively.

1.7.2 Modeled hyporheic flow

Upwelling and downwelling fluxes, forming the hyporheic exchange, increase with discharge (Figure 12). Maximum normal velocity (q_{max}) for small, medium, and large redds

are 0.00396 m/s, 0.0009 m/s, and 0.00068 m/s, respectively. As with H_R, their magnitude

decreases as water depth and velocity decrease. The highest redd aspect ratio gives rise to the

maximum hyporheic exchange, the largest hyporheic cell size, and the highest downwelling

velocity. High upwelling (negative normal velocity) and downwelling velocities are seen in

the same locations as the high H_R values (compare Figure 8 and Figure 12). The surface

flow-redd interaction formed three to four recirculating cells: one large cell with a

downstream flow direction between the redd trough and crest, two with an upstream flow

direction (one below the pit and one at the crest), and one slightly downstream of the crest

(upstream flow direction) that did not appear for low A_R (Figure 13). The main hyporheic

flow cell, which brings oxygen-rich surface water to the egg nest (see Figure 1 for potential

locations of the egg pocket), has most of the flux upwelling at the crest's low-pressure zone,

while a portion is entrained by the underflow and does not return to the river. Between

slightly downstream of the pit and upstream of the tailspill of the redd, the flow reaches the

egg pocket before arching back to the streambed surface. Both spatially averaged

downwelling velocities ($\bar{q}_d$, and $\bar{q}_{d,ep}$) systematically increase with the larger Reynolds and

Froude numbers, as well as redd A_R (Figure 14).
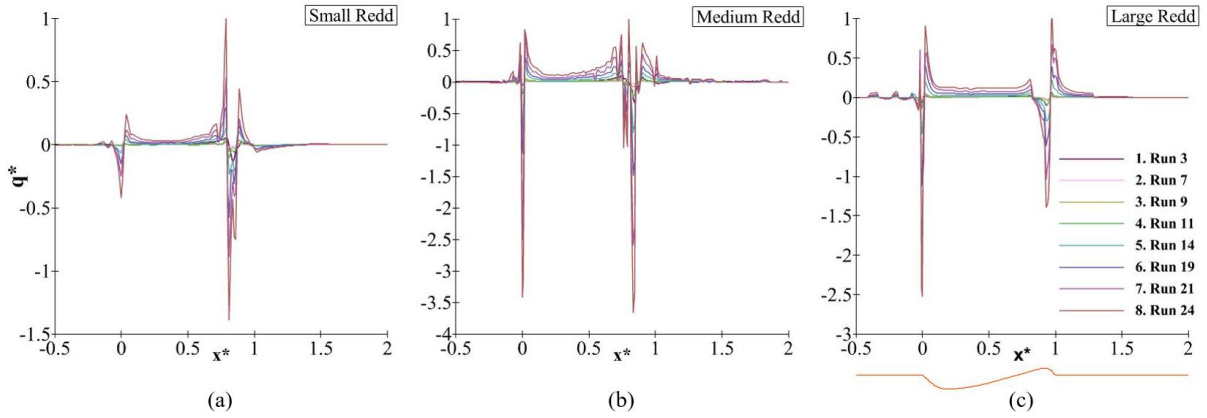
Figure 12: Normalized normal velocity distribution, $q^* = q/q_{max}$ (normal velocity normalized by its maximum value) over a (a) small redd, (b) medium redd, and (c) large redd. Note that y axes are not in the same scale to help visualize the lines. Flow is from left to right.
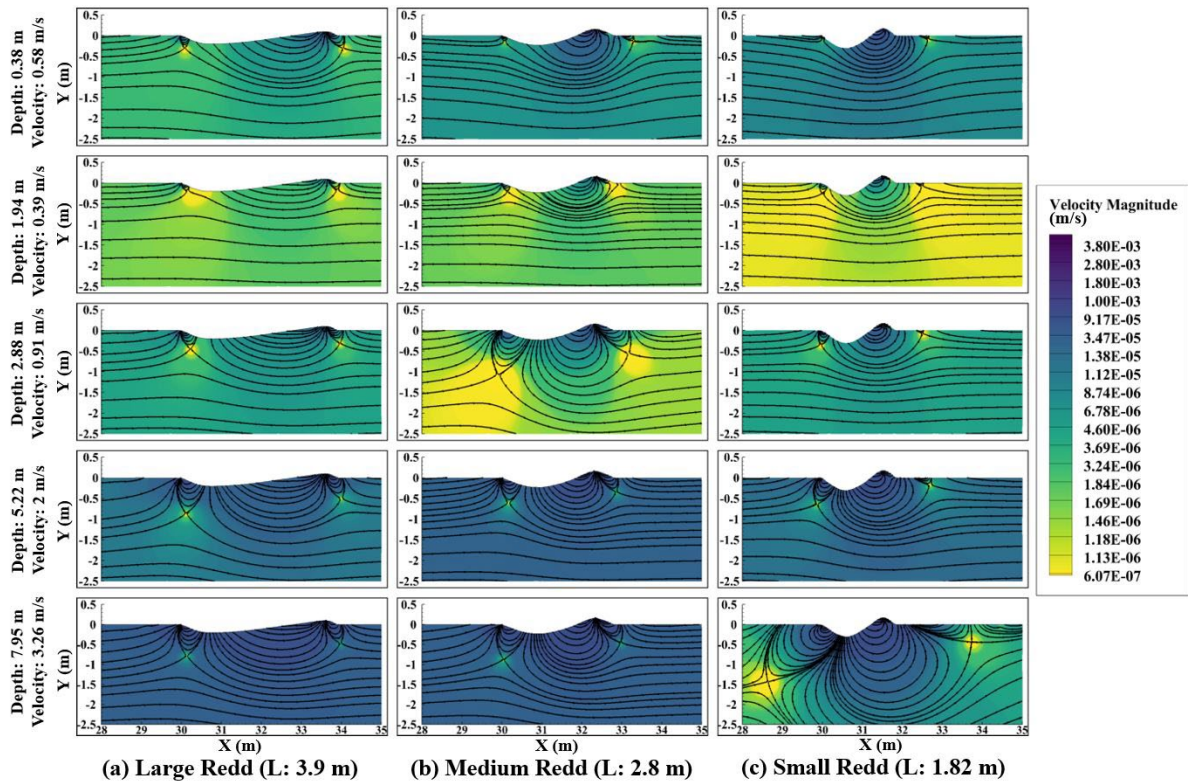
(a) Large Redd (L: 3.9 m)   **(b) Medium Redd (L: 2.8 m)**   **(c) Small Redd (L: 1.82 m)**

Figure 13: Subsurface flow characteristics for different surface hydrodynamics and three different redd sizes. Flow is from left to right.
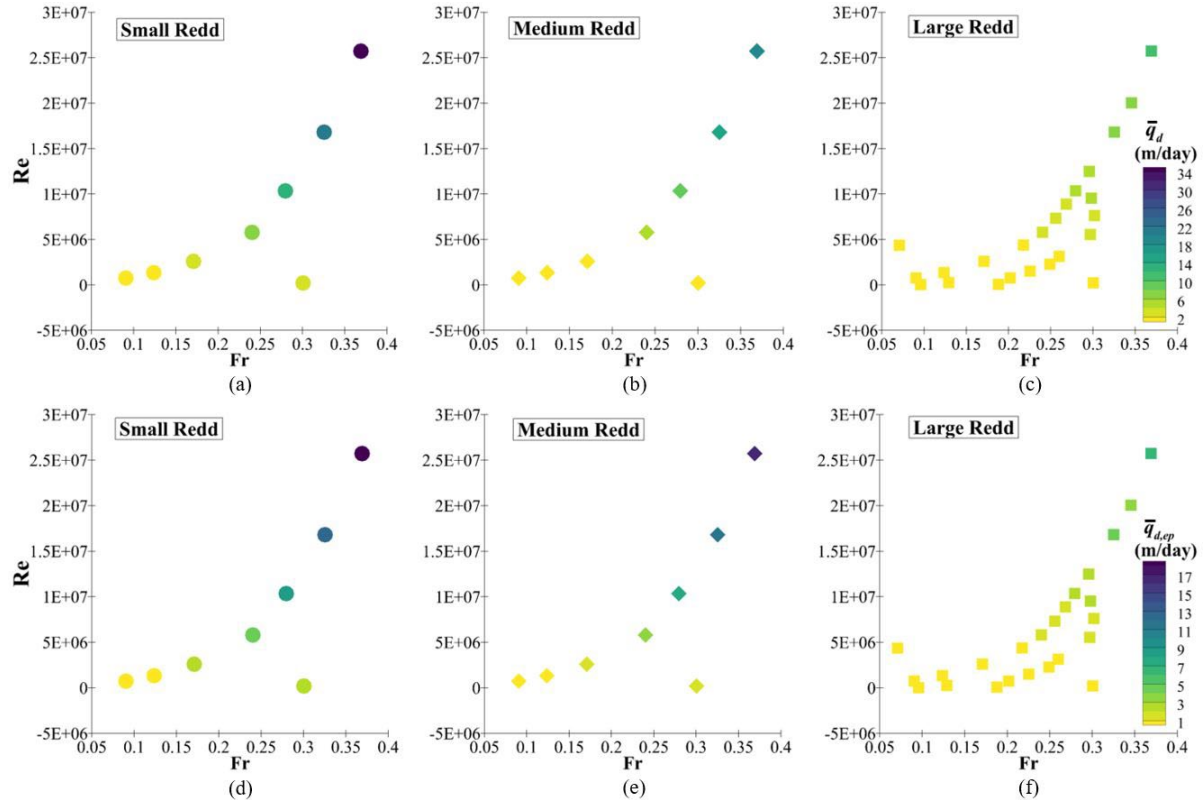
Figure 14: Averaged downwelling velocity over the redd ($\bar{q}_d$) (top panel) and between pit-tailspill region affecting the egg pocket ($\bar{q}_{d,ep}$) (bottom panel) as a function of Reynolds Number (Re), Froude Number (Fr), and Aspect Ratio (A_R).

1.7.3   Effect of categorical hydraulic conductivity

For Run 14 M (medium-sized redd), a comparison of downwelling velocities between homogenous and categorical heterogeneous hydraulic conductivities with 5 and 10 times larger hydraulic conductivities in the redd than in the surrounding undisturbed sediment (Figure 15a) resulted in similar dimensionless downwelling velocities (Figure 15b). This shows that the redd hydraulic conductivity dominates the downwelling velocity and that the influence of heterogeneity between the redd and surrounding sediment is negligible on the flow field within the redd. Spatially averaged downwelling velocity over the redd and spatially averaged downwelling velocity going through the region of the egg pocket chiefly scale linearly with the hydraulic conductivity.
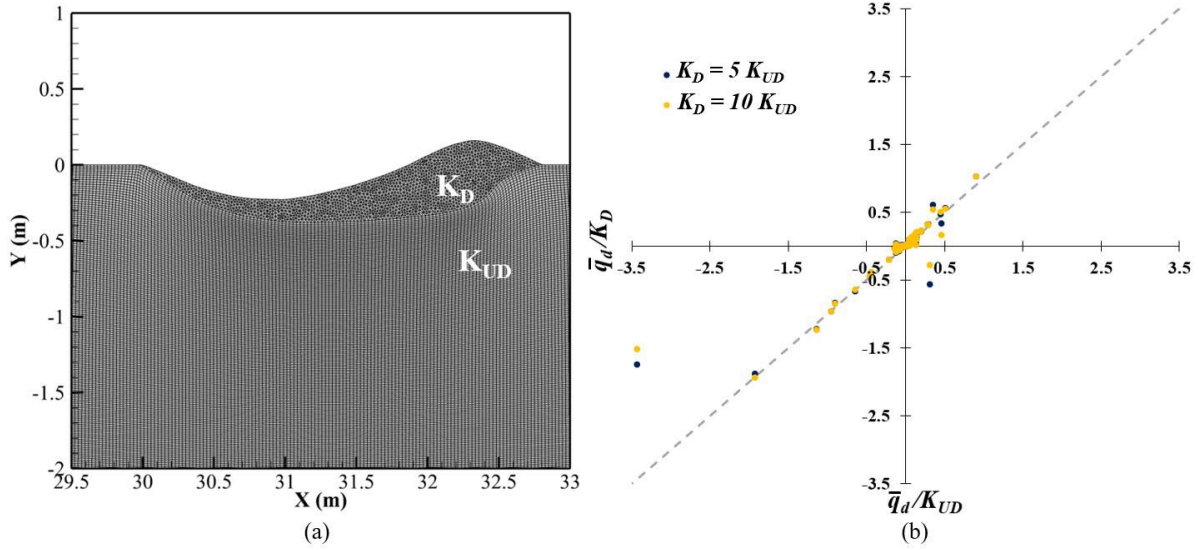
Figure 15: (a) Redd disturbed and undisturbed sediment with their hydraulic conductivities, K_D and K_{UD}, respectively. (b) Comparison between downwelling velocities normalized by the redd hydraulic conductivities for the homogeneous case (K_{UD}) and the heterogeneous (K_D) $K_D = 5 \cdot K_{UD}$ and $K_D = 10 \cdot K_{UD}$.

1.7.4 Regression predictive equations

The dimensional analysis was applied to the 3 dependent variables: relative total head drop (ΔH_R), downwelling velocity for the entire redd ($\bar{q}_d$), and downwelling velocity impacting only the egg pocket ($\bar{q}_{d,ep}$). Linear regression analysis of the log-transformed dimensionless numbers showed that Fr and Re, as well as A_R, are statistically significant ($p < 0.01$), but the relative submergence was not ($p \sim 0.8$), on both total head drop and downwelling flux. Thus, it was eliminated from the regression analysis, resulting in three independent dimensionless quantities, Fr, Re, and A_R:

$$H^* = \frac{\Delta H_R}{L} = 10^{-0.915 \mp 0.36} \cdot (A_R)^{1.274 \mp 0.177} \cdot (Re)^{0.313 \mp 0.037} \cdot (Fr)^{2.219 \mp 0.193} \qquad (4)$$

$$\bar{q}_d^* = \frac{\bar{q}_d}{K} = 10^{-1.278 \mp 0.355} \cdot (A_R)^{0.82 \mp 0.175} \cdot (Re)^{0.317 \mp 0.036} \cdot (Fr)^{1.91 \mp 0.19} \qquad (5)$$

$$\bar{q}_{d,ep}^* = \frac{\bar{q}_{d.ep}}{K} = 10^{-0.95 \mp 0.39} \cdot (A_R)^{0.784 \mp 0.192} \cdot (Re)^{0.247 \mp 0.04} \cdot (Fr)^{1.91 \mp 0.209} \qquad (6)$$

The equations report the mean values of the regression coefficients along with their standard errors, SE. Comparisons of the model predictions against the independent data sets, not used in the regression analysis, showed very good performance with $R^2 > 0.9$ and strong correlations along the 1:1 line (Figure 16).
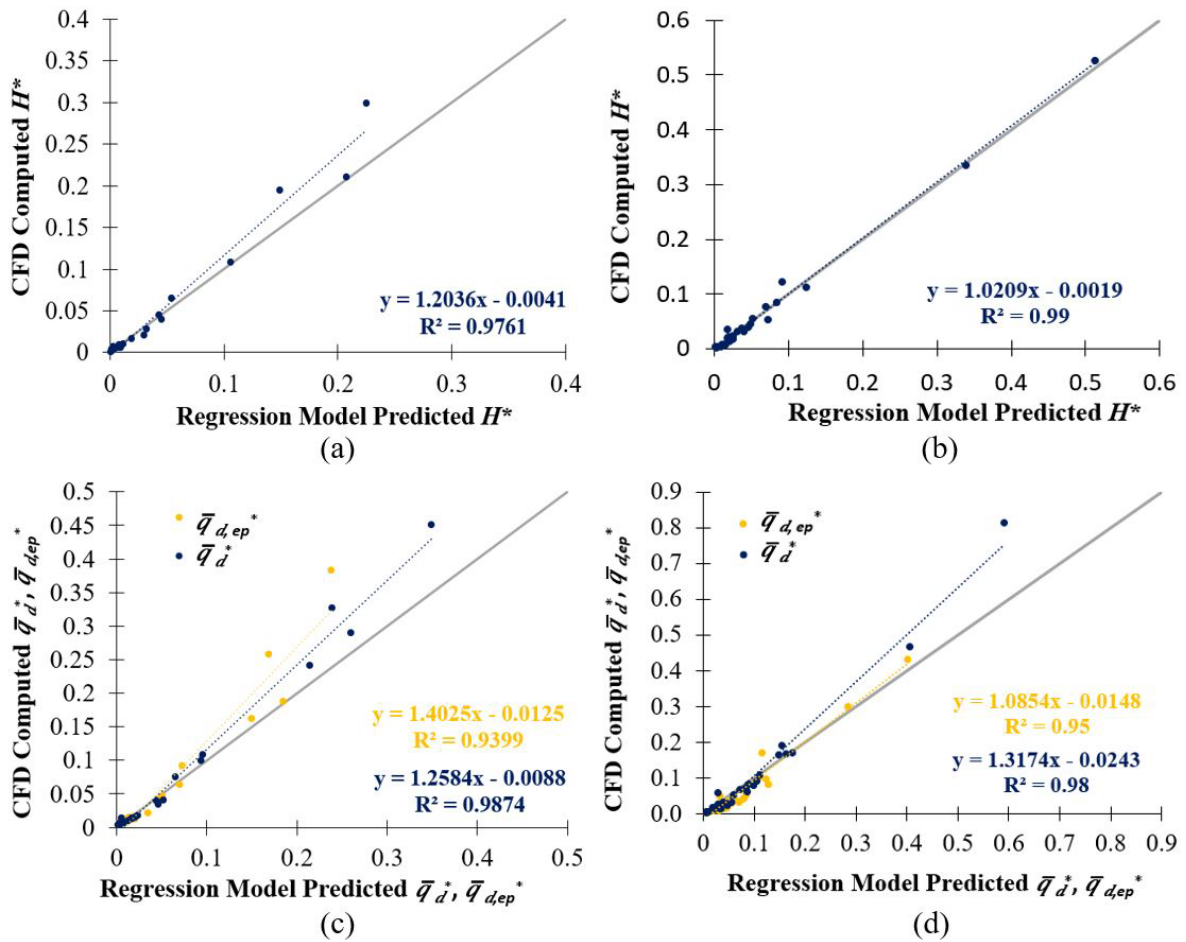
Figure 16: Linear regression plots for computed (y-axis) VS predicted (a) calibration and (b) validation of dimensionless total head drop across the redd. (c) Calibration and (d) validation of averaged downwelling velocities across the egg pocket (yellow) and entire redd (blue) for 48 runs (21 calibrations and 27 validations).

We also tested whether equation (4) can predict the total head drop over dunes, extending the

work of Fehlman (1985) (Figure 17a). The comparison shows a good fit ($R^2 \sim 0.9$), but

model predictions are 2.5 times higher than those measured in Fehlman's experiments

(Figure 17a). Therefore, we ran a simulation with a sequence of redds and dunes for the flow

conditions of Fehlman's (1985) run number 11 with the flow depth of 0.272 m and the

velocity of 0.653 m/s to test whether the presence of multiple redds would explain the

difference (diamond marker Figure 17a). The three simulations (single redd, a sequence of 15

redds, and a sequence of 15 dunes) generated similar relative total head distributions (Figure

17b) regardless of single or sequence of bedforms. The single redd has a slightly higher than

the redd sequence drop, but small such that the effect of a sequence of feature is negligible

(Figure 17b) on pressure drop.
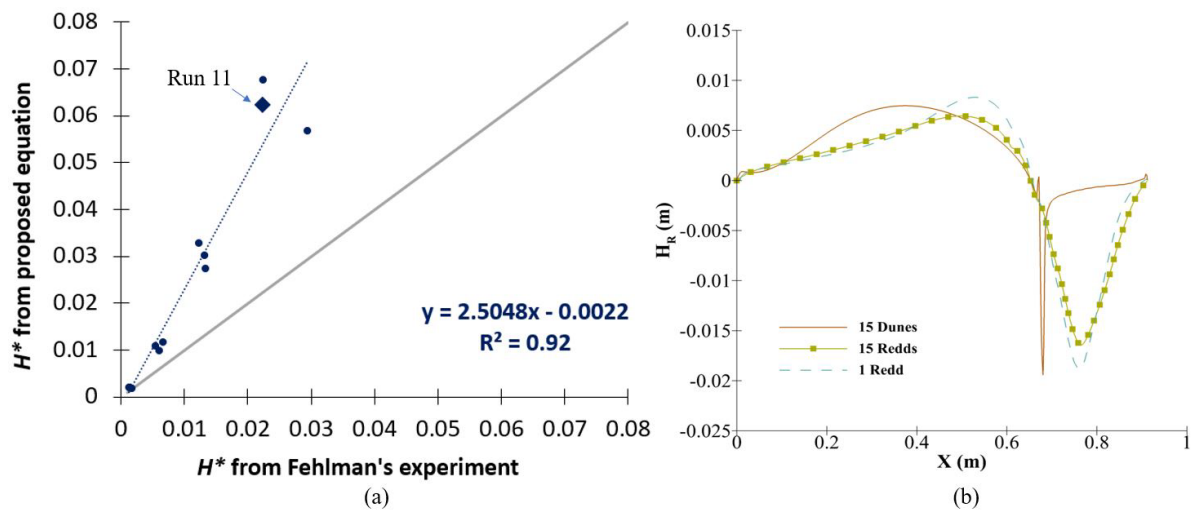
Figure 17: (a) Relative total head drop normalized by the length of the dune ($\Delta H_R/L$) across the uniform bedform for the flow hydraulics used in Fehlman's experiment for dunes using our proposed equation and (b) relative total head distribution over a sequence of 15 dunes, a sequence of 15 redds, and one redd for Fehlman's (1985) run 11. Flow is from left to right.

Although the three simulations provide similar relative total head drop, the minimum head occurs over a large portion of the redd lee side but almost in a point for dunes near the crest. The simulated dramatic drop in relative head the for the 15-dunes case, occurring around $X =$ 0.7 m, is due to the sharp edge at triangular dunes. Because the sharp and localized head drop is mainly due to the sharp corner rather than the overall dune shape, we believe a more appropriate minimum head value for the dune would be around -0.01 m rather than -0.02 H_R. This drop is also similar to that reported by Fehlman's (1985) who did not have any measurement ports at that location. This is a significant result because it implies that the proposed equation (4) can be extended to dunes by dividing H_R by a constant factor of 5 (2.5 times 2, where 2 accounts for semi-amplitude), resulting in semi-amplitude as given by equation (7) because Elliott and Brooks (1997b) used semi-amplitude rather than amplitude:

$$h_{dune} = \frac{10^{-0.915 \mp 0.36}}{5} \cdot (A_R)^{1.274 \mp 0.177} \cdot (Re)^{0.313 \mp 0.037} \cdot (Fr)^{2.219 \mp 0.193} \qquad (7)$$

where h_{dune} is the semi-amplitude ($H^*/2$).

1.8 Discussion

Our surface flow range is fairly extensive, encompassing spawning areas ranging from very shallow to very deep flows, as well as slow and fast water. Because the depth and velocity quantities are not independent as expressed through the resistance equation, e.g., Manning's equation, we did not keep one constant and change the other arbitrarily; instead, we modified them both simultaneously because an increase in discharge results in an increase in both velocity and depth. Our hydraulic scenarios also aim to replicate what is observed in the field in locations near redds. River management teams commonly use reach-averaged values, so

the flow hydraulics used are reach-averaged values rather than local flow velocities and depths over a specific redd.

We employed a VOF model that allows tracking of the free surface elevation, which helps to better represent the pressure distribution at the water-sediment interface accurately. Most computational fluid dynamics models have used a single-phase with a rigid-lid approximation. However, we used a two-phase model (flow of the water column with air above it) because both hydrostatic and nonhydrostatic-driven fluxes can significantly increase when compared to the rigid-lid approach because we are analyzing surface flows within a wide range of Froude numbers (Lee et al., 2021), and the deformation of the river's free surface may influence to redd-driven hyporheic exchange. The fixed lid approach can be beneficial where no large changes in water surface elevations occur and where the VOF method may be computationally expensive.

Our numerical modeling demonstrates the impact of salmon redd shape and size, as well as surface discharge, on the hyporheic flow inside the redd, which directly influences the embryos. As seen in earlier publications (Stonedahl et al., 2010; Wörman et al., 2007), multiscale hyporheic flows are driven by the superposition of multiple scales of geomorphic features, and multi-cell hyporheic exchange is formed when surface flows interact with a redd (Tonina & Buffington, 2009d). The near-bed pressure distribution produces the largest flow circulation at the region between the redd pit bottom and the crest, where eggs incubate. Other secondary hyporheic exchange cells whose formation and relative size are dependent on flow hydraulics and redd aspect ratio, develop adjacent to the large flow circulation. This large hyporheic exchange cell is always present and has a downstream flow direction regardless of flow hydraulics or redd size, whereas the other smaller hyporheic exchange

cells develop and grow with higher discharges and larger A_R values and can disappear with lower discharge and smaller A_R values. Another small cell is formed downstream of the tailspill for the highest A_R, which develops in size as the discharge increases. The large, constant cell, between the pit and the crest, is the most crucial for egg development as it supplies oxygen-rich surface water to the egg pocket. The downwelling flux, which refers to the movement of water from the streambed to the subsurface, was found to be positively correlated with both stream discharge and aspect ratio of the redd. This means that the generated downwelling flux increases with discharge and aspect ratio, suggesting that smaller redds with larger amplitudes may benefit from higher interstitial flows compared to large redds with smaller amplitudes. While large aspect ratios may enhance downwelling fluxes, their presence depends on several factors, including flow hydraulics, as steeper lee sides may result in grain mobility at the crest. Thus, aspect ratio is likely constrained by factors such as sediment mobility and fish behavior.

For a given redd configuration, larger discharges with the same water temperature will supply more oxygen-rich water to developing embryos as downwelling flux increases with discharge (Cardenas et al., 2016). This might have an important implication in managing water resources from dam releases or water diversion during the embryo's development. For oxygen delivery and consumption, however, both water temperature and interstitial flow velocity are important during the embryos' development stage (Martin et al., 2020). In managed rivers such as the Sacramento River, high levels of water discharge can more rapidly deplete cool water pools stored in dams and thus lead to elevated temperature exposure during the embryonic period (Anderson et al., 2022). As a result, our findings should be interpreted in combination with a biophysical model of oxygen supply and demand

for developing embryos to fully comprehend the significance of discharge for embryo survival (Martin et al., 2020). For instance, the proposed regression model for downwelling flux, equation 6, could be used to estimate the effect of regulated flow releases on egg pocket habitat quality and potential embryos survival. Downwelling velocity (equation 6) coupled with stream water temperature can inform the potential oxygen limitation within the egg pocket (e.g., Figure 3 in Martin et al 2020) and the potential proportion of embryos survival (e.g., Figure 2c in Martin et al. 2020). This may provide a valuable tool for evaluating the several management scenarios by accounting for both regulated thermal and flow regimes.

High discharge may also impact redd stability because sediment mobility increases with discharge. Therefore, grain mobility should be considered for water management during egg development when flows are increased. Although we do not know their aspect ratios, redds have been observed in reaches with the high flows simulated in this study. It is possible that they have a low aspect ratio since grains on the crest may be displaced.

Hydraulic conductivity in redds for chinook salmon was found to vary from $3 \cdot 10^{-2}$ m/s (Chapman et al., 1986) to $1.5 \cdot 10^{-4}$ m/s (Geist, 2005a; Malcolm et al., 2004) in unspawned beds. Here we show the effect of categorical heterogeneity between a newly formed redd and undisturbed material that does not focus on downwelling flow. The hyporheic flows within the egg pocket are dominated by the redd hydraulic conductivity regardless of the surrounding undisturbed condition. This result is supported by earlier simulations of Tonina & Buffington (2009c), although they did not report this behavior. This suggests that the reduction of the redd hydraulic properties over time from newly built redds toward undisturbed material (Zimmermann & Lapointe, 2005a, 2005b) can be studied by reducing the hydraulic conductivity of the homogeneous case. Thus, the advantage of the proposed

normalization of the downwelling fluxes by the redd hydraulic conductivity (equations 5, 6) is that it allows the model to be applied to different permeabilities that may vary not only temporally but also among redds.

The size and shape of salmon redd vary enormously both within and across species (Deverall et al., 1993; Evenson, 2001; Tonina & Buffington, 2009d). However, the biological implications of this phenotypic variability for oxygen supply to developing embryos have been unknown. Here, for the first time, we quantified how redd size and shape influence interstitial flows within the redd. We found that the effect of redd morphology and stream discharge on interstitial flow can be characterized primarily by the aspect ratio of the redd, along with the Reynolds number and Froude number. We found that the Reynolds number, Froude number, and aspect ratio significantly affect flow velocity within the redd using regression analysis, based on the subset of the 21 simulations that encompass the varied sizes of redd and surface discharge. The size of the redd, the velocity of the surface stream, and the depth of the flow are all represented by these variables. As Re increases, more pressure builds up on the redd, which is then modulated by the Fr and $A_R,$ causing the hyporheic flow to increase.

Flows across dunes, which have a similar form as redds, can be used to understand the influence of the redd aspect ratio on hyporheic flows. Larger head gradients and faster pore water velocities are produced by dunes with taller bedforms (Lee et al., 2020), just as they are found in our model for redds with larger aspect ratios. The total head drop found in our model, which is about twice as large as that reported in Fehlman's (1985) experiment (Figure 17), might be attributed to the shape of the redd with the pit and the hump (Figure 3 and Figure 8), while the impact of a single versus a sequence of features has negligible effect.

This allows us to propose a new equation for semi-amplitude head drop around a dune bedform, which extends that of Elliott and Brooks (1997a) by accounting for the dune aspect ratio and Reynolds number whose effects were not accounted for because of the narrow range of hydraulic variability in Fehlman's (1985) experiments.

One of the limitations of our study's separate domain analysis approach is that the pressure profile obtained from the surface waterbed is used as the pressure inlet boundary condition for coupling the surface and subsurface domains. (Broecker et al., 2019) found that not only does surface water influence the subsurface, but the subsurface also influences the surface flow conditions. However, for the range of hydraulic conductivity we used, the exchange in mass between the surface and subsurface is small and the downwelling mass flux is less than 1% of the total mass transported by the surface flow. We also modeled an intrinsically three-dimensional feature as a two-dimensional bedform. This may have introduced errors in the predicted quantities. However, these errors may be partially quantified with the work of Chen et al., (Chen et al., 2015), who compared hyporheic fluxes induced by three-dimensional vs two-dimensional dunes (see Figure 6 in (Chen et al., 2015)). Their analysis shows that the flux increases with the dune Reynolds number ($Re = \frac{UA}{\nu}$,where the length scale is the dune amplitude, A, rather than the flow depth). Their simulations were up to $Re = 25,000$ and showed that the increase in hyporheic flux for the three-dimensional case was about 2.3 that of the two-dimensional dune. Our simulations ranged between 10,000 and 1,600,000 Re such that for the deep and fast flows, our predictions could underestimate the hyporheic flux more than 2.3 folds.

Chapter 2: The role of riverine bed roughness, egg pocket location, and egg pocket permeability on salmonid redd-induced hyporheic flows

2.1 Introduction

Female salmonids bury their eggs within the hyporheic zone of gravel-bed rivers (Baxter & Hauer, 2000). They create egg nests, called redds, by excavating a pit in the streambed gravel and then covering the fertilized eggs with sediment from a second pit (Burner, 1951; Chapman, 1988; Crisp & Carling, 1989; Deverall et al., 1993; Groot & Margolis, 1991). This process results in a topographical feature similar to a dune in a two-dimensional (2D) cross-section, with a pit, and a hump called a tailspill (Bjornn & Reiser, 1991) (Figure 18). The spawning-related activity leads to the redd having a higher hydraulic conductivity, K_D, than the undisturbed streambed sediments, K_{UD}, due to the removal of fine grains and loosening of the sediment matrix (Coble, 1961; Merz et al., 2004; Tappel & Bjornn, 1983; Zimmermann & Lapointe, 2005b). Salmonid spawning activities remove fine sediments form the egg pocket, leaving the larger, clustered sediments where eggs are laid (Peterson & Quinn, 1996). This egg pocket, with an average size of 7 to 10 cm (Evenson, 2001), may exhibit a higher hydraulic conductivity, K_{EP}, than the redd, due to its larger gravel size compared to the surrounding sediment (Kondolf, 2000; McNeil & Ahnell, 1964). This higher permeability can benefit embryos because it increases hyporheic flows, bringing oxygen-rich surface water to the egg pocket (Tonina & Buffington, 2009a). These hyporheic fluxes are assumed to be induced by the dune-like shape of the redd, which causes downwelling fluxes in the pit

and upwelling fluxes downstream of the tailspill crest (Cardenas et al., 2016; Tonina & Buffington, 2009a).

Female salmonids can form multiple egg pockets within a single redd (Crisp & Carling, 1989; J. M. Elliott, 1984; Hawke, 1978; Maekawa & Hino, 1990; Van Den Berghe & Gross, 1984). Therefore, the location of egg deposition may vary within the redd, mainly between the pit and the tailspill crest (Crisp & Carling, 1989) (Figure 18). Despite these observations, research has treated redds as a homogenous feature without investigating the effects of egg pocket permeability and location on hyporheic fluxes to the incubating embryos (Cardenas et al., 2016; P. A. Carling et al., 2006; Tonina & Buffington, 2009a).
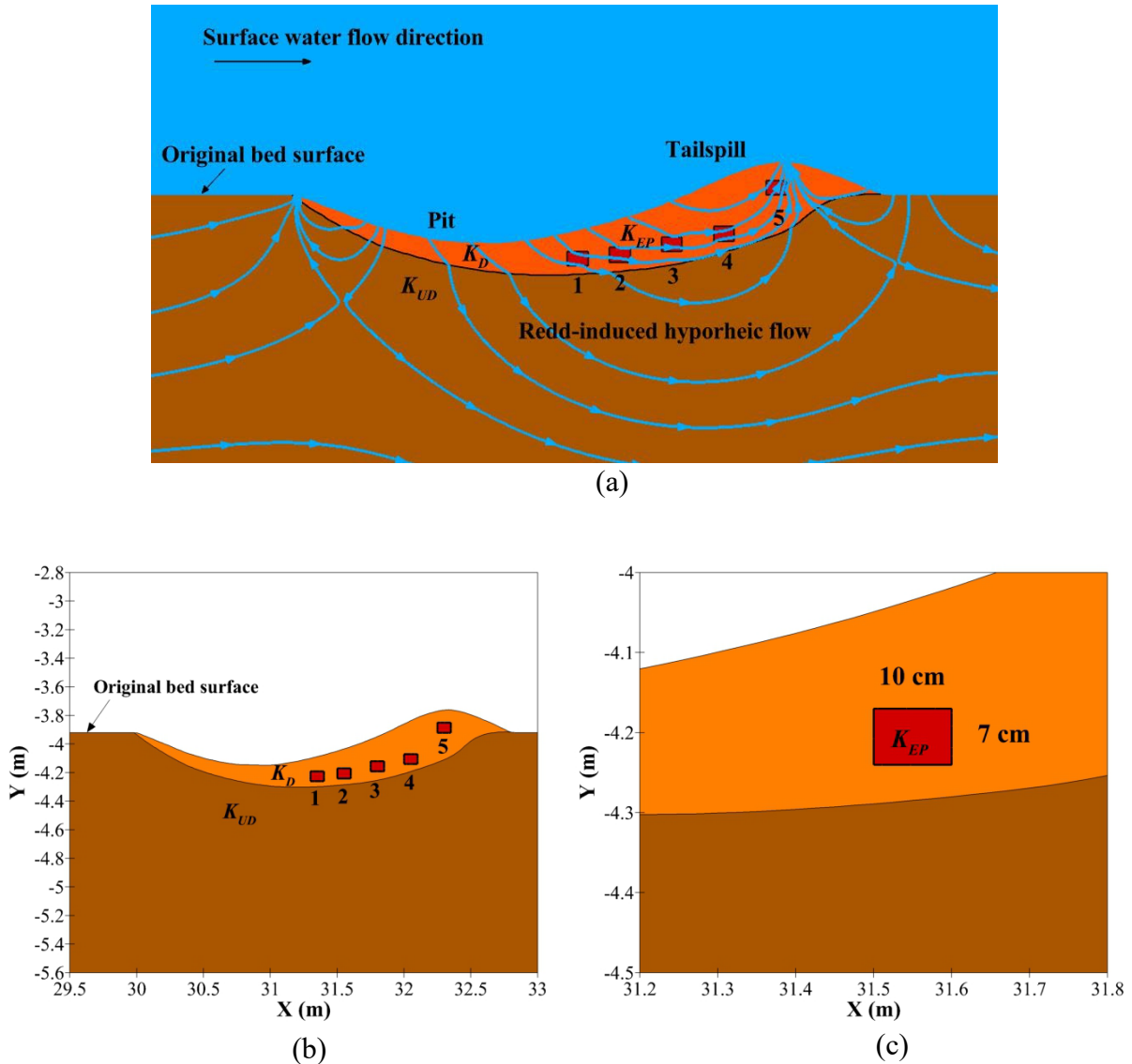
Figure 18: (a) Schematic of a redd's longitudinal profile, with egg pockets of hydraulic conductivity K_{EP} highlighted in red situated within disturbed sediment (K_D), shown in orange. The surrounding undisturbed sediment (K_{UD}) is indicated in brown, and the streamlines are included to show the subsurface flow paths. (b) Five egg pockets positioned left to right, labeled as EP_1 to EP_5, and (c) EP_2, showing the dimensions of the egg pocket. In all panels, flow direction is from left to right.

Similarly, previous research (Cardenas et al., 2016; Tonina & Buffington, 2009a) considered the redd shape as a smooth surface without taking into account the surface roughness (Evenson, 2001). Gravel-bed streams have broad grain size distributions, which create uneven surfaces characterized by grain-scale roughness (Heritage & Milan, 2009; Keulegan,

1938; Whiting & Dietrich, 1991; Wiberg & Smith, 1991). This roughness can be quantified with the standard deviation of the bed elevation, detrended from the large-scale variability caused by various bedforms (Aberle & Nikora, 2006; J. R. Cooper & Tait, 2009; Nikora et al., 1998; Smart et al., 2004).

Early studies investigated how granular porous beds affect underground water flow. Grain-scale roughness causes water to move slower within the gravel due to head variations generated by the roughness, which in turn promotes the momentum exchange between the surface and subsurface waters (Greig S. M. et al., 2006; Mendoza & Zhou, 1992; D. Zhou & Mendoza, 1993). This roughness drives microhabitat-scale exchange, resulting in surface water penetrating shallower depths and flow paths being shorter compared to bedform-driven hyporheic exchange (Hervant & Malard, 1999).

However, limited information is available regarding the impact of surface roughness on hyporheic fluxes induced by redds and how they may impact hyporheic fluxes deeper in the redd, near the potential locations of egg pockets. Surface roughness may affect the downwelling flux entering the redd but may not impact the flow reaching the egg pockets, as they may be located at depths greater than the hyporheic flow cells induced by grain-scale roughness. Consequently, we hypothesize that, even in the presence of grain-induced hyporheic flows, the flow to the egg pocket is primarily influenced by the redd-scale hyporheic flow.

The present study aims to address this hypothesis by investigating the impact of egg pocket hydraulic conductivity, their locations, the effect of multiple egg pockets within a redd, and surface roughness on redd-induced hyporheic fluxes. We used a set of numerical modeling techniques, constrained by field information, to simulate and analyze surface and subsurface

flows in a two-dimensional (2D) numerical hydraulic model. The models were simulated separately and linked through the near-bed pressure distribution, which is quantified using a two-phase (air-water) computational fluid dynamics model for surface water. We applied this modeling approach to a typical Chinook salmon (*Oncorhynchus tshawytscha*) redd under surface flow conditions observed in the Sacramento River.

2.2 Methods

2.2.1 Surface flow hydraulics

We used the 2D surface model developed by Bhattarai et al. (2023a) to simulate open channel flow surface hydraulics over a salmon redd. The model employed a two-phase (air-water) solver for the Reynolds-Averaged Navier-Stokes (RANS) equations with a realizable k-ε turbulence closure scheme in ANSYS. The volume of fluid (VOF) approach was applied to extract the water surface elevation profile where the volume fraction is 0.5, with the values of 1 or 0 indicating only water or air, respectively. A long flow domain was utilized to develop and train the flow, which included two fixed-lid sections upstream and downstream of a 45 m long two-phase domain (Figure 2a). The water-sediment interface was specified as a no-slip impermeable boundary (Cardenas & Wilson, 2007d, 2007b; Chen et al., 2015) since momentum and mass exchanges with porous sediment are considered negligible (Janssen et al., 2012). Water boundaries were defined as velocity inlet and velocity outlet conditions for the upstream and downstream locations, respectively, while air boundaries were specified as pressure outlets (Figure 2a). The model domain consisted of approximately two million quadrilateral cells, with a mean cell size of about 2.4 cm in the horizontal direction. A vertical cell size of 1.6 mm was employed at the air-water interface to accurately track the

water surface elevation. Additionally, a very small vertical cell size of approximately 0.06 mm was used near the bottom boundary. The flow was characterized by a mean slope of 0.007%, an average velocity of 1.49 m/s, and a mean depth of 3.92 m. These represent flow characteristics at the reach scale observed during egg incubation periods in a spawning reach along the Sacramento River (California, USA). These values were measured at a location with redds along the Sacramento River and correspond to run number 14 in Table 4 of Bhattarai et al. (2023a). The sediment surface was characterized by 12 rough cases and a smooth case, which was used as a reference condition (see section 2.4).

2.2.2   Groundwater flow hydraulics

The hyporheic flow was simulated with the steady-state Darcian solver in ANSYS within a 2D domain, similar to the method employed by Bhattarai et al. (2023a). The upper boundary of the domain was defined as the pressure inlet boundary, with the pressure distribution at the water-sediment interface predicted by the RANS surface model (section 2.1). The bottom boundary was treated as an impermeable slip wall boundary located 5 m below the water-sediment interface to avoid affecting the hyporheic flow cell induced by the redd. A periodic boundary condition was applied at the upstream and downstream locations of the subsurface domain boundaries. This boundary condition imposed an ambient groundwater flow of approximately 0.001 mm/s, mimicking a large-scale longitudinal groundwater flow from a valley slope. The computational mesh used has an average grid cell size of 2.5 cm horizontally and 3 cm vertically, resulting in approximately 500,000 quadrilateral cells. The hydraulic conductivity of the undisturbed bed, K_{UD}, was set to 0.0005 m/s, representing the surrounding streambed material. This value falls within the range reported in literature, where redd hydraulic conductivity values range from 0.00009–0.035 m/s (Bray & Dunne,

2017; Geist, 2005b; Hanrahan et al., 2005; Harrison et al., 2019; Malcolm et al., 2004). The hydraulic conductivity for the disturbed bed, K_D, was five times larger than K_{UD} (0.0025 m/s), representing the permeability of the redd bedform.

2.2.3   Egg pocket characteristics

Egg pockets can vary in shape and size, influenced by the digging salmonid and flow conditions. We simplified the Chinook salmon egg pocket by using a rectangular shape, facilitating easy assessment, and enabling the study of accurate flow direction into and out of the egg pocket. We chose the dimension of the egg pockets to be 10 cm in length and 7 cm in height, corresponding to the average dimensions observed by (Evenson, 2001). The hydraulic conductivity of the egg pocket, K_{EP}, is higher than that of K_D (Chapman, 1988). The mean hydraulic conductivity for fall Chinook salmon spawning areas ranged from $9 \cdot 10^{-5}$ to 0.0021 m/s in the Hells Canyon Reach of the Snake River and $5 \cdot 10^{-5}$ m/s, with a maximum value of $4.3 \cdot 10^{-4}$ m/s, in the Hanford Reach of the Columbia River (Hanrahan et al., 2005). Geist (2000) estimated hydraulic conductivity values ranging from $2 \cdot 10^{-4} - 3 \cdot 10^{-4}$ m/s near fall Chinook salmon spawning areas in the Hanford Reach. In the Columbia River, Chapman (1988) and Zimmermann & Lapointe (2005a) observed a hydraulic conductivity value of 0.029 m/s in Chinook salmon redds. Based on this information, we analyzed the effect of varying K_{EP} from 0.0025 m/s to 0.02 m/s. We defined the index $K_{EP}^{*} = \frac{K_{EP}}{K_D}$, which varied between 1 and 8, to study the effect of different hydraulic conductivities between the egg pocket and redd.

The impact of egg pocket location on the spatial average interstitial fluxes entering the egg pocket, $\bar{q}_{ep}$, was investigated by analyzing five egg pockets located both independently and

collectively within a single redd (Crisp & Carling, 1989) (Figure 18). The horizontal distances of the upstream ends of the five egg pockets from the upstream end of the redd are 1.3 m, 1.5 m, 1.75 m, 2 m, and 2.25 m, respectively. The top of egg pockets EP_1, EP_2, EP_3, and EP_4 are situated 27 cm, 25 cm, 20 cm, and 15 cm below the original bed surface, respectively, while the top of EP_5 is situated 7 cm above the original bed surface near the tailspill of the redd.

2.2.4   Streambed roughness

Natural streambed roughness varies across sites and flows due to its dependence on multiple factors, including grain shape, orientation, packing, spacing, and structural arrangements (Nikora et al., 1998). Salmonids spawn in a variety of gravel bed rivers, where grain size distributions can vary significantly (Bjornn & Reiser, 1991; Kondolf & Wolman, 1993; Tappel & Bjornn, 1983). To accurately represent the streambed roughness of a natural gravel bed river, we used a 5 mm resolution survey of a plane gravel bed surface that was water-worked in a flume (Dudunake et al., 2020; Monsalve et al., 2017). The grain size distribution of the bed had a median grain size of 10 mm and a standard deviation of 7.7 mm. Although it is not the grain size distribution of the Sacramento River, its characteristics fall within those observed in gravel-bed rivers used by salmonids (Kondolf & Wolman, 1993). Therefore, it should provide a reasonable representation of streambed elevation variability due to grain size heterogeneity. This original rough surface served as the baseline from which we created two types of roughness by scaling the vertical and horizontal distances with six constant multipliers: 0.5, 1, 1.5, 2, 2.5, and 3. Given that the surface roughness is influenced by several processes, including flow and sediment transport regimes (e.g., Buffington &

Montgomery, 1999), the two types of roughness were expected to provide two end members with R_1, an extreme roughness, and R_2, a more realistic basis for comparison against the smooth boundary.

To generate a highly rough surface, referred to as the R_1 roughness type (Figure 19a), we scaled the surface only vertically, which exaggerates the vertical protrusion of the grains. This may represent an extreme case where the grains have their b axes vertically aligned, as observed in the analysis conducted by Lee et al. (Lee et al., 2020). In contrast, the R_2 roughness represents a more natural roughness, achieved by scaling the original rough surface both vertically and horizontally with the same scaling factor (Figure 19b). Since we geometrically scaled the surface for the R_2 type, it is equivalent to increasing the grain size distribution such that the median grain size corresponds to 0.5, 1, 1.5, 2, 2.5, and 3 cm. The larger values (>2cm) fall within the range observed for salmonid spawning in large rivers (Kondolf & Wolman, 1993).We analyzed a total of six different rough beds, in addition to a smooth bed, for both R_1 and R_2, with streambed elevation standard deviations, σ_E, of 2, 4.4, 6.7, 8.9, 11, and 13.3 mm (Figure 19).
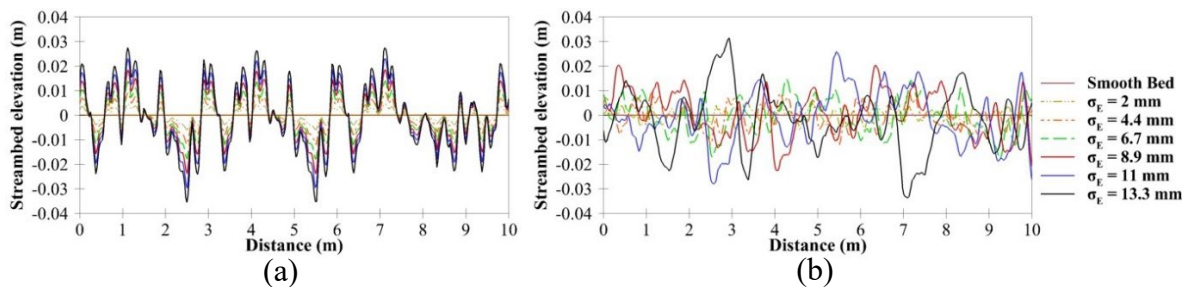
Figure 19: Zoom-in section of the streambed profiles (a) R_1 and (b) R_2.

2.3 Data analysis

To quantify the impact of the selected three treatments - surface roughness, egg pocket location, and egg pocket hydraulic conductivity - on the hyporheic fluxes, we analyzed the downwelling fluxes at various locations. We defined the mean downwelling fluxes at the water-sediment interface as $\bar{q}_d$, spatially averaged over the downwelling area of the redd. This flux represents the overall water exchange induced by the redd. We defined the mean downwelling flux, $\bar{q}_{d,ep}$, as the averaged value of the fluxes downwelling through the stoss side of the redd, flowing toward the region where egg pockets are most likely situated. The stoss side area is the same for smooth and rough surfaces. We also defined the mean spatial downwelling fluxes over the surfaces located at a sediment depth two times ($\bar{q}_{d,2d,ep}$) and three times ($\bar{q}_{d,3d,ep}$) the largest D_{50} (3 cm, σ_E = 13.3 mm) . Comparison among $\bar{q}_{d,ep}$, $\bar{q}_{d,2d,ep}$ and $\bar{q}_{d,3d,ep}$ provides an index indicating the fading effect of near-surface roughness on downwelling flux. The value of $\bar{q}_{d,2d,ep}$ and $\bar{q}_{d,3d,ep}$ represent the overall hyporheic flow that affects the area within the redd where egg pockets are primarily located. We defined $\bar{q}_{ep}$ as the mean spatial flux entering the egg pocket, indicating the flux that goes into the embryo's habitat. To eliminate the influence of hydraulic conductivity on the fluxes, we normalized them by the redd hydraulic conductivity (K_D): $\bar{q}_d^* = \frac{\bar{q}_d}{K_D}$ (dimensionless downwelling mean flux over the entire redd), $\bar{q}_{d,ep}^* = \frac{\bar{q}_{d,ep}}{K_D}$ (dimensionless downwelling mean flux toward the egg pockets at the water-sediment interface), $\bar{q}_{d,2d,ep}^* = \frac{\bar{q}_{d,2d,ep}}{K_D}$ (dimensionless downwelling mean flux toward the egg pockets at a sediment depth 2 times the median grain size), $\bar{q}_{d,3d,ep}^* = \frac{\bar{q}_{d,3d,ep}}{K_D}$ (dimensionless downwelling mean flux toward the

egg pockets at a sediment depth 3 times the median grain size), and $\bar{q}_{ep}^* = \frac{\bar{q}_{ep}}{K_D}$ (dimensionless mean flux entering an egg pocket).

To quantify the impact of surface roughness on hyporheic fluxes at the redd scale, we defined the relative total head, $H_R = H-(Y_0+z)$, where H is the total head, Y_0 is the undisturbed hydraulic depth away from the redd base, and z is the difference between the local streambed and the datum, both inclined at the same angle. Bhattarai et al. (2023a) showed that hyporheic flow at the redd scale varies with the relative total head drop (ΔH_R) between upstream and downstream locations of the redd, divided by the length of the redd. Thus, a decrease in ΔH_R due to roughness should correspond to a reduction in the hyporheic flux through the redd.

2.4 Model Performance

Bhattarai et al. (2023a) quantified the model's performance against flume experiments conducted on a redd with a smooth surface. They evaluated the agreement using the Nash-Sutcliffe coefficient (NSC), which quantifies the performance of a CFD model. The NSC values indicate the degree of agreement and are classified as follows: very good (NSC > 0.75), good (0.65 < NSC ≤ 0.75), satisfactory (0.5 < NSC ≤ 0.65), or unsatisfactory (NSC ≤ 0.5) (Moriasi et al., 2007). For the smooth bed, the model's performance was evaluated based on the comparison between streamwise velocity profiles at $X = 0.95$ m (just downstream of the crest) and $X = 1.15$ m (near the bottom of the hump). The performance was very good, as indicated by the NSC values: for flows with depths and velocities of 0.1 m and 0.2 m/s, 0.1 m

and 0.1 m/s, 0.2 m and 0.2 m/s, and 0.2 m and 0.1 m/s, the respective values were 0.954 and 0.969, 0.824 and 0.967, 0.644 and 0.923, and 0.6 and 0.845 (Bhattarai et al., 2023a).

To evaluate the model's performance under rough bed conditions, we conducted two flume experiments using a streambed surface rougher than those in Bhattarai et al. (2023a), while maintaining a similar redd size and shape (a 1/3 scaled version of an average Chinook salmon redd) in a 7 m long, 0.5 m wide, and 0.7 m deep recirculating flume. Experiments had slow (0.1 m/s) and fast (0.2 m/s) flow velocities and one mean flow depth of 0.1 m. The two velocities were near those observed at redd locations (Deverall et al., 1993). The model redd was constructed with non-spherical tetrafluoroethylene hexafluoropropylene vinylidene fluoride (THV) grains, produced by 3M, with an average diameter of 3 mm. The surface roughness of the model redd was achieved by placing a mixture of molded THV grains with different nominal diameters (7, 14, and 17 mm) on the bed. The specific gravity of the THV grains was approximately 2 with a refractive index (RI) of around 1.365. Matching the refractive index of the THV grains and the fluid allowed us to employ the non-intrusive imaging technique of stereo particle image velocimetry (SPIV). To achieve the RI match, we mixed fresh water with magnesium sulfate at a proportion of 15% by weight, causing the model salmon redd to be transparent once saturated. To minimize potential boundary effects, the redd was positioned in the middle of the flume. The inflowing water was directed through a flow straightener before entering the flume, and a weir gate was used to regulate the downstream boundary.

We utilized SPIV to map the flow field downstream of the redd crest, where complex hydraulics occur, to validate our CFD model. The starting of the redd is at $X = 0$. Upstream flow field measurements ($X = -2.04$ m) were taken to establish boundary conditions for

streamwise (V_x) and vertical (V_y) velocities (V_y constituted less than 2% of V_x), as well as turbulence kinetic energy (*TKE*) profiles for the CFD models. At the downstream boundary ($X = 2$ m), a pressure outlet was applied with a hydrostatic pressure profile (Figure S1). We took preliminary measurements upstream of the redd at distances of 15 cm and 25 cm from the wall to test the impact of wall disturbances on the measured flow field. The two measured flow fields were similar, suggesting that wall effects were negligible beyond 15 cm from the wall.
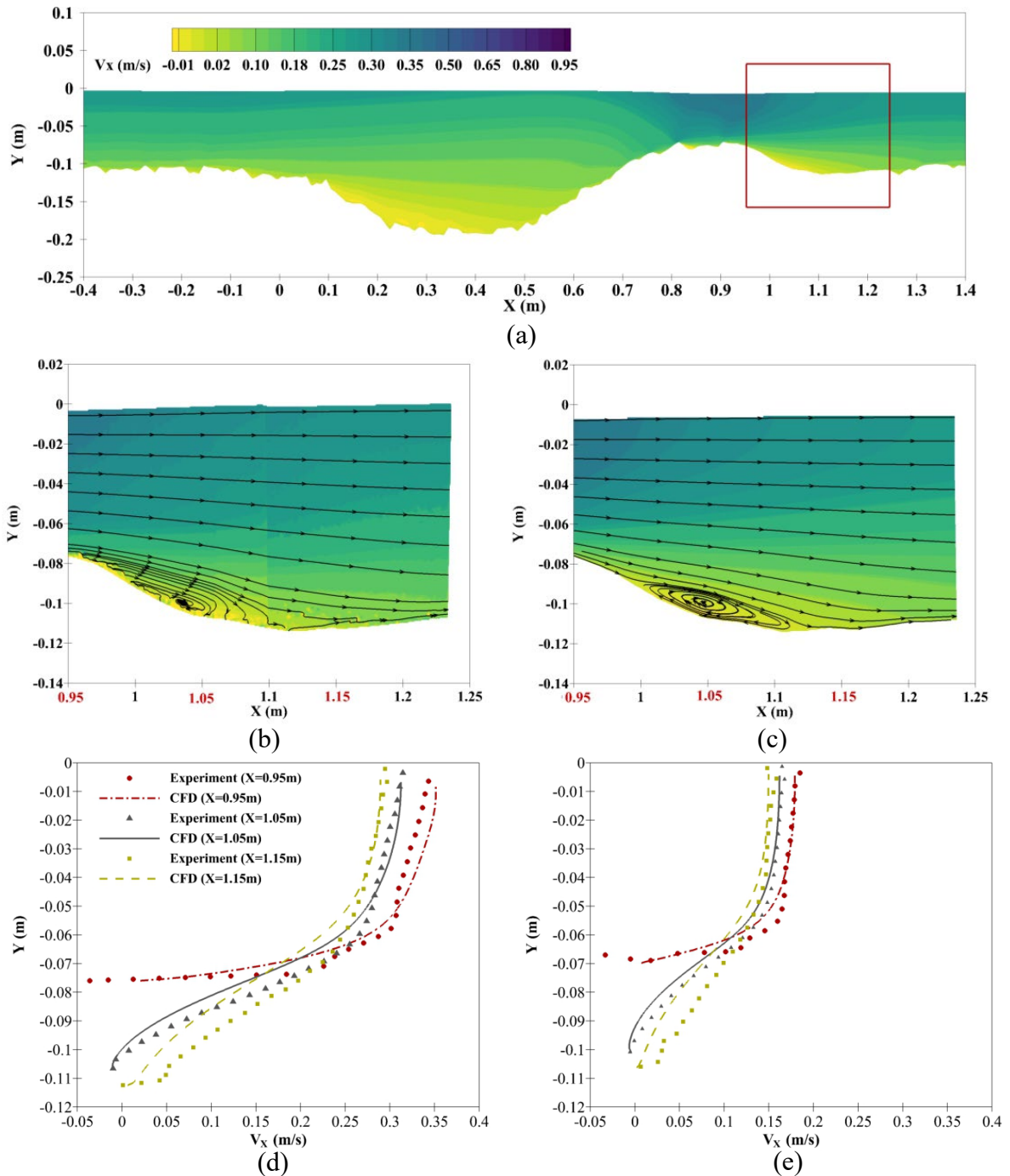
Figure 20: (a) Streamwise velocity field contours for the fast (0.2 m/s) flow case around the redd with the experimental and CFD comparison region indicated by the red square box. (b) Experimental and (c) CFD results. Comparison between the simulated (solid and dashed lines) and experimental (symbols) streamwise velocity profiles at X = 0.95 m, 1.05 m, and 1.15 m for (d) fast (0.2 m/s) and (e) slow (0.1 m/s) flows. These locations are marked by red X-labels in (b) and (c). The flow direction is from left to right.

Visual comparison of the overall size of the separation vortex and reattachment locations

shows a good agreement between the measured and predicted flow fields downstream of the

redd (Figure 20b and Figure 20c). Similarly, when comparing the streamwise velocity (V_x)

profiles just downstream of the crest ($X = 0.95$ m) and just downstream end of the redd ($X =$

1.05 m and $X = 1.15$ m), both flow cases yield very good NSC values of 0.84, 0.97, and 0.92

for fast flow, and 0.8, 0.98, and 0.9 for slow flow at $X = 0.95$ m, $X = 1.05$ m, and $X = 1.15$ m,

respectively (Figure 20d and Figure 20e). These results are consistent with those obtained by

Bhattarai et al. (2023a) in their study for the same surface discharge that also exhibit very

good NSC values.

Additionally, Bhattarai et al. (2023a) implemented the verification and validation for the

same flow discharge as studied here, using the method developed by Xing and Stern (Xing et

al., 2008; Xing & Stern, 2010, 2011), and observed a monotonic convergence of solutions for

the grid triplets and yielded validated solutions at four different testing locations. We employ

the same subsurface model that was utilized in the study conducted by Bhattarai et al.

(2023a), which compared measure and simulated interstitial flow paths within a synthetic

redd like the one studied here. These results underscore the capability of our CFD model to

predict the flow field resulting from redd-flow interaction accurately.

2.5 Results

2.5.1 Effect of egg pocket permeability

The simulated interstitial streamlines converge toward the egg pocket as K_{EP}^* increases

because of the increased flow velocity within the egg pocket (Figure 21). When $K_{EP}^* = 1$,

water consistently flows into the egg pocket from the top and upstream sides, while exiting

from the downstream and bottom sides, without deviating from the overall flow path. With

$K_{EP}{}^* > 1$, most of the water enters the egg pocket from the upstream side and exits from the

downstream side. Additionally, a portion of the water flow is diverted into the egg pocket

from the top and bottom and exits from these sides as well. For the $K_{EP}{}^* = 8$, the inflow

increased by about 71% from the case with $K_{EP}{}^* = 1$ (Figure 21f). Although the local egg

pocket hydraulic conductivity has some impact, the primary control of the interstitial flow

into the egg pocket is still predominantly governed by the overall permeability of the redd,

because even the 8-fold increase in the egg pocket hydraulic conductivity (800% increase in

permeability) results in only approximately a 71% increase in $\bar{q}_{ep}^*$.
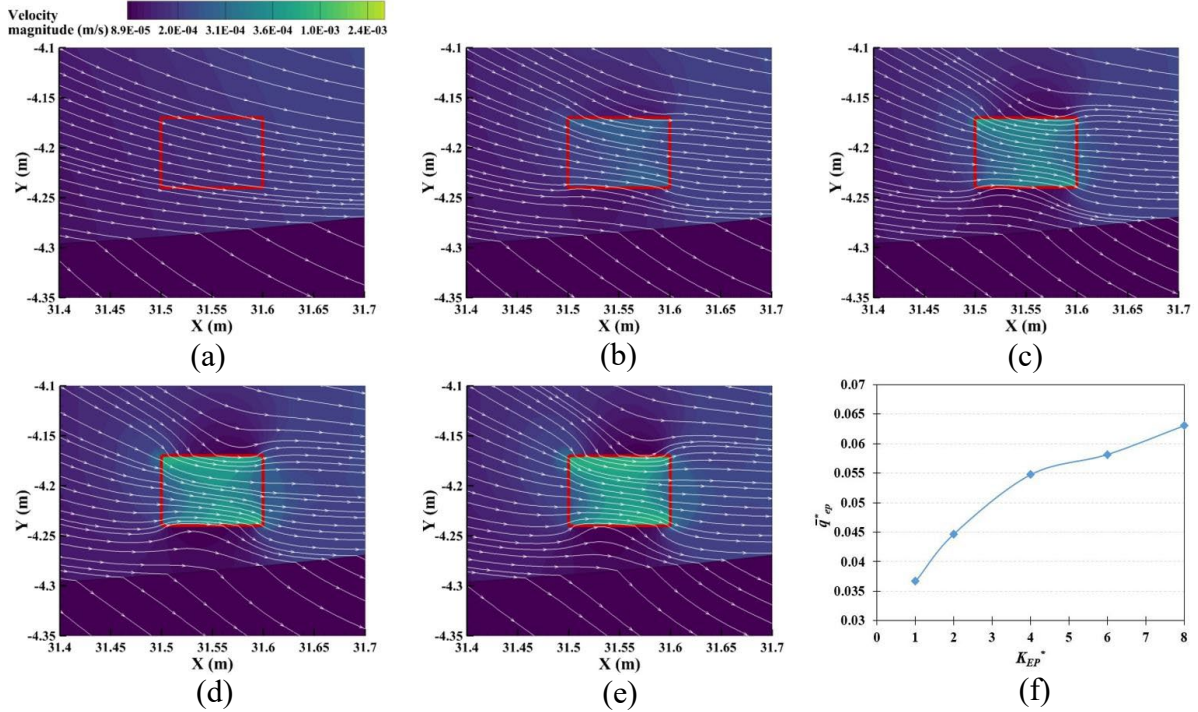
Figure 21: Flow streamlines in and around the egg pocket (EP_2) with different permeabilities for the smooth case ($\sigma_E = 0$). Their corresponding hydraulic conductivities (K_{EP}) are (a) $K_{EP} = K_D$, (b) $K_{EP} = 2 \cdot K_D$, (c) $K_{EP} = 4 \cdot K_D$, (d) $K_{EP} = 6 \cdot K_D$, and (e) $K_{EP} = 8 \cdot K_D$. (f) The flux entering the egg pocket, normalized by the disturbed bed hydraulic conductivity, $\bar{q}_{ep}^* = \frac{\bar{q}_{ep}}{K_D}$, where $K_D = 0.0025$ m/s, plotted against different normalized egg pocket hydraulic conductivities ($K_{EP}^* = \frac{K_{EP}}{K_D}$).

2.5.2 Effect of egg pocket location

Interstitial flows passing through the egg pockets increase with the distance downstream of the redd pit from EP_1 to EP_5 (Figure 22). Specifically, egg pocket EP_5, located in the upwelling region, receives over five times the flux compared to EP_1. The flux entering each egg pocket at various locations is largely independent of the presence of additional egg pockets within the redd (Figure 22). The variations in interstitial flow entering any given egg pocket between simulations with or without additional egg pockets are minimal, amounting to less than ~9%, which could be due to the influence of adjacent egg pockets on the flow dynamics.
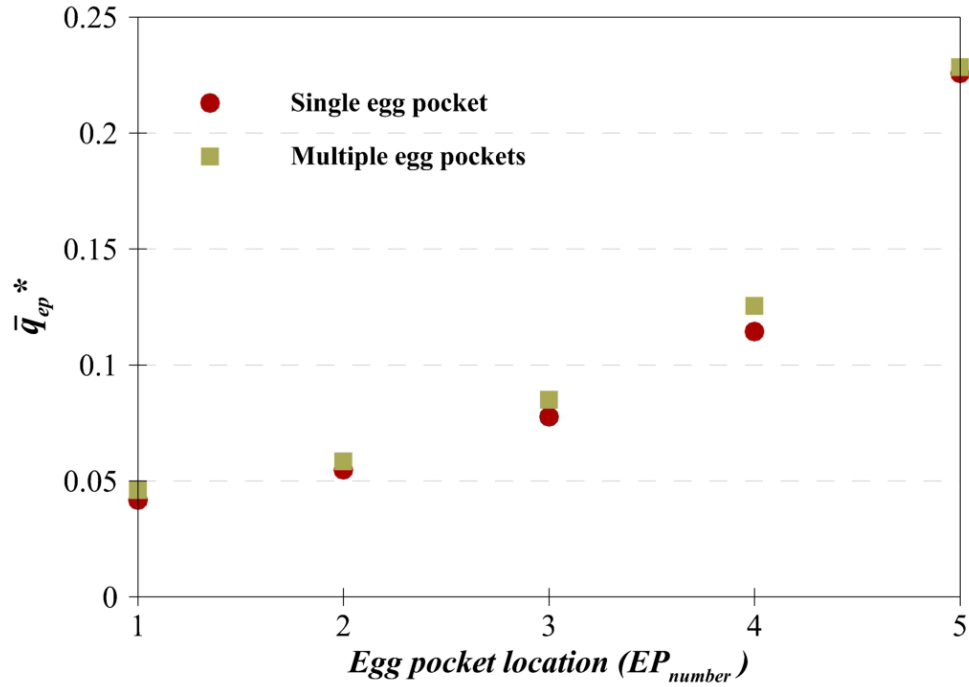
Figure 22: Normalized flow velocity entering the egg pocket ($\bar{q}_{ep}^* = \dfrac{\bar{q}_{ep}}{K_D}$, with $K_D = 0.0025$ m/s) at different egg pocket locations for the smooth case ($\sigma_E = 0$).

These results are further supported by visual inspection of the streamlines, which indicate similar trends for both single and multiple egg pockets. Moreover, there is a noticeable overall increase in interstitial flow as the egg pocket is positioned closer to the redd crest (Figure 23).
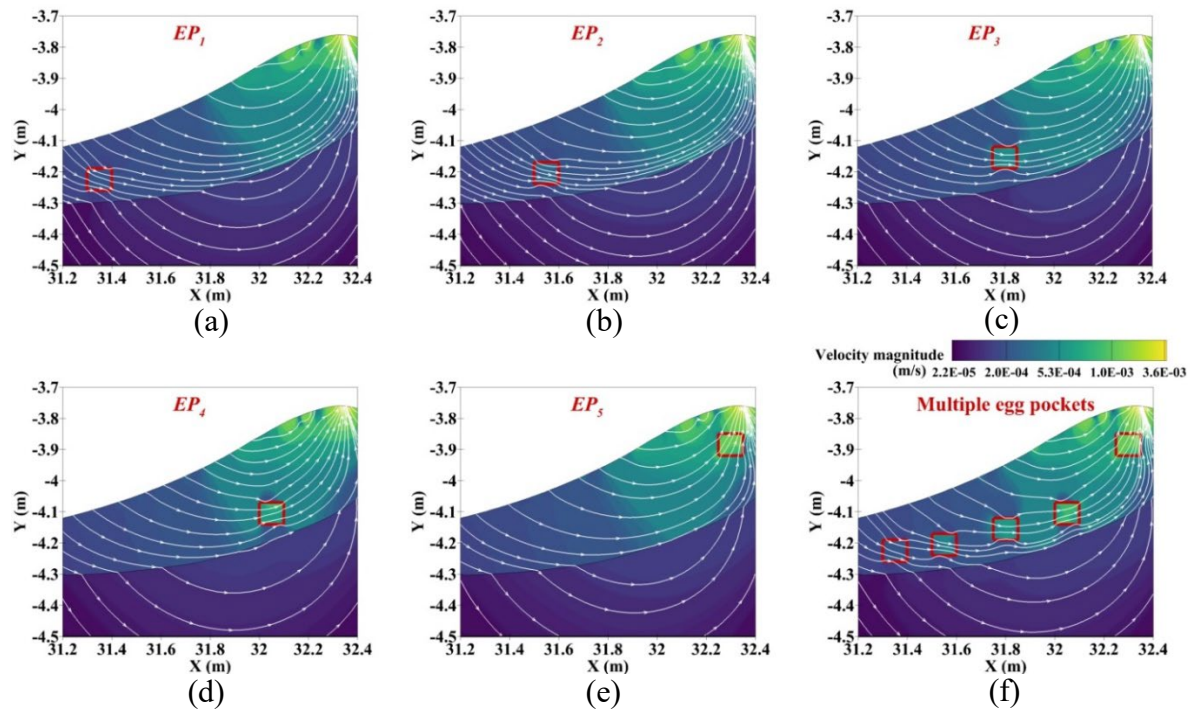
Figure 23: Visualization of flow streamlines for (a-e) individual egg pockets and (f) multiple egg pockets located at different positions within a single redd for the smooth case ($\sigma_E = 0$). All the egg pockets have the same hydraulic conductivity ($K_{EP} = 4 \cdot K_D$). Flow is from left to right.

2.5.3 Effects of bed roughness

The downwelling fluxes are influenced by the interaction between surface hydraulics and the redd shape with a smooth bed surface, as demonstrated by Bhattarai et al. (2023a). They showed that the relative total head drop (ΔH_R) between upstream and downstream locations of the redd, as well as the downwelling flux through the redd, increases with the discharge and the redd aspect ratio ($A_R = A/L$) for a smooth surface.

However, when the redd has a rough surface of type R_1, the ΔH_R decreases as R_1 increases, with the smooth bed exhibiting the largest ΔH_R (Figure 24a). This decrease in ΔH_R is attributed to local head variations that consume energy at the local level, resulting in a smaller overall relative total head drop. In contrast to the impact on ΔH_R observed with R_1

roughness, the case of R_2 roughness does not show a significant difference in ΔH_R compared to the smooth bed case. However, the head profiles do exhibit oscillations around the head profile of the smooth bed due to localized head variations (Figure 24b).

Superimposed onto the redd-induced head profile, there are localized small head drops that occur at the roughness scales that result in numerous localized hyporheic cells formed within the larger hyporheic cell between the pit and tailspill (Figure 25a). This highlights the fact that an increase in vertical roughness (R_1) leads to the formation of local hyporheic cells, with the size of these cells growing as R_1 increases. The local hyporheic cells identified for the maximum R_1 had an average depth of $2 \cdot D_{50}$ of roughness $\sigma_E = 13.3 \ mm$, and lengths ranging from 5 cm to 25 cm, depending on the presence of local roughness features. The local hyporheic flow cells due to grain roughness are much shallower and subdued for R_2 compared to R_1 (c.f., Figure 25a and Figure 25b). For a smooth bed, the flow above the egg pocket downwells from the area between the pit and the tailspill (stoss side of the redd) directly entering the egg pocket. However, when the bed is rough, it can significantly influence the flow direction, potentially causing the flow to enter the egg pocket from a different zone. As the spatial distribution of roughness can vary randomly due to sediment transport, this variability can affect the origin of the flowline entering the egg pockets. In certain cases, the presence of roughness can amplify the effect of the redd topography, resulting in a small area of the redd surface contributing most of the flow that enters the egg pocket. This is illustrated in Figure 25a, where the flow entering the egg pocket originates from the bottom of the pit. The control of roughness on the flow path is less noticeable for R_2 (Figure 25b).

The downwelling flow at the water-sediment interface increases with R_1 (Figure 26a)

primarily due to shallow and fast roughness-scale hyporheic flow cells, as previously

observed in rough beds but without a redd (Reidenbach et al., 2010). The depth of

penetration of these localized hyporheic flow cells becomes larger and faster with increasing

R_1 roughness (Figure 25a), because of the increase in local head drops (Figure 24a).

Conversely, the downwelling fluxes are negligibly affected by R_2 roughness (Figure 26a).

However, the graphs of downwelling velocities and roughness do not exhibit monotonic

relationships, but rather show trends with some uncertainty, primarily influenced by the

random nature of roughness where peaks and troughs are placed over the redd. This

roughness size and distribution could have been amplified by the redd's shape, which

resulted in a minimum value for R_1 and a maximum value for R_2 for the downwelling

velocity at $\sigma_E = 2$ (Figure 26a). These values could vary slightly if the roughness were

resampled.
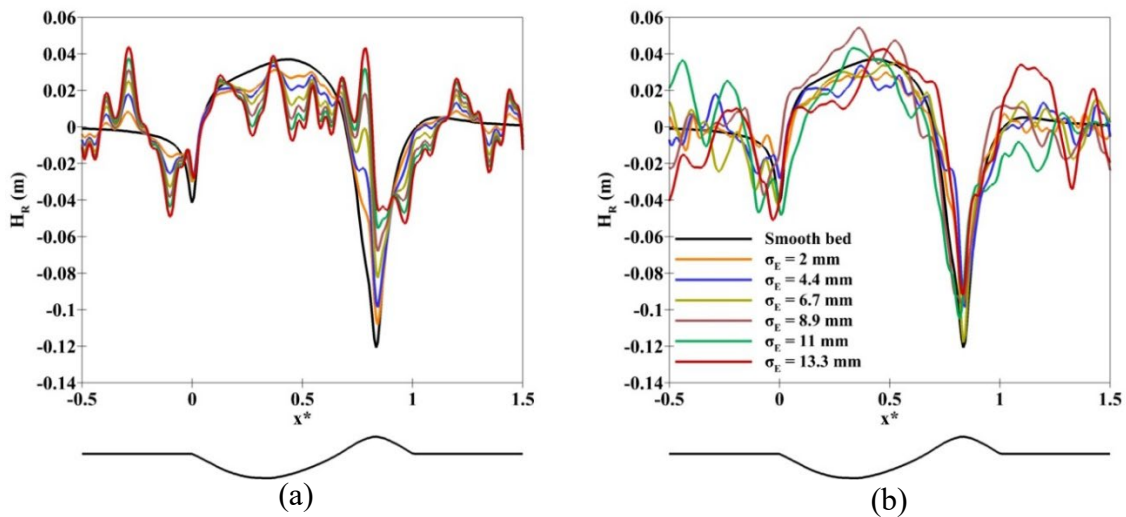
Figure 24: Relative total head (H_R) as a function of dimensionless distance (x^*), defined as the distance normalized by the redd wavelength ($x^* = \frac{x}{L}$), over the redds of roughness types (a) R_1 and (b) R_2, along with the corresponding illustration of the smooth redd profile indicating redd location. Flow is from left to right.
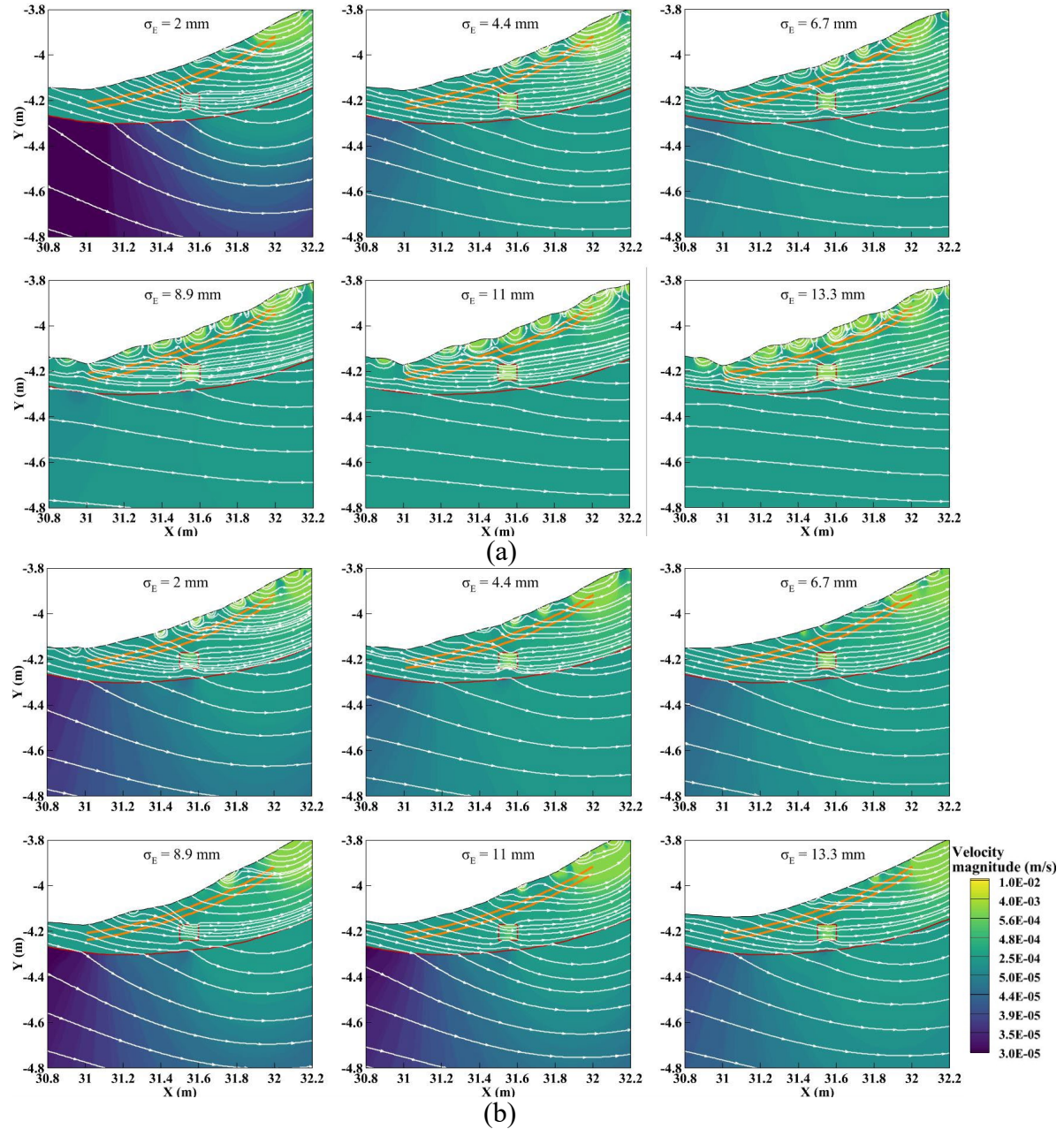
Figure 25: Subsurface flow characteristics for different stream bed roughness (a) R_1 and (b) R_2 with egg pocket EP_2 of hydraulic conductivity $K_{EP} = 4 \cdot K_D$, situated inside the redd. The orange curves indicate the locations at which downwelling fluxes are extracted at 2 times (top) and 3 times the D_{50} of a $\sigma_E = 13.3$ mm roughness. Flow is from left to right.
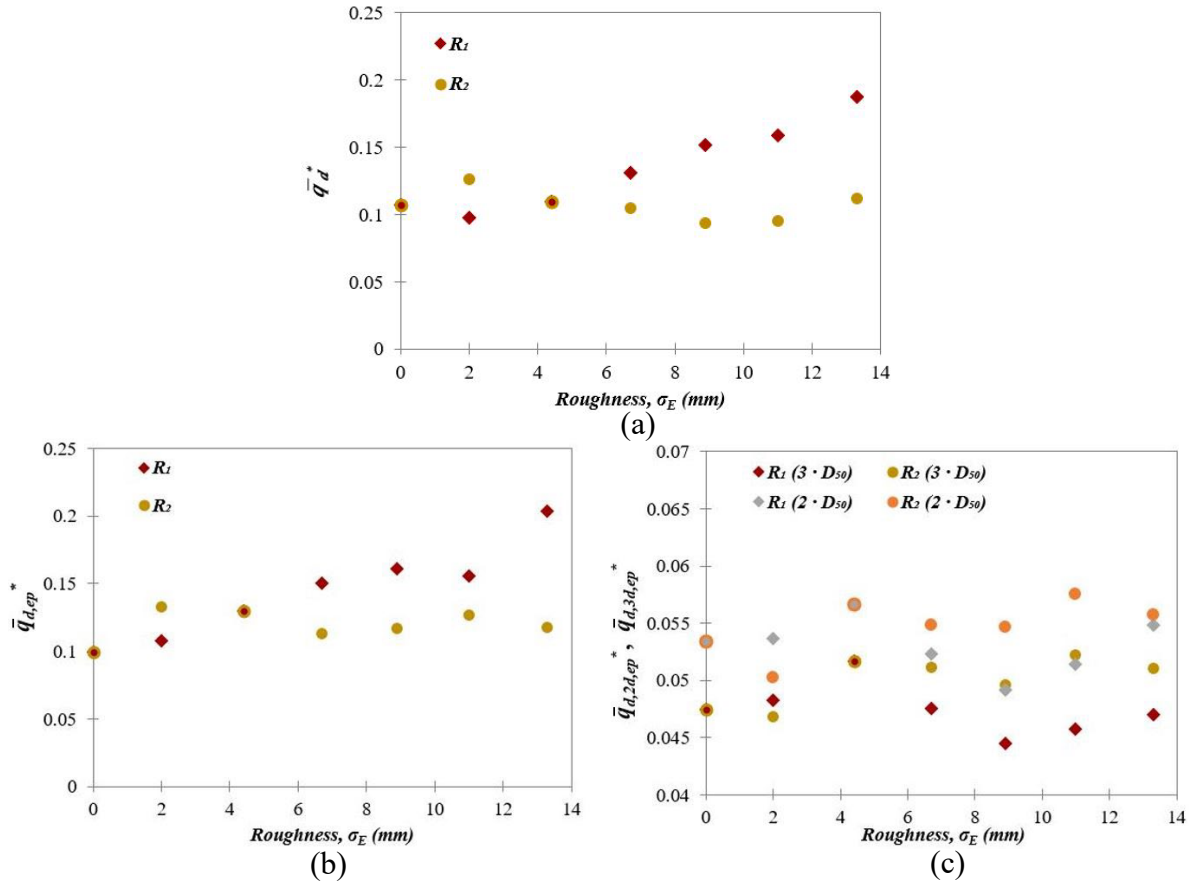
Figure 26: (a) Average downwelling velocity normalized by the disturbed bed hydraulic conductivity over the entire redd, $\bar{q}_d^* = \frac{\bar{q}_d}{K_D}$, (b) at the water-sediment interface between the pit and tailspill region ($\bar{q}_{d,ep}^* = \frac{\bar{q}_{d,ep}}{K_D}$) and at (c) $2 \cdot D_{50}$ ($\bar{q}_{d,2d,ep}^* = \frac{\bar{q}_{d,2d,ep}}{K_D}$) and, $3 \cdot D_{50}$ ($\bar{q}_{d,3d,ep}^* = \frac{\bar{q}_{d,3d,ep}}{K_D}$) for two types of rough beds, R_1 (diamond) and R_2 (circle).

The interstitial flow velocity gradually decreases further into the redd. The downwelling flow velocity at the water-sediment interface (Figure 26b) is nearly two times higher than at regions $2 \cdot D_{50}$ (6 cm) and $3 \cdot D_{50}$ (9 cm) below the smooth bed surface (Figure 26c). Moreover, the flow velocity at $2 \cdot D_{50}$ is only slightly higher than that at $3 \cdot D_{50}$ (Figure 26c), indicating that most of the flow reduction occurs within the first shallow band of $2 \cdot D_{50}$. Notably, the flow at $3 \cdot D_{50}$ is minimally influenced by the type and amount of roughness (Figure 26c). Consequently, the surface roughness may have a negligible effect on the flux directed toward the egg pockets.

In our comparison of the downwelling flow between the two rough beds (R_1 and R_2 of $\sigma_E =$ 13.3 mm), we found that the average downwelling flow in the region that affects the egg pocket significantly varied at the water-sediment interface (Figure S2). However, deeper within the redd, the mean downwelling flow variation was not substantial. At the water-sediment interface, the average downwelling flows, $\bar{q}_{d,ep}$, for R_1 and R_2 were observed to be 0.51 mm/s and 0.294 mm/s, respectively (Figure 26b). However, at depths of $2 \cdot D_{50}$ and $3 \cdot D_{50}$, the variations in average downwelling flows becomes smaller, with values of 0.137 mm/s and 0.139 mm/s for R_1 and R_2, respectively, at $\bar{q}_{d,2d,ep}$, and 0.117 mm/s and 0.128 mm/s for R_1 and R_2, respectively, at $\bar{q}_{d,3d,ep}$ (Figure 26c). Therefore, the impact of varying surface roughness types on the average downwelling flow becomes less significant deeper within the redd, with negligible variations of less than 9.5% for $\bar{q}_{d,3d,ep}$.

Although the hyporheic flux entering an egg pocket, $\bar{q}_{ep}^*$, initially increased with bed roughness, this increase may be different from the 9.5% that was quantified for the spatially averaged downwelling flow at a depth of $3 \cdot D_{50}$. For instance, the average value of $\bar{q}_{ep}^*$, shows an approximately 45% increase compared to the smooth bed for both R_1 and R_2 types of roughness for EP_2 (Figure 27a).

The impact of K_{EP}^* on $\bar{q}_{ep}^*$ increase from 71% for smooth bed to 92% for a bed with roughness of $\sigma_E = 4.4$ mm, when K_{EP}^* is increased by 8-folds (Figure 27b). This further supports the observation that the overall redd hydraulic conductivity primarily controls the overall flow through the egg pocket.
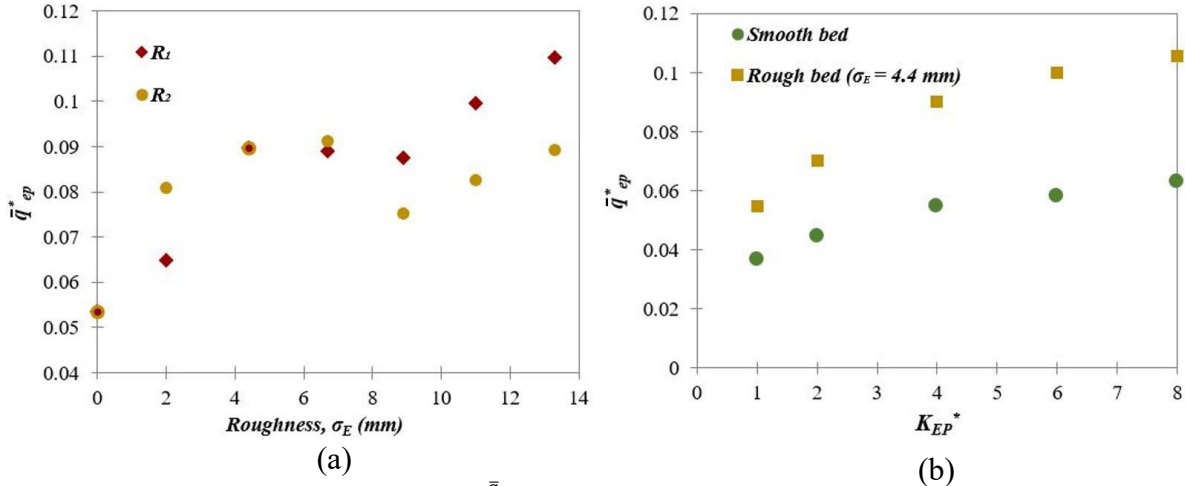
Figure 27: (a) Normalized flux ($\bar{q}^*_{ep} = \frac{\bar{q}_{ep}}{K_D}$) entering the egg pocket, EP_2, of hydraulic conductivity $K_{EP} = 4 \cdot K_D$ plotted against rough waterbeds R_1 (diamond) and R_2 (circle), and (b) Normalized flux ($\bar{q}^*_{ep} = \frac{\bar{q}_{ep}}{K_D}$) entering the egg pocket, EP_2, plotted against different normalized hydraulic conductivities ($K_{EP}{}^* = \frac{K_{EP}}{K_D}$).

2.6 Discussion

Previous studies have investigated the effect of the interaction between surface hydraulics and redd shape and size (Bhattarai et al., 2023a; Cardenas et al., 2016). The recent work of Bhattarai et al. (2023a) shows an increase in mean downwelling hyporheic flux with stream discharge and redd aspect ratio. An increase in stream discharge results in an order of magnitude increase in the downwelling fluxes, while an increase in redd aspect ratio results in several tens of percent increase in the downwelling fluxes. The redd hydraulic conductivity is a significant controlling factor that exhibits a linear impact on the fluxes. Tonina and Buffington (2009a) showed that the increased permeability of the redd sediment due to spawning activity has a primary impact on the interstitial fluxes. Furthermore, Bhattarai et al. (2023a) showed that the redd permeability controls the redd-induced hyporheic fluxes, regardless of the undisturbed streambed permeability. Our analysis revealed a secondary impact, where the increased permeability of the egg pocket, in

comparison to the overall redd permeability, contributes to the heterogeneity and the additional permeability observed within the redd. Specifically, an 8x (800%) increase in the egg pocket permeability compared to the redd permeability leads to a 71% increase in the mean flux entering the eggs. Here, we estimate that the egg pocket permeability, K_{EP}, is higher than that of the overall redd permeability because of the accumulation of large particles that form the structure of the egg pocket (Peterson & Quinn, 1996). However, female salmon lay their eggs in large numbers within the large interstices, which may substantially reduce the egg pocket permeability. This effect has not yet been quantified to the best of our knowledge. Thus, K_{EP} values may be similar to those of the overall redd. The K_{EP} effect is also smaller than that of the effect due to the egg pocket location within the redd. The location of the egg pocket within the redd can significantly vary, resulting in several-fold changes in the interstitial flow entering the eggs.

Egg pockets can exist at multiple locations within a redd, and they experience different interstitial flows. Shallower egg pockets may experience higher $\bar{q}^*_{ep}$ compared to deeper egg pockets, but they may also face a higher risk of being excavated by erosion during high flows. The variability in predicted interstitial flows may be influenced by the uncertainty surrounding the location of the egg pocket, more so than the hydraulic conductivity attributed to the egg pocket itself. Within the range of egg pocket locations studied in this research, this uncertainty can be as much as five times higher than the variability caused by $K_{EP}^* > 1$. Moreover, this level of uncertainty is larger than the influence of surface roughness on $\bar{q}^*_{ep}$. Whereas here we studied 5 egg pocket locations, future research could provide better constrains on the impact of egg pocket hydraulic conductivity, the number of egg pockets within the redd, and their spatial arrangement on hyporheic fluxes.

Salmonids may spawn in streambeds with a wide range of sediment, ranging from fine gravel to cobbles, which can result in significant variations in surface roughness. Spawning activity, whether in high or low densities, has the potential to modify streambeds through sediment mixing (Gottesfeld et al., 2004), fines purging (DeVries, 2012), coarsening and sorting of surface grains (Kondolf & Wolman, 1993), and loosening of grain packing (Montgomery et al., 1996). These alterations are beneficial for salmon reproduction success as they promote hyporheic flow that oxygenates eggs and removes metabolic waste from egg pits (Chapman, 1988; Tonina & Buffington, 2009a). Our results show that bed surface roughness has a discernible effect on the downwelling flow near the water-sediment interface over the redd. At the roughness scale, locally generated pressure gradients give rise to short and shallow hyporheic exchange cells imposed over the larger redd-induced hyporheic exchange. In flat beds, Dudunake et al. (2020) showed that grain roughness may generate mean hyporheic depths up to 26 times the median grain size. Our study shows that the redd shape constrains these fluxes to a superficial layer that is approximately three times the median grain size. The current study demonstrates that the impact of streambed roughness on interstitial flows, $\bar{q}_{ep}^{*}$, near the egg pockets is primarily controlled by the redd shape, regardless of roughness type (R_1 or R_2). However, the impact of roughness on $\bar{q}_{ep}^{*}$ depends on egg pocket location. Potentially, species with smaller redds, where egg pockets are located at shallower sediment depths compared to Chinook salmon redds, may benefit from roughness-induced flows. Nevertheless, smaller fish typically spawn in finer sediment than Chinook salmon, and their redds may have higher aspect ratios, potentially constraining the roughness-induced hyporheic flows. The potential for variability in this relationship across different roughness types and redd shapes has not been thoroughly investigated. Therefore, future work could

explore this further by comparing the effects of different roughness types on hyporheic fluxes across a range of redd shapes.

Building on the study of Bhattarai et al. (2023a), which suggest that the overall redd shape impacts the flow rate into the egg pocket, this study adds that the flow rate is also influenced by the egg pocket hydraulic conductivity and the position of the egg pocket. Analyses based on a smooth redd surface with a single redd hydraulic conductivity may provide a good indication of the mean downwelling fluxes, which the egg pocket may experience. For instance, the normalized downwelling flux for the smooth case, $\sigma_E = 0$, ($\bar{q}_{d,ep}^* = 0.1$) (Figure 26b) is similar to the flux into EP_2 for the roughest bed, $\sigma_E = 13.3$ mm, ($\bar{q}_{ep}^* = 0.11$) (Figure 25a) and the highest egg pocket permeability analyzed in this study. The equations for predicting downwelling flux proposed by Bhattarai et al. (2023a) can be used to quantify $\bar{q}_{d,ep}^*$. These values are then affected by uncertainty due to surface roughness and egg-pocket permeability and locations. These uncertainties could be estimated with the analysis provided in the current study. Our analysis suggests that the uncertainty in egg pocket location has a greater impact on the variability of $\bar{q}_{ep}^*$ than egg pocket permeability and surface roughness. This suggests that a single redd may have different eggs surviving because egg pockets may be at different locations within the redd.

However, our analysis is based on the simplification of an intrinsically 3D bedform to a 2D one. This simplification may lead to some errors in our predictions. Nonetheless, the potential errors can be somewhat assessed based on the study of Chen et al. (2015), in which they evaluated hyporheic fluxes driven by 3D dunes as opposed to 2D ones. Since 3D bedforms generate higher fluxes due to increased drag and exhibit a slightly larger hyporheic zone volume, our analyses could be conservative, because they may predict lower hyporheic

fluxes than those generated by a 3D redd. Further research is necessary to constrain the 3D effects more precisely, as they are also influenced by surface flow hydraulics.

The characteristics of redds, such as aspect ratio, hydraulic conductivity, and surface roughness, could be time dependent. Changes in sediment inputs and in surface hydraulics may lead to variations in these characteristics (Gottesfeld et al., 2004; Hassan et al., 2008; Maturana et al., 2013; Soulsby, Malcolm, et al., 2001b; Zimmermann & Lapointe, 2005a). High flows may alter redd aspect ratios by displacing grains and flattening redd crests, while sediment inputs may deposit in the pit (Gottesfeld et al., 2004; Hassan et al., 2015; Maturana et al., 2013). Fine sediment inputs can lead to the deposition both over and within sediment grains. This deposition results in a dual effect, reducing the redd hydraulic conductivity and smoothening the redd surface roughness as voids among particles are filled (Soulsby, Malcolm, et al., 2001a; Soulsby, Youngson, et al., 2001; Zimmermann & Lapointe, 2005a). Similarly, the opposite trend of surface coarsening could be influenced by local flow hydraulics, as well as flow and sediment regimes (Gottesfeld et al., 2004; Hassan et al., 2008). However, the importance of these processes depends on the local systems (Hassan et al., 2015). For instance, in reaches downstream of lakes or reservoirs, there is typically low sediment input from upstream flows as well as low flow variability. These flows might have magnitudes below the grain mobility, such that redds in such areas may maintain their characteristics during the entire incubation period. In contrast, streams with high discharge variability and high sediment inputs, especially fine sediment, e.g., sand, might cause noticeable changes in redd characteristics during embryo development. It is important to note that our analysis does not account for these transitional effects. Nevertheless, our results can still be used to estimate flux changes using selected values of redd hydraulic conductivity,

surface roughness, and aspect ratio that describe their evolution throughout embryo development. For instance, redd hydraulic conductivity may decrease from the time of spawning to hatching and this variation can be simulated in our model by changing the redd hydraulic conductivity. Thus, the differences in hydraulic conductivities between the redd and egg pocket might diminish with time. Similarly, streambed roughness could also become smoother over time. Therefore, these quantities may have less influence during the later stages of egg development, when compared to the impact of egg pocket location on altering hyporheic flux.

Our study mainly focused on lowland streams characterized by gentle slopes, which induce underflow ambient groundwater. However, we assumed neutral basal (vertical) ambient groundwater. Tonina and Buffington (2009a) showed that pool-riffle induced hyporheic flows have a limited impact on redd-induced hyporheic flows due to the hierarchical nature of hyporheic flows (Tonina & Buffington, 2009c). However, large scale groundwater-stream water connectivity may result in energy head differences large enough to generate upwelling groundwater fluxes. These fluxes could potentially constrain the redd-induced hyporheic flow (e.g., Fox et al., 2016). This effect remains unexplored and could be time-dependent, contingent on factors such as water table dynamics and differences in water surface elevations.

Chapter 3: Evaluation of RANS Turbulence Models in Open Channel Flow over Salmon Redds

3.1 Introduction

Understanding hydrodynamics, particularly over complex geometrical formations like salmonid redds, is essential in riverine ecosystem studies to comprehend salmon spawning behaviors, egg incubation conditions, and overall ecosystem function (Benjankar et al., 2016; Tonina & Buffington, 2009c, 2009a; Tonina & Jorde, 2013). Salmon redds, the nests created by salmon in the riverbed for spawning, interact with river water flow, affecting the survival of salmon eggs and larvae (Coble, 1961; Martin et al., 2020). The interaction between the redd and the riverine hydraulics results in oxygen-rich surface water downwelling into the redd's pit and upwelling just downstream of the redd's crest, forming a process of water exchange known as hyporheic exchange (Tonina & Buffington, 2009b, 2009c). This water exchange is vital for oxygenating the eggs, transporting nutrients, removing metabolic waste, and sustaining the habitat for salmonid eggs development (Buxton, Buffington, Tonina, et al., 2015b; Chapman, 1988; Tonina & Buffington, 2009a). Numerical models (Bhattarai et al., 2023a, 2023b; Cardenas et al., 2016; Tonina & Buffington, 2009d) and with experimental set-ups (P. Carling et al., 1999; P. A. Carling et al., 2006; A. C. Cooper, 1965) have been a valuable tool to investigate these complex fluid dynamics. Given the nature of turbulent flow around salmon redds, turbulence models need to capture the effects of flow characteristics accurately. Among the various numerical models, Reynolds-Averaged Navier-Stokes (RANS) models have been widely used due to their relative computational efficiency and acceptable levels of accuracy in predicting complex flow behavior in natural water bodies

(Wilcox, 1998). Realizable k–ε, standard k–ω, and shear-stress transport (SST) k–ω models have shown promising results in aquatic environments with turbulent flows (Bhattarai et al., 2023a; Cardenas et al., 2016; Menter, 1994; Tonina & Buffington, 2009d; Wilcox, 2008). However, the prediction of flow characteristics in open channel flows, such as streams and rivers, which are characterized by their inherent turbulent nature, several flow reversals, and the presence of a free surface, is highly complex and poses a significant challenge for simulation (Rahimzadeh et al., 2012).

Recent advances in computational fluid dynamics (CFD) have provided an invaluable tool to assess and quantify these flow dynamics with a considerable degree of accuracy. However, the performance of these models can vary significantly based on the specific application, requiring their careful evaluation for each study (Heyrani et al., 2021; Martins Segunda et al., 2018; Simsek et al., 2016; Wang et al., 2022; Yu et al., 2022). Therefore, no single turbulence model is universally accepted as being superior for all classes of problems. The choice of turbulence model depends on considerations such as the physics of the flow, the established practice for a specific class of problem, the level of accuracy required, the available computational resources, the information detailing the boundary conditions, e.g., streambed, and the amount of time available for the simulation. To make the most appropriate choice of model for our application, we need to understand the capabilities and limitations of the various options ("ANSYS Fluent User's Guide," 2019).

The realizable k-ε model enhances the performance of the standard k-ε model by addressing the limitations associated with the isotropy of turbulence (Shih et al., 1995). It introduces flexibility in predicting the spreading rate of both free and wall-bounded shear flows (Patankar, 1980), making it suitable for complex flow simulations such as over salmon redds.

The realizable k-ε model is often used in free-surface flow simulations (Xing et al., 2020),

however it needs additional wall treatment for accurately predicting near-wall flows (*ANSYS*

Fluent Theory Guide, 2019). On the other hand, k-ω turbulence models, being wall-resolved,

can predict turbulence near solid boundaries without additional wall treatments. ω-based

turbulence models use an Automatic Wall Treatment (AWT), recommending a highly refined

near-wall mesh to resolve the viscous sublayer for optimal results (Martins Segunda et al.,

2018). The standard k-ω model, with its robustness and accuracy in the near-wall region, has

been extensively used in boundary layer flow computations (Wilcox, 1998). However, its

performance under adverse pressure gradients, a condition often present in salmon redd

environments, and for free stream modeling has been questioned (*ANSYS Fluent Theory*

Guide, 2019; Menter, 1994). The SST k-ω model is particularly suitable for flows with

adverse pressure gradients and separation (Yorke & Coleman, 2004; J. yin Zhou et al., 2017).

It combines the features of the standard k-ω model in the inner region of the boundary layer

and the k-ε model in the outer region, providing accurate predictions across a wider range of

flow regimes (Menter, 1994).

Despite the popularity of RANS models, their comparative performance in simulating flow

over salmon redds remains unexplored and represents a gap in the literature. The accurate

simulation of such flow conditions can provide insights into important ecological processes

(Tonina & Jorde, 2013) such as egg incubation (Martin et al., 2020), intra-gravel flow

(Cardenas et al., 2016), and fine sediment infiltration (S. Greig et al., 2007; S. M. Greig et

al., 2005). Our research addresses this gap by evaluating and contrasting the predictive

capabilities of the SST k–ω, standard k–ω, and realizable k–ε models in this unique

ecological scenario, along with wall treatments for the realizable k–ε model: standard wall

function, scalable wall function, enhanced wall treatment, and standard wall function with the near wall mesh resolving viscous sublayer in predicting the flow behavior over a salmon redd. For easy convention, these wall treatments are indicated hereafter as follows: realizable k–ε model with standard wall function and the first grid point within the log layer as RKE-SW-LL, standard wall function with near-wall mesh resolving viscous sublayer as RKE-SW-VS, scalable wall function as RKE-ScW, and enhanced wall treatment as RKE-EW. We implement a two-dimensional (2D) numerical modeling approach and employ the VOF method to determine the free surface in each case. We carried out a series of simulations and compared the numerical results against experimental data collected with stereo particle image velocimetry (SPIV) in a controlled flume experiment (Bhattarai et al., 2023a) to assess model accuracy and reliability in predicting the flow hydraulics, e.g., flow and turbulence fields, over a salmon redd. The performance of each RANS model is assessed based on various metrics such as flow speed, turbulent kinetic energy (*TKE*), and water surface elevation.

3.2 Computational Methods

The numerical simulations are performed using the commercial CFD code, ANSYS Fluent (releases 2022 R1, R2, and 2023 R1). The simple scheme is used to solve the pressure-velocity field, and the second-order upwind scheme is used for the spatial discretization of the momentum equation. The second-order implicit scheme is used for transient temporal discretization. The governing equations consist of transport equations for continuity and momentum quantities. The governing equations are solved for a finite-volume formulation of the RANS equations for an incompressible, homogeneous fluid (Janssen et al., 2012; Martins Segunda et al., 2018):

$$\frac{\partial u_i}{\partial x_i} = 0 \tag{8}$$

$$\rho \frac{\partial (u_i u_j)}{\partial x_j} = -\frac{\partial P}{\partial x_i} + \frac{\partial}{\partial x_j}\left[\mu\left(\frac{\partial u_i}{\partial x_j} + \frac{\partial u_j}{\partial x_i}\right)\right] - \rho \frac{\partial \overline{u_i' u_j'}}{\partial x_j} \tag{9}$$

where ρ and μ are fluid density and dynamic viscosity, $u_{i\,or\,j}$ (i, j = 1, 2 where i ≠ j) is the time-averaged velocity, u_i' (i = 1, 2) are the fluctuations in the instantaneous velocity components in $x_{i\,or\,j}$ (i, j = 1, 2 where i ≠ j) directions, the term, $-\overline{\rho u_i' u_j'}$, is the Reynold stresses, and P is time-averaged pressure.

Additional transport equations are also required to be solved for the turbulent flow (*ANSYS Fluent Theory Guide*, 2019). We utilized the three commonly used RANS equations coupled to the two-equation turbulent models, namely, realizable k–ε, standard k–ω and SST k–ω models, to simulate the open channel flow over a salmon redd. A transport equation for the turbulence kinetic energy, k, is solved by all turbulent viscosity models. The realizable k–ε model from Shih et al. (Shih et al., 1995) uses the turbulence eddy dissipation rate (ε) equation derived from the mean-square vorticity fluctuation. The Wilcox (Wilcox, 1998) k–ω model computes the second equation for the specific turbulence dissipation (ω). Menter's (Menter, 1994) SST model solves a blended transport equation of dissipation rate (ε) in the outer part of the boundary layer and specific turbulence dissipation (ω) within the boundary layer.

3.2.1   Realizable k–ε Model

The realizable k-ε model is an improved version of the standard k-ε model, which includes modifications to the turbulent viscosity and dissipation rate equations (*ANSYS Fluent Theory Guide*, 2019). It aims to better capture the physics of turbulent flows and is widely used in

CFD simulations (*ANSYS Fluent Theory Guide*, 2019). It demonstrates enhanced accuracy in forecasting the dissipation rates of flat and round jets, as well as predicting the properties of boundary layers under significant pressure gradients (Bulat & Bulat, 2013). The eddy viscosity (μ_t) and the transport equations for k and ε in the realizable k-ε model are as follows (Shih et al., 1995):

$$\mu_t = \rho C_\mu \frac{k^2}{\varepsilon} \qquad (10)$$

C_μ is computed from,

$$C_\mu = \frac{1}{A_0 + A_s \frac{kU^*}{\epsilon}} \qquad (11)$$

where,

$$U^* \equiv \sqrt{S_{ij}S_{ij} + \tilde{\Omega}_{ij}\tilde{\Omega}_{ij}} \qquad (12)$$

$$\tilde{\Omega}_{ij} = \Omega_{ij} - 2\varepsilon_{ijk}\omega_k \qquad (13)$$

$$\Omega_{ij} = \overline{\Omega_{ij}} - \varepsilon_{ijk}\omega_k \qquad (14)$$

where $\overline{\Omega_{ij}}$ is the mean rate-of-rotation tensor viewed in a moving reference frame with the angular velocity ω_k.

A_0 and A_s are the model constants, A_0=4.04, $A_s=\sqrt{6}cos\varphi$, and

$$\varphi = \frac{1}{3}cos^{-1}(\sqrt{6}W), \ W = \frac{S_{ij}S_{jk}S_{ki}}{\tilde{S}^3}, \ \tilde{S} = \sqrt{S_{ij}S_{ij}}, \ S_{ij} = \frac{1}{2}(\frac{\partial u_j}{\partial x_i} + \frac{\partial u_i}{\partial x_j}) \qquad (15)$$

Transport equations k and ε are computed from,

$$\frac{\partial}{\partial t}(\rho k) + \frac{\partial}{\partial x_j}(\rho k u_j) = \frac{\partial}{\partial x_j}\left[\left(\mu + \frac{\mu_t}{\sigma_k}\right)\frac{\partial k}{\partial x_j}\right] + G_k + G_b - \rho\varepsilon - Y_M + S_k \qquad (16)$$

and

$$\frac{\partial}{\partial t}(\rho\varepsilon) + \frac{\partial}{\partial x_j}(\rho\varepsilon u_j) \qquad (17)$$

$$= \frac{\partial}{\partial x_j}\left[\left(\mu + \frac{\mu_t}{\sigma_\varepsilon}\right)\frac{\partial\varepsilon}{\partial x_j}\right] + \rho C_1 S\varepsilon - \rho C_2 \frac{\varepsilon^2}{k + \sqrt{\nu\varepsilon}} + C_{1\varepsilon}\frac{\varepsilon}{k}C_{3\varepsilon}G_b + S_\varepsilon$$

where,

$$C_1 = max\left[0.43, \frac{\eta}{\eta + 5}\right], \qquad \eta = S\frac{k}{\varepsilon}, \qquad S = \sqrt{2S_{ij}S_{ij}} \qquad (18)$$

G_k represents the generation of turbulence kinetic energy due to the mean velocity gradients. G_b is the generation of turbulence kinetic energy due to buoyancy. Y_M represents the contribution of the fluctuating dilatation in compressible turbulence to the overall dissipation rate. C_2, $C_{1\varepsilon}$, and $C_{3\varepsilon}$ are constants. σ_k and σ_ε are the turbulent Prandtl numbers for k and ε, respectively and ν is the kinematic viscosity. S_k and S_ε are user-defined source terms. Wall treatments in turbulence models are crucial for precise flow predictions near solid boundaries (Launder & Spalding, 1974). They capture important boundary layer characteristics, flow separation, and reattachment zones, integral for understanding flow dynamics over salmon redds and other similar environments like flow over dunes (Bennett & Best, 1995). One common approach is to use wall functions that prescribe the near-wall conditions for the turbulence variables based on the local flow properties and the distance from the wall. Wall functions are efficient and computationally inexpensive, and they can be

used with coarse meshes. This paper focuses on wall treatment options for the realizable k-ε model, known for its effectiveness in high Reynolds number, fully turbulent flows. However, its performance can degrade near walls and in complex flow regions, requiring wall functions or other near-wall treatments for these scenarios (Versteeg & Malalasekera, 1995).

i)   Standard Wall Function (RKE-SW-LL)

The standard wall functions in ANSYS Fluent are based on the work of Launder and Spalding (1974) and uses the logarithmic law for the velocity variation near the wall. The primary use of standard wall functions is to simplify the calculation of near-wall turbulence without requiring a detailed resolution of the boundary layer, which would be computationally expensive (Versteeg & Malalasekera, 1995). It assumes that the near-wall flow can be modeled using semi-empirical relations, which allows the turbulent quantities (velocity and turbulent kinetic energy) to be extrapolated from the turbulent core to the wall, and typically requires a first cell height within the log layer at y^+ value above 30 $\left(y^+ = u_\tau \Delta y / v \right)$, where Δy is the distance of the first grid point from the solid wall, u_* is friction velocity, defined as $u_\tau = \sqrt{\frac{\tau_\omega}{\rho}}$, where τ_ω is wall shear stress and ρ is the fluid density, and v is kinematic viscosity.

ii)   Standard Wall Function with Near-Wall Mesh (RKE-SW-VS)

In ANSYS Fluent, the law-of-the-wall for mean velocity and temperature is based on the wall unit, y^*, rather than y^+. These quantities are approximately equal in equilibrium

turbulent boundary layers (*ANSYS Fluent Theory Guide*, 2019). The log-law is utilized for

the dimensionless near-wall distance, $y^* > 11.225$, whereas the laminar stress-strain

relationship is employed when $y^* < 11.225$ in the wall-adjacent cells. To investigate the

potential benefit of solving momentum equations near the wall for a better flow field, we

positioned the first grid point in the viscous sublayer ($y^+ < 5$), to observe the variations in

flow characteristics near both the wall and the free stream regions, as tested by D. Mohotti

(2019) for the study in predicting wind pressure on buildings. We implemented this change

with the hope of enhancing the capability of this turbulence closure near the wall while

retaining its good performance near the water surface.

iii)   *Scalable Wall Function (RKE-ScW)*

The scalable wall functions are designed to work efficiently across a wide range of y^+

values, thus offering more flexibility in meshing the near-wall regions. For grids that are

coarser than $y^* > 11$, the standard wall functions are identical (*ANSYS Fluent Theory Guide*,

2019). They force the use of the log law in conjunction with the standard wall function

approach. This is achieved by introducing a limiter in the y^* calculations such that $\tilde{y}^* =$

$MAX(y^*, y^*_{limit})$, where y^*_{limit}=11.225. They provide more accurate results in situations

involving strong adverse pressure gradients compared to standard wall functions (Menter &

Egorov, 2010). Despite their improved performance over standard wall functions, scalable

wall functions still represent an approximation to the near-wall turbulence and may introduce

some errors.

iv)   *Enhanced Wall Treatment (RKE-EW)*

ANSYS Fluent simulations use Enhanced Wall Treatment for the ε based models like realizable *k-ε*. This is a near-wall modeling method which combines a two-layer model that subdivides the computational domain into two regions: a viscosity-affected region and a fully turbulent region. Additional details of the turbulence models are in (*ANSYS Fluent Theory Guide*, 2019; Menter & Egorov, 2010). The enhanced wall treatment is used when a more accurate prediction of the near-wall flow field is needed, especially in cases with significant impact from the boundary layer, such as flow separation or high skin-friction drag. However, they require a high-quality mesh with a finer near-wall resolution, which could lead to increased computational cost.

3.2.2   Standard *k–ω* Model

The standard *k–ω* model in ANSYS Fluent is based on the Wilcox (1998) model, which incorporates modifications for low-Reynolds number effects, compressibility, and shear flow spreading. One of the weak points of the Wilcox model is the sensitivity of the solutions to values for *k* and outside the shear layer (freestream sensitivity) (*ANSYS Fluent Theory Guide*, 2019). While the new formulation implemented in ANSYS Fluent has reduced this dependency, it can still have a significant effect on the solution, especially for free shear flows (Menter, 2009). The turbulent viscosity (μ_t) and the two transport equations (turbulent kinetic energy (*k*) and specific dissipation rate of turbulence (ω)) of the standard *k–ω* model are as follows (Wilcox, 1998).

$$\mu_t = \alpha^* \frac{\rho k}{\omega} \tag{19}$$

$$\frac{\partial}{\partial t}(\rho k) + \frac{\partial}{\partial x_i}(\rho k u_i) = \frac{\partial}{\partial x_j}\left((\mu + \frac{\mu_t}{\sigma_k})\frac{\partial k}{\partial x_j}\right) + G_k - Y_k + S_k \tag{20}$$

$$\frac{\partial}{\partial t}(\rho \omega) + \frac{\partial}{\partial x_i}(\rho \omega u_i) = \frac{\partial}{\partial x_j}\left((\mu + \frac{\mu_t}{\sigma_\omega})\frac{\partial \omega}{\partial x_j}\right) + G_\omega - Y_\omega + S_\omega \tag{21}$$

where the coefficient α^* damps the turbulent viscosity, μ_t, causing a low-Reynolds-number correction. G_k represents the generation of turbulence kinetic energy due to mean velocity gradients. G_ω represents the generation of ω. Y_k and Y_ω represent the dissipation of k and ω due to turbulence. S_k and S_ω are user-defined source terms.

The main advantage of this model is its good performance for near-wall turbulence, free shear layers, and in regions affected by strong adverse pressure gradients (Wilcox, 1998). However, the standard k-ω model has shown some deficiencies for fully developed free shear flows and is also very sensitive to the inlet boundary conditions of the ω equation (Wilcox, 1998). It's important to note that the standard k-ω model is known to have limitations in modeling complex flows, and other turbulence models such as the k–ε and SST k–ω models may be more appropriate in those cases.

3.2.3   SST k–ω Model

The SST k–ω turbulence model is a two-equation model that blends the k–ω model in the near-wall region and the k–ε model in the outer region and in the free stream (Versteeg & Malalasekera, 1995; Wilcox, 1998). The SST k-ω model, incorporating the precise Wilcox (Wilcox, 1998) k-ω model for near-wall regions and the stable k-ε model for far-field regions through specific blending functions, was further enhanced by Menter's (Menter, 1994) proposal to redefine the eddy viscosity, resolving the issue of excessive eddy viscosity prediction. So, while the standard k-ω model and the SST k-ω model both contain two

transport equations (one for k and one for ω), the equations are different due to the blending of the k-ε model in the SST version. Specifically, the SST k-ω model modifies the production terms in the k and ω equations and includes a cross-diffusion term in the ω equation.

$$\mu_t = \frac{\rho k}{\omega} \frac{1}{max\left[\frac{1}{\alpha^*} \frac{\sqrt{2\Omega_{ij}\Omega_{ij}}F_2}{\alpha_1\omega}\right]} \tag{22}$$

$$\frac{\partial}{\partial t}(\rho k) + \frac{\partial}{\partial x_i}(\rho k u_i) = \frac{\partial}{\partial x_j}\left((\mu + \frac{\mu_t}{\sigma_k})\frac{\partial k}{\partial x_j}\right) + G_k - Y_k + S_k \tag{23}$$

$$\frac{\partial}{\partial t}(\rho \omega) + \frac{\partial}{\partial x_i}(\rho \omega u_i) = \frac{\partial}{\partial x_j}\left((\mu + \frac{\mu_t}{\sigma_\omega})\frac{\partial \omega}{\partial x_j}\right) + G_\omega - Y_\omega + D_\omega + S_\omega \tag{24}$$

where

$$\sigma_k = \frac{1}{F_1/\sigma_{k,1} + (1 - F_1)/\sigma_{k,2}} \tag{25}$$

$$\sigma_\omega = \frac{1}{F_1/\sigma_{\omega,1} + (1 - F_1)/\sigma_{\omega,2}} \tag{26}$$

Model constants are $\sigma_{k,1} = 1.176$, $\sigma_{\omega,1} = 2.0$, $\sigma_{k,2} = 1.0$, and $\sigma_{\omega,2} = 1.168$

μ_t is turbulent viscosity and σ_k and σ_ω are the turbulent Prandtl numbers. G_k is the generation of turbulence kinetic energy due to mean velocity gradients, G_ω is the generation of ω. Y_k and Y_ω are the dissipation of k and ω due to turbulence. D_ω is the cross-diffusion term. S_k and S_ω are user defined source terms. F_1 and F_2 are the blending functions.

3.2.4 Free Surface Modeling

We treated the system as a two-phase (air and water) problem and tracked the water surface

elevation at the air-water interface using the volume of fluid (VOF) approach (Hirt &

Nichols, 1981). The water surface profile was extracted at locations where the volume

fraction is 0.5, with the values of 1 or 0 representing only water or air, respectively. VOF

method has become the preferred method in modeling due to its superior interface capturing

ability compared to other methods (Kocaer & Yarar, 2020). The tracking of the interface

between the different phases is achieved by solving a continuity equation that describes the

proportion of volume occupied by one or more of the phases. Specifically, for the qth phase,

the equation can be expressed as follows:

$$\frac{\partial}{\partial t}\left(\alpha_q \rho_q\right) + \nabla \cdot \left(\alpha_q \rho_q \vec{v}_q\right) = \sum_{p=1}^{n}\left(\dot{m}_{pq} - \dot{m}_{qp}\right) \tag{27}$$

where $\dot{m}_{pq}$ is the mass transfer from phase p to phase q and $\dot{m}_{qp}$ is the mass transfer from

phase q to phase p. ρ_q is the density and $\vec{v}_q$ is the velocity vector of the qth phase. If the qth

fluid's volume fraction in the cell is denoted as α_q, then the following three conditions are

possible:

• $\alpha_q = 0$: The cell is empty of the qth fluid.

• $\alpha_q = 1$: The cell is full of the qth fluid.

• $0 < \alpha_q < 1$: The cell contains the interface between the qth fluid and one or more other

fluids.

3.2.5   Geometry, Boundary Conditions and Mesh

The water-sediment interface was specified as a smooth, no-slip impermeable boundary

(Figure 28), which is a typical condition for this problem (Cardenas & Wilson, 2007c; Chen

et al., 2015) because momentum and mass exchanges with porous sediment are small and

have negligible influence on surface hydraulics (Janssen et al., 2012). Water boundaries were

defined as velocity inlet and velocity outlet conditions for the upstream and downstream

locations, respectively. Measured flow fields at upstream (X = -1.14 m) and downstream (X

= 1.42 m) locations were used to establish boundary conditions for the streamwise (V_x) and

vertical (V_y) velocities (V_y was less than 2% of V_x) as well as the *TKE* profiles for the CFD

models (Bhattarai et al., 2023a). The starting of the redd is at X = 0. Air boundaries were

specified as pressure outlets. We ran all simulations for about four flow cycles throughout the

full domain to ensure that the flows were in equilibrium with the specified boundary

conditions.
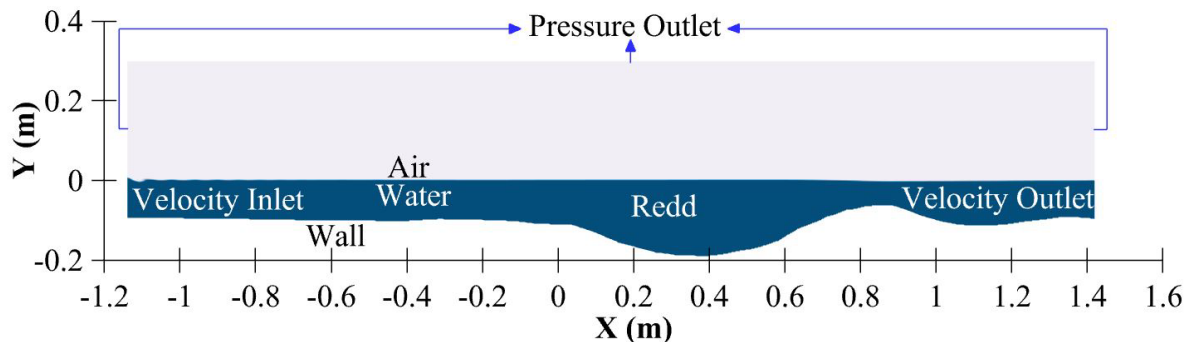
Figure 28: Illustration of the flow domain with boundary conditions.

The computational mesh was constructed using Pointwise (release V18.0 R4) (Figure 29).

There are approximately 0.2 million quadrilateral cells with a mean cell size of about 3 mm

in the horizontal direction. We employed a highly refined 0.8 mm cell size in the vertical

direction at the air-water interface to accurately track water surface elevation. For all models

except RKE-SW-LL, we used a very small vertical cell size of about 0.375 mm close to the

bottom boundary i.e., the first grid point off the wall for these models was within the viscous

sublayer where $y^+ < 5$. For RKE-SW-LL, the first grid point was positioned in the log layer

with an average $y^+ = 33.4$ and a near-wall grid spacing of $\Delta y = 20.6$ mm.
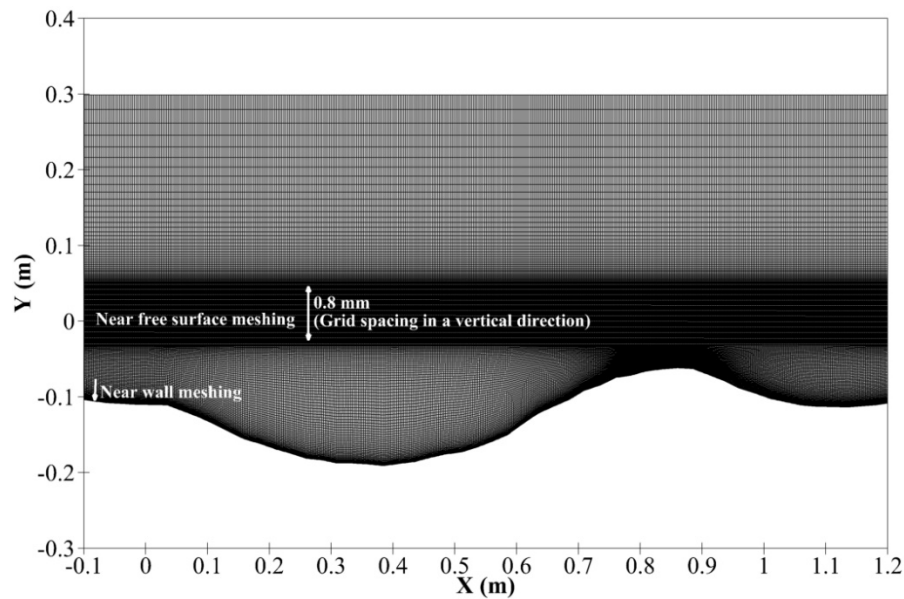
Figure 29: Zoomed-in section near the redd showing the mesh.

This study utilizes the supplementary experimental data from an experiment conducted at

The Center for Ecohydraulics Research to study the hydrodynamics of a model salmon redd

(Bhattarai et al., 2022; Moreto et al., 2022). The experiment involved an upstream flow depth

of 0.1 m and an upstream streamwise velocity of 0.2 m/s in a 7 m long, 0.5 m wide, and 0.7

m deep recirculating flume. We reference the velocity field at the downstream end of the

redd crest and the streamwise velocity profile from Bhattarai et al. (2023a). In addition, this

study also compares *TKE* and free surface profiles to validate the simulation results. Free

surface is expressed in terms of relative water surface elevation (WSE_R). WSE_R is defined as the difference between the local free surface elevation and the undisturbed free surface elevation based on water depth at the inlet. We defined the relative total head, $H_R = H - (Y_0 + z)$, where H is the total head, Y_0 is the undisturbed hydraulic depth away from the redd based on the inlet water depth and z is the difference between the local streambed and the datum that are sloped at the same angle. The experimental setup and the overall procedure are further discussed in Bhattarai et al. (2023a). Simulation performance was also quantified using the Nash Sutcliffe Coefficients (NSC) as an indicator of model quality. The NSC values are categorized as follows: very good (NSC > 0.75), good (0.65 < NSC ≤ 0.75), satisfactory (0.5 < NSC ≤ 0.65), and unsatisfactory (NSC ≤ 0.5) (Moriasi et al., 2007).

3.3 Solution Verification and Validation (V&V)

To ensure that the results are independent of the time-step size and mesh resolutions, we conducted a solution verification using three systematically refined meshes (fine, medium, and coarse). In this study, we performed the solution verification for Vx using the SST k-ω model. The V&V for the RKE-SW-VS model was performed in our earlier study (Bhattarai et al., 2023a). We did not conduct solution verification for all the models, as some of them utilize wall functions for which solution verification is not applicable due to the requirement for systematically refined meshes. The overall grid size, the total number of grid points, and time step size used for solution verification are given in Table 5. We used a grid refinement ratio, $r_G = \dfrac{\Delta x_2}{\Delta x_1} = \dfrac{\Delta x_3}{\Delta x_2} = 1.414$, where Δx is the grid distance between two elements and the subscripts 1, 2, and 3 represent the fine, medium, and coarse meshes, respectively. The overall procedure is described in (Xing et al., 2008; Xing & Stern, 2010, 2011). The

convergence ratio, denoted by R_G, is the ratio of solution differences for medium-fine and coarse-medium solution pairs. L2 norms (square root of the sum of the squares of the differences between the coordinates of the two points) of streamwise velocity profiles are used to calculate $\varepsilon_{G_{21}}$ and $\varepsilon_{G_{32}}$ to define the ratios for R_G and P_G (observed order of accuracy), i.e.,

$$\langle R_G \rangle = \left\| \varepsilon_{G_{21}} \right\|_2 / \left\| \varepsilon_{G_{32}} \right\|_2 \tag{28}$$

$$\text{where } \left\| \varepsilon_{G_{21}} \right\|_2 = \sqrt{\Sigma_{k=1}^N (P_1 - P_2)^2} \tag{29}$$

$$\langle P_G \rangle = \frac{\ln(\left\| \varepsilon_{G_{32}} \right\|_2 / \left\| \varepsilon_{G_{21}} \right\|_2)}{\ln(r_G)} \tag{30}$$

where $\langle \ \rangle$ & and $\| \ \|_2$ denotes a profile-averaged quantity (solution change ratio based on L2 norms) and L2 norm, respectively (Wilson et al., 2001). N is the number of points along a single velocity profile and P_1 and P_2 are the point solutions (V_x) for meshes 1 and 2, respectively.

Table 5: Solution verification (SST k-ω model).

Grids	Grid Dimensions	Total Number of Points	Time step size (s)
1	869 × 220	191,180	0.002
2	615 × 155	95,325	0.002828
3	430 × 108	46,440	0.004

U_G is the numerical uncertainty estimate and $|E|$ is the absolute relative error between the fine mesh and the experimental data, representing a measure of bias error between the numerical and experimental results ($|E| = |S - D|$), where S is the fine mesh streamwise average velocity, and D is the experimental streamwise average velocity. U_V is the validation uncertainty ($U_V = \sqrt{U_G^2 + U_D^2}$), where U_D is the experimental uncertainty, representing an

average uncertainty of the numerical and experimental results. Validation is achieved when

$|E| < U_V$.

For the solution verification and validation study, we used three locations (X = 1 m, 1.05 m, and 1.15 m). The grid triplet showed monotonic convergence ($0 < R_G < 1$) at all three horizontal locations with small grid uncertainty values ranging from 30.37 %D to 87.22 %D. All four locations showed that the model was validated ($|E| < U_V$) (Table 6).

Table 6: Verification & Validation study for the longitudinal component of the velocity. Percentages are calculated using experimental data (%D).

x-location (m)	R_G	P_G	U_G	U_G(%D)	U_D(%D)	$|E|$(%D)	U_V(%D)
1.0	0.40	2.56	0.19	87.22	0.33	0.49	87.22
1.05	0.56	1.65	0.09	45.51	0.41	1.8	45.51
1.15	0.47	2.15	0.056	30.37	0.55	1.99	30.38

3.4 Results

3.4.1 Velocity Field Comparisons

We compared the streamwise velocity contours and flow streamlines predicted by different RANS models against the experimental flow field in the area denoted by the red box, representing the region extending from the crest of the redd to its downstream end (Figure 30a). RKE-SW-VS showed the closest resemblance to experimental observation in depicting the near-wall separation vortex size and the location of the reattachment zone (Figure 30b). The SST k–ω model slightly overpredicted the size of the separation vortex, whereas the standard k–ω not only overpredicted the vortex size but also predicted an additional separation zone further downstream. The realizable k–ε model, coupled with other near-wall treatments, either underestimated the size of the separation zone or failed to depict it

altogether. Consequently, RKE-SW-VS demonstrated the best performance in predicting near-wall flow separation.
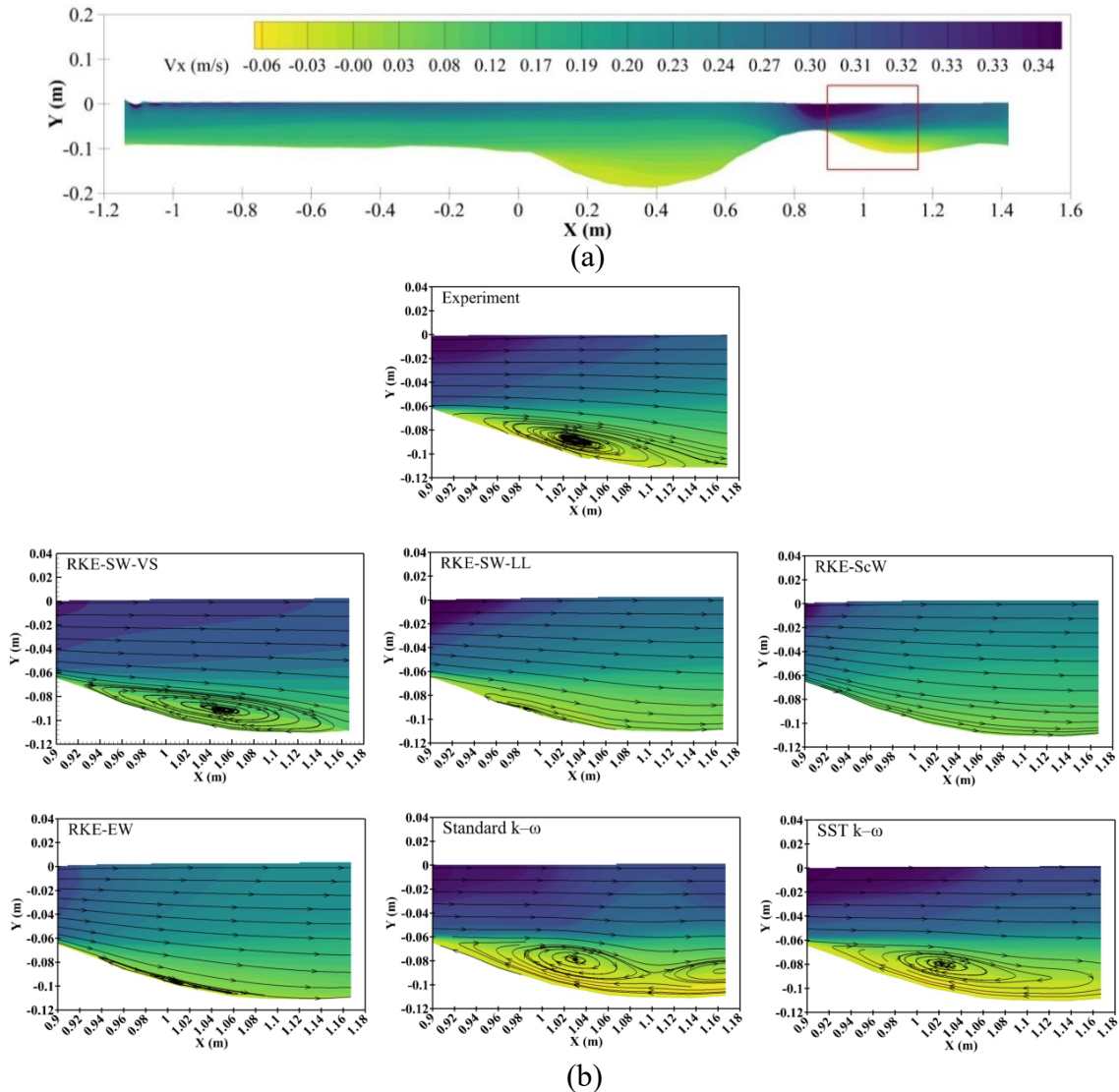
Figure 30: Comparison between CFD and experimental data for streamwise velocity field: (a) across the entire simulation domain, indicating the comparison region with a red square box, and (b) experimental and CFD results within that region. The flow direction is from left to right.

The velocity magnitude contours from different models compared differently with the experimental result (Figure 31). Both RKE-SW-VS and the SST k–ω models accurately simulate the experimental velocity magnitude contours. While the standard k–ω model captured the velocity field effectively very close to the wall, its performance notably

degraded near the free stream. Compared to all other k–ε models, RKE-SW-VS aligns most closely with the experimental observations, both near the wall and in the free stream regions.
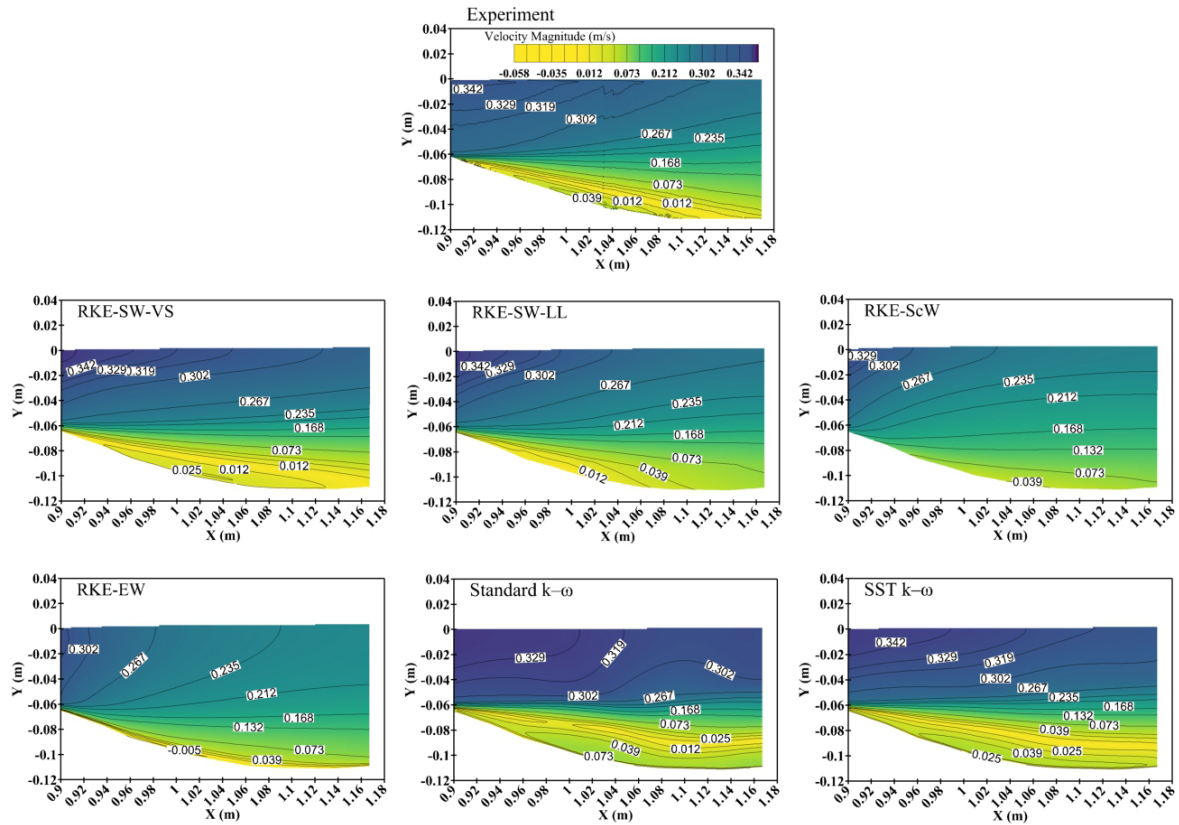
Figure 31: Comparison of the simulated and experimental velocity magnitude contours from different models in the region denoted by the red box in Figure 30a.

We also evaluated streamwise velocity (V_x) profiles downstream of the crest (X = 0.95 m) and further downstream of the end of the redd (X = 1.05 m and X = 1.15 m) for all models, comparing with experimental V_x profiles (Figure 32). Both SST k–ω and standard k–ω models effectively replicated the overall profile trend and accurately captured near wall flow circulations, as indicated by the negative V_x profile, at two of the three investigated X-locations (X = 0.95 m and 1.05 m), marking a potential flow separation zone (Figure 30b). However, both models overpredicted the flow circulation at X = 1.15 m (potential end of the flow separation, Figure 30b). Although RKE-SW-LL also mimicked the profile trend, it did

not accurately represent the flow circulation close to wall. RKE-ScW and RKE-EW models did not predict the V_x profile effectively. RKE-SW-VS performance was superior compared to all other models at all three specified X-locations, both near the wall as well as near the free stream.

SST k–ω, standard k–ω, RKE-SW-VS, and RKE-SW-LL consistently demonstrated good performance with high NSC values. In contrast, the performance of realizable k–ε varied when coupled with other wall treatments. Particularly, RKE-ScW and RKE-EW displayed a degraded performance when compared to experimental data, especially at X = 0.95 m (Table 7). Among all the models, RKE-SW-VS exhibited the best performance at all three X-locations (Figure 32), recording the highest NSC values (Table 7), highlighting its exceptional capability in predicting the velocity profiles.
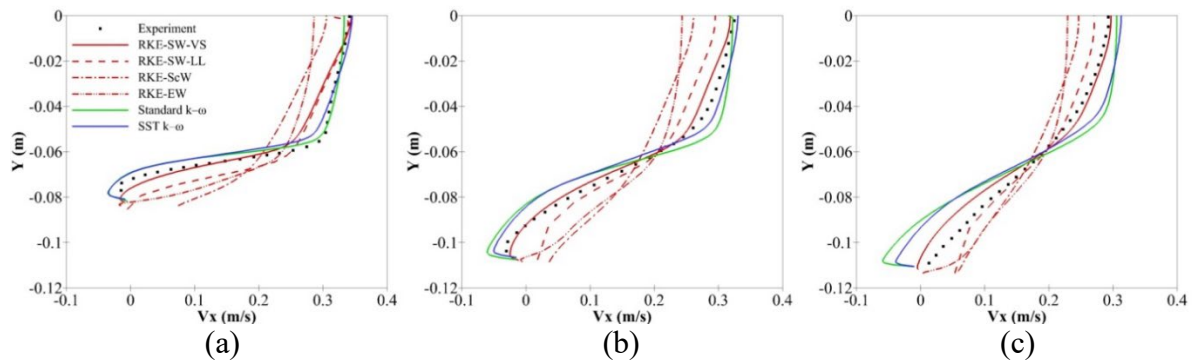
Figure 32: Streamwise velocity profiles at (a) X = 0.95 m (b) X = 1.05 m and (c) X = 1.15 m

Table 7: Evaluation of Streamwise velocity (V_x), Turbulent Kinetic Energy (*TKE*), and Free Surface performance for various RANS models using the Nash Sutcliffe Coefficient (NSC).

RANS Models		Nash Sutcliffe Coefficient (NSC)						Free Surface
		V_x (X-Location, m)			*TKE* (X-Location, m)			
		0.95	1.05	1.15	0.95	1.05	1.15	
SST *k–ω*		0.93	0.96	0.82	0.69	**0.90**	**0.88**	0.65
Standard *k–ω*		0.95	0.94	0.74	0.29	0.73	0.83	0.68
Realizable *k–ε*	RKE-SW-VS	**0.96**	**0.99**	**0.96**	N/A	0.84	0.85	**0.91**
	RKE-SW-LL	0.82	0.94	0.96	N/A	0.62	0.25	0.90
	RKE-ScW	0.53	0.73	0.84	N/A	0.22	N/A	0.63
	RKE-EW	0.62	0.76	0.83	N/A	0.44	0.10	0.50

3.4.2   Turbulent Kinetic Energy (TKE) Comparisons

SST *k–ω*, standard *k–ω* and RKE-SW-VS closely represented the shape of the *TKE* profile across all three X-locations, comparing against the experimental *TKE* profile in the protruding region (maximum *TKE*) (Figure 33). At X = 0.95 m, each model showed the highest deviation in the *TKE* profile, ranging from about 0.0005 to 0.001 (m^2/s^2) above the protrusion. RKE-ScW underpredicted the profile trend at all X-locations. RKE-SW-LL and RKE-EW captured the trend but underestimated the magnitude of the maximum *TKE* value.

Closer *TKE* profile comparisons using NSC values demonstrated varying performance at different X-locations (Table 7), consistent with the visual observations in Figure 33. The realizable *k–ε* model, with all wall treatments, underperformed against the mean observed value at X = 0.95 m (marked as N/A, indicating predictive deficiencies). Notably, both the standard *k–ω* and RKE-SW-VS showed improved performance at the downstream end of the redd at X = 1.05 and 1.15 m. However, the performance of the realizable *k–ε* models, when coupled with other wall treatments, was still not as effective. Compared to all other models,

the SST k–ω model exhibited better performance across all three X-locations, indicating that the SST k–ω model has proven to be the best option in predicting *TKE*.
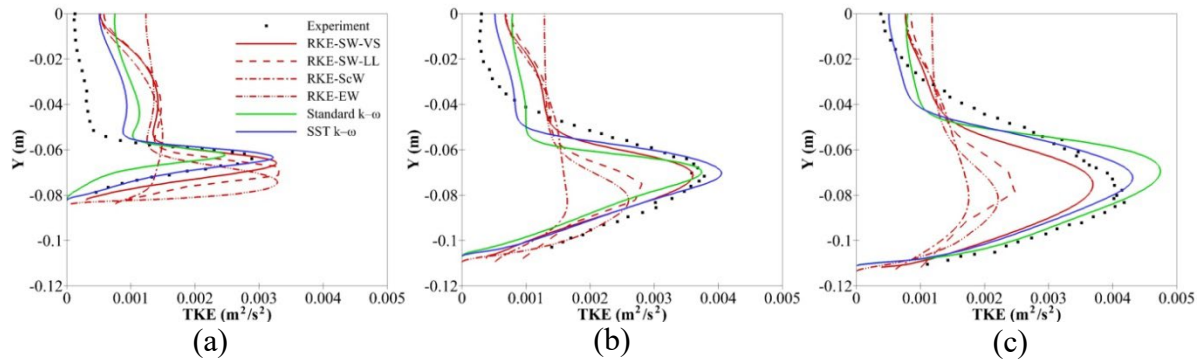
Figure 33: Turbulent Kinetic Energy (*TKE*) profiles at (a) X = 0.95 m (b) X = 1.05 m and (c) X = 1.15 m.

3.4.3   Free Surface Profile Comparisons

All models yielded diverse relative water surface elevation (WSE_R) profile predictions upstream and downstream of the redd crest (Figure 34). Upstream of the redd crest, the RKE-ScW model showed oscillations in the WSE_R profile around the experimental WSE_R profile, while RKE-EW model slightly overpredicted the WSE_R when compared to the experimental data. Both RKE-ScW and RKE-EW overestimated the downstream WSE_R. RKE-SW-VS closely predicted the experimental WSE_R profile, both upstream and downstream of the crest, while RKE-SW-LL also showed nearly identical profile predictions in these regions. Both k–ω models predicted the WSE_R profile upstream of the crest but underestimated it downstream (Figure 34).

The superior performance of the realizable k–ε model coupled with standard wall function, especially RKE-SW-VS, as seen in Figure 34 and confirmed by high NSC values in (Table 7), indicates the realizable k–ε model's effectiveness in representing free surface profiles.
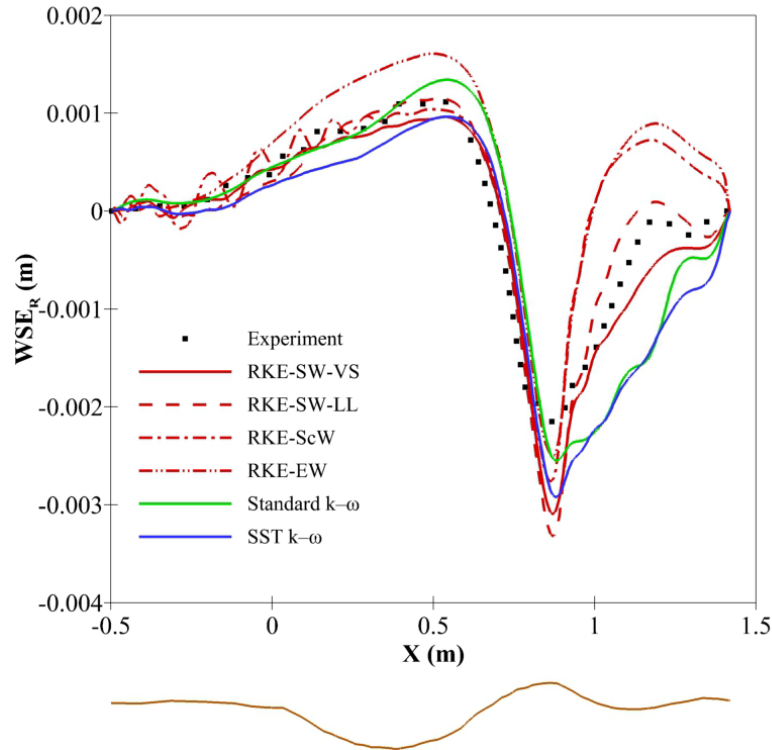
Figure 34: Relative water surface elevation (*WSE_R*) profiles for different RANS models compared with experiment, along with the illustration of the redd profile (redd starting at X = 0) indicating redd location.

3.4.4   Total Head Profile Comparisons

All models predicted similar profile trends for the head, except for RKE-SW-LL. This model diverges significantly, predicting the highest head at the stoss side of the redd but slightly shifted downstream near the redd crest. The SST k–ω, standard k–ω, and RKE-SW-VS, all portrayed similar profiles, with comparable head amplitudes but with slight differences in the minimum and maximum head values (Figure 35). This indicates that the realizable k–ε model employing a wall function with a coarse mesh near the wall boundary may not accurately capture the head variation in the viscous sublayer. In contrast, using fine mesh resolution near the wall (low y+ treatment) can better resolve these head variations.
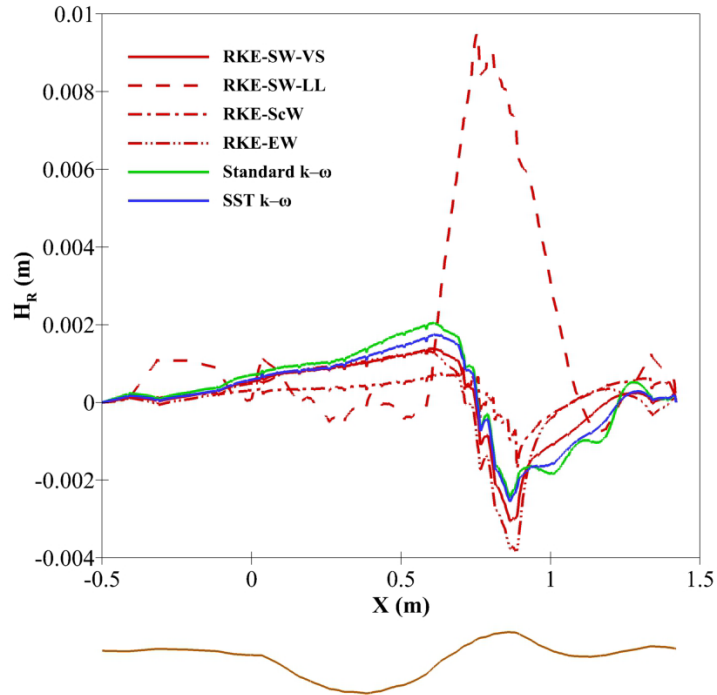
Figure 35: Relative total head (H_R) profiles for different RANS models, along with the illustration of the redd profile (redd starting at X = 0) indicating redd location

3.4.5 Flow Field Comparison over Salmonid Redds

In the redd's pit region (Figure 36), substantial flow circulation was predicted by both k–ω models as well as RKE-SW-VS. These models yielded fairly similar sizes for the separation vortex. RKE-ScW and RKE-EW, on the other hand, predicted a smaller separation zone, and RKE-SW-LL failed to capture this separation entirely, potentially due to the insufficient grid points near the wall, thus limiting its ability to accurately model near-wall characteristics.
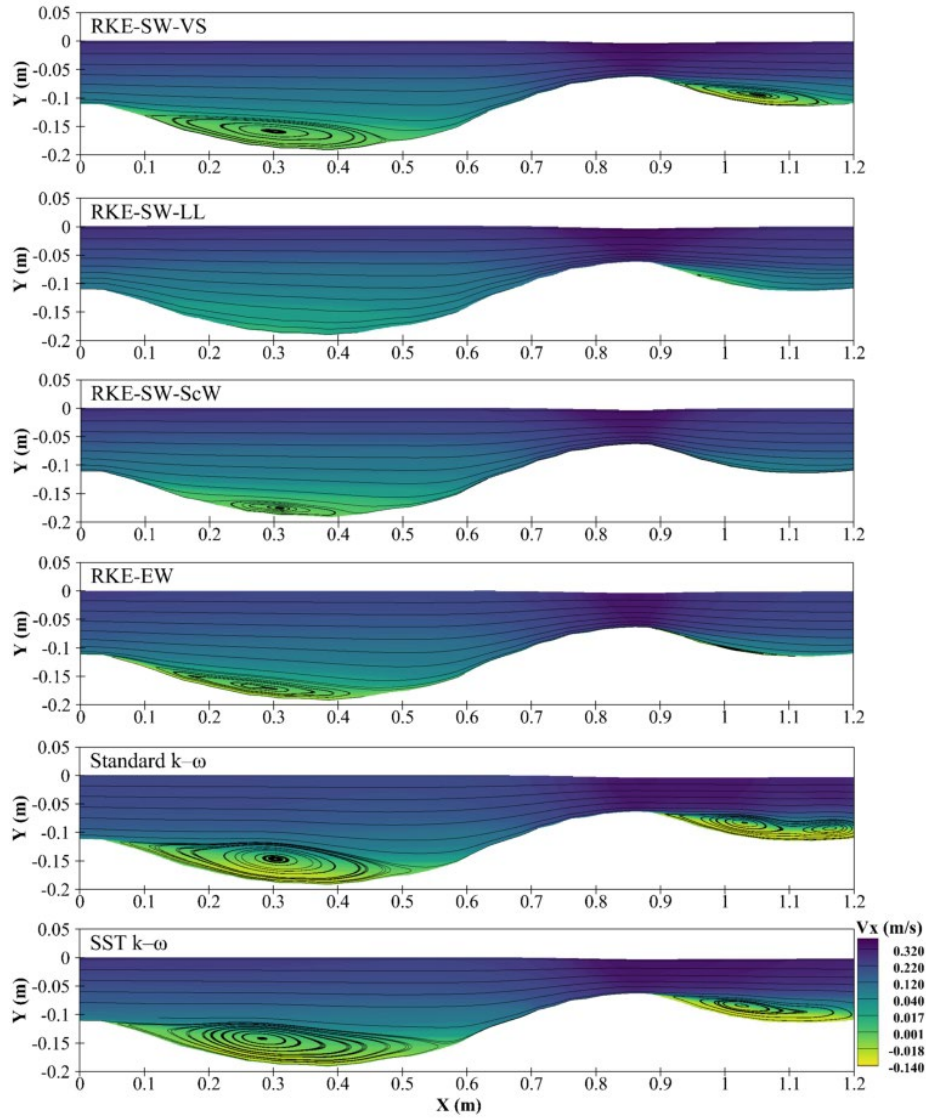
Figure 36: Streamwise velocity contours and flow streamlines for different RANS models across the redd. Flow is from left to right.

3.5 Discussion

We assessed the performance of three RANS turbulence models - realizable k–ε, standard k–ω, and SST k–ω - in capturing the flow dynamics over a salmon redd, a highly complex and ecologically significant flow scenario. An additional aspect considered was the influence of wall treatments for the realizable k–ε model. This analysis highlighted the importance of

selecting the appropriate wall treatment based on the specific requirements of the study in terms of accuracy, complexity, and computational cost.

The flow structure around salmon redds, particularly the near-bed pressure distributions and near-wall flow separations, is critical for understanding riverine ecosystems and salmon reproduction (Cardenas et al., 2016; Tonina & Buffington, 2009c). The RKE-SW-VS model exhibited significant accuracy in predicting near-wall phenomena, such as separation vortices and reattachment zones, as well as characteristics of the free surface. Additionally, the RKE-SW-VS emerged to be the most accurate in predicting streamwise velocity and free surface profiles. This result is supported by visual inspections as well as NSC values, further affirming its suitability for such predictions. The limitation of the realizable k-ε model applied to log-layer resolved grids (RKE-SW-LL) in predicting separation zone and the total head profile suggests that without a fine mesh near the wall, it lacks the sensitivity required to capture complex flow dynamics near the boundary layer. Consequently, it may not effectively capture variation in head within the viscous sublayer. The standard k–ω and SST k–ω models predicted near-wall flow circulations, aligning well with the experimental flow field, particularly in velocity magnitude contour visualization (Figure 31). However, the SST k–ω model slightly overpredicted the size of the separation vortex, while the standard k–ω model not only overestimated the vortex size but also incorrectly introduced an additional downstream separation zone. The standard k–ω model, while accurately predicting flow near the wall boundary, failed to predict the free stream flow with a similar accuracy (Figure 31), confirming the known limitations of this model in such conditions (Wilcox, 1998). The SST k–ω model was the most effective in predicting turbulent kinetic energy (*TKE*), a crucial factor for water mixing processes and enhancing the water transport into the hyporheic zone

(Roche et al., 2018). However, overestimation of the size of the separation vortex can lead to inaccuracies in the assessment of salmon habitat suitability and could also lead to imprecise interpretations of the flow behavior around redds. Different variations of the realizable k–ε model with alternative wall treatments, such as RKE-ScW and RKE-EW, exhibited significantly degraded performance, particularly in capturing streamwise velocity profiles at critical locations where potential flow separation occurs. This suggests a potential limitation in near-wall treatments under complex flow conditions, including strong pressure gradients and flow separation. Such deficiencies suggest their limited applicability in accurately modeling flow dynamics around redds. Both RKE-SW-LL and RKE-SW-VS showed impressive performance for predicting the free surface profile, with very good NSC values of 0.9.

The results indicate that while some turbulence models exhibit strengths in certain critical areas, no single model consistently provides the best results across all flow characteristics, which is similar to the findings from the CFD workshop on ship hydrodynamics (Bhushan et al., 2013). This suggests the importance of a customized model selection process, considering the specific flow features and ecological interactions under investigation, as well as the availability of the computational resources and the associated costs. For instance, the RKE-SW-LL model may be chosen for predictions in the free surface region where it is computationally less demanding and provides accurate results; however, its coarse mesh may not capture near-wall flow fields with sufficient precision. On the other hand, the RKE-SW-VS model predicted all characteristics with high accuracy except for *TKE*, yet the SST k–ω model was marginally better at predicting *TKE*. Therefore, it is important that model development continues to be refined through such comparative analyses, particularly to

improve simulations of flow over complex topographies, such as those found over salmon

redds. These advancements are crucial for the effective conservation and management of

salmonid species and their habitats.

Chapter 4: Conclusion

This comprehensive research integrated various hydraulic modeling approaches to explore the hyporheic exchange in salmonid redds. This study incorporates extensive analyses of redd-stream flow interactions, encompassing various surface flow hydraulics, redd sizes, streambed roughness, egg pocket permeability, and location on hyporheic fluxes. We also conducted an evaluation of different turbulence models for accurately simulating complex open channel flows.

Our simulations have quantified the systematic change in hyporheic exchange induced by redd-stream flow interactions across a broad range of surface flow hydraulics and redd sizes. Salmonids construct redds in streambed gravel, shaping them as dunes to induce the flow of oxygen-rich surface water toward the egg pocket. We observed that the total head gradient across the redd increases with the redd aspect ratio and river discharge. Regardless of surface flow hydraulics, the overall shape of the total head distribution over the redd remains typically consistent, characterized by the two low heads at the beginning and crest of the redd and a high head between the pit and the tailspill. Additionally, a secondary high total head is observed on the streambed downstream of the redd, although decreasing in intensity for smaller redd aspect ratios. These findings contribute to our understanding of how salmonids, through their spawning activities, enhance the environmental conditions of the egg habitat by altering both streambed morphology and sediment permeability. Our dimensional analysis further allows us to develop regression equations that predict the total head drop and mean downwelling hyporheic fluxes based on dimensionless variables like Reynolds number (Re), Froude number (Fr), and redd aspect ratio (A_R). These equations can be instrumental in

studying the hydraulic characteristics of interstitial flows experienced by salmon embryos and in evaluating hyporheic processes induced by dune-like bedforms.

Moreover, our study delves into the interstitial flows towards egg pockets within redds. The egg pockets within the redd can have different locations and higher hydraulic conductivities compared to the overall redd. The interstitial flows toward the egg pocket increase with the egg pocket's distance from the pit, as the downstream egg pockets received progressively higher fluxes compared to the first egg pocket, indicating a lack of hydraulic interference among densely packed egg pockets. The difference in hydraulic conductivity between the egg pocket and the overall redd permeability significantly influences interstitial flow toward the egg pocket. However, this increase in flow is relatively small compared to the uncertainty in egg pocket locations. For instance, an eight-fold, i.e., 800% increase in egg pocket permeability resulted in only a 71% increase in interstitial flow. We also explored the influence of streambed roughness on near-bed pressure gradients and in shaping hyporheic exchanges. Rough streambeds contribute to more complex hyporheic exchanges, with multiple fast and shallow near-surface hyporheic cells superimposed over the large cell generated by the redd's shape. However, the impact of streambed roughness on the flows into egg pocket diminishes with increasing sediment depth, becoming negligible at depths more than twice the median grain size, regardless of the roughness type. Consequently, the interstitial flows near the egg pockets are predominantly controlled by the redd's shape and permeability, with roughness playing a secondary role. Our results support the common simplification of the redds as homogeneous features with a smooth surface. Recognizing the complexities of redd formations, hydraulic conductivities, and roughness leads to a more

comprehensive understanding of the mechanisms driving the transport of oxygen-rich surface water toward the eggs.

Additionally, our evaluation of different RANS turbulence models highlights the importance of selecting appropriate models and wall treatments for simulating complex environmental flows. The realizable k-ε model, especially with a near-wall mesh and standard wall function, demonstrates the best accuracy in predicting velocity fields and flow separations over salmon redds. Meanwhile, the SST k-ω model performs best in predicting *TKE*. This variability among models in accurately predicting specific flow features underlines the necessity of a careful and context-specific choice of turbulence models. It suggests that a combination of different models might be required to fully comprehend the flow physics in such complex scenarios. Future research will focus on extending these models to three-dimensional simulations and integrating more advanced turbulence models like large eddy simulations and detached eddy simulations, coupled with rigorous solution verification and validation (Dutta & Xing, 2018; Xing, 2015).

Literature Cited

Aberle, J., & Nikora, V. (2006). Statistical properties of armored gravel bed surfaces. *Water Resources Research*, *42*(11), 1–11. https://doi.org/10.1029/2005WR004674

Anderson, J. J., Beer, W. N., Israel, J. A., & Greene, S. (2022). Targeting river operations to the critical thermal window of fish incubation: Model and case study on Sacramento River winter-run Chinook salmon. *River Research and Applications*, *38*(5), 895–905. https://doi.org/10.1002/rra.3965

ANSYS Fluent Theory Guide. (2019). http://www.ansys.com

ANSYS Fluent User's Guide. (2019). In *Knowledge Creation Diffusion Utilization*.

Baxter, C. V., & Hauer, F. R. (2000). Geomorphology, hyporheic exchange, and selection of spawning habitat by bull trout (Salvelinus confluentus). *Canadian Journal of Fisheries and Aquatic Sciences*, *57*(7), 1470–1481. https://doi.org/10.1139/f00-056

Benjankar, R., Tonina, D., Marzadri, A., McKean, J. A. J., & Isaak, D. J. (2016). *Effects of habitat quality and ambient hyporheic flows on salmon spawning site selection. 121*(5), 1222–1235. https://doi.org/10.1002/2015JG003079

Bennett, S. J., & Best, J. L. (1995). Mean flow and turbulence structure over fixed, two-dimensional dunes: implications for sediment transport and bedform stability. *Sedimentology*, *42*(3), 491–513. https://doi.org/https://doi.org/10.1111/j.1365-3091.1995.tb00386.x

Bhattarai, B., Hilliard, B., Reeder, W. J., Budwig, R., Martin, B. T., Xing, T., & Tonina, D. (2023a). Effect of Surface Hydraulics and Salmon Redd Size on Redd- Induced Hyporheic Exchange. *Water Resources Research*, *59*(6), 1–24. https://doi.org/10.1029/2022WR033977

Bhattarai, B., Hilliard, B., Reeder, W. J., Budwig, R., Martin, B. T., Xing, T., & Tonina, D. (2023b). The role of riverine bed roughness, egg pocket location, and egg pocket permeability on salmonid redd-induced hyporheic flows. *Water Resources Research*, *59*(11), 1–17. https://doi.org/10.1029/2023WR035548

Bhattarai, B., Tonina, D., Reeder, W. J., Budwig, R., Hilliard, B., Martin, B., & Xing, T. (2022). *Salmon redd-induced hyporheic flow, HydroShare*. https://doi.org/https://www.hydroshare.org/resource/6deaf594de954b95b81bd117bd919960/

Bhushan, S., Xing, T., Visonneau, M., Wackers, J., Deng, G., Stern, F., & Larsson, L. (2013). *Post Workshop Computations and Analysis for KVLCC2 and 5415* (L. Larsson, M. Visonneau, & F. Stern (Eds.)). Springer.

Bjornn, T. C., & Reiser, D. W. (1991). Habitat requirements of salmonids in streams. In W. R. Meehan (Ed.), *Influence of forest and rangeland management on salmonid fishes and their habitats* (pp. 83–138). Am. Fish. Soc. Spec. Publ. 19. Bethesda, Md.

Boano, F., Harvey, J. W., Marion, A., Packman, A. I., Revelli, R., Ridolfi, L., & Wörman, A. (2014). Hyporheic flow and transport processes: Mechanisms, models, and biogeochemical implications. *Reviews of Geophysics*, *52*(4), 603–679. https://doi.org/10.1002/2012RG000417

Boyd, J. W., Oldenburg, E. W., & Mcmichael, G. A. (2010). Color photographic index of fall chinook salmon embryonic development and accumulated thermal units. *PLoS ONE*, *5*(7). https://doi.org/10.1371/journal.pone.0011877

Bray, E. N., & Dunne, T. (2017). Subsurface flow in lowland river gravel bars. *Water Resources Research*, *53*(9), 7773–7797.

Broecker, T., Elsesser, W., Teuber, K., Özgen, I., Nützmann, G., & Hinkelmann, R. (2018). High-resolution simulation of free-surface flow and tracer retention over streambeds with ripples. *Limnologica*, *68*(September 2017), 46–58. https://doi.org/10.1016/j.limno.2017.06.005

Broecker, T., Teuber, K., Gollo, V. S., Nützmann, G., Lewandowski, J., & Hinkelmann, R. (2019). Integral flow modelling approach for surface water-groundwater interactions along a rippled streambed. *Water (Switzerland)*, *11*(7). https://doi.org/10.3390/w11071517

Buffington, J. M., & Montgomery, D. R. (1999). Effects of hydraulic roughness on surface textures of gravel-bed rivers. *Water Resources Research*, *35*(11), 3507–3521.

Bulat, M. P., & Bulat, P. V. (2013). *Comparison of Turbulence Models in the Calculation of Supersonic Separated Flows*. *27*(10), 1263–1266. https://doi.org/10.5829/idosi.wasj.2013.27.10.13715

Burner, C. J. (1951). Characteristics of spawning nests of Columbia River salmon. *Fishery Bulletin*, *52*, 97–110.

Buxton, T. H., Buffington, J. M., Tonina, D., Fremier, A. K., & Yager, E. M. (2015a).
Modeling the influence of salmon spawning on hyporheic exchange of marine-derived
nutrients in gravel stream beds. *Canadian Journal of Fisheries and Aquatic Sciences*,
72(8), 1146–1158. https://doi.org/10.1139/cjfas-2014-0413

Buxton, T. H., Buffington, J. M., Tonina, D., Fremier, A. K., & Yager, E. M. (2015b).
Modeling the Influence of Salmon Spawning on Hyporheic Exchange of Marine-
Derived Nutrients in Gravel Streambeds. *Canadian Journal of Fisheries and Aquatic
Sciences*, *72*(8), 1146–1158. https://doi.org/10.1139/cjfas-2014-0413

Buxton, T. H., Buffington, J. M., Yager, E. M., Hassan, M. A., & Fremier, A. K. (2015). The
relative stability of salmon redds and unspawned streambeds. *Water Resources
Research*, *51*(8), 6074–6092. https://doi.org/10.1002/2015WR016908

Cardenas, Ford, A. E. A., Kaufman, M. H., Kessler, A. J., Cook, P. L. M., … M. K.-J. of, &
2016, U. (2016). Hyporheic flow and dissolved oxygen distribution in fish nests: The
effects of open channel velocity, permeability patterns, and groundwater upwelling.
Journal of Geophysical Research: Biogeosciences, *121*(12), 3113–3130.
https://doi.org/10.1002/2016JG003381

Cardenas, M. B., & Wilson, J. L. (2007a). Dunes, turbulent eddies, and interfacial exchange
with permeable sediments. *Water Resources Research*, *43*(8), 1–16.
https://doi.org/10.1029/2006WR005787

Cardenas, M. B., & Wilson, J. L. (2007b). Effects of current-bed form induced fluid flow on
the thermal regime of sediments. *Water Resources Research*, *43*(8), 1–12.
https://doi.org/10.1029/2006WR005343

Cardenas, M. B., & Wilson, J. L. (2007c). Exchange across a sediment-water interface with ambient groundwater discharge. *Journal of Hydrology*, *346*(3–4), 69–80. https://doi.org/10.1016/j.jhydrol.2007.08.019

Cardenas, M. B., & Wilson, J. L. (2007d). Hydrodynamics of coupled flow above and below a sediment-water interface with triangular bedforms. *Advances in Water Resources*, *30*(3), 301–313. https://doi.org/10.1016/j.advwatres.2006.06.009

Carling, P. A., Whitcombe, L. J., Benson, I. A., Hankin, B. G., & Radecki-Pawlik, A. M. (2006). A new method to determine interstitial flow patterns in flume studies of sub-aqueous gravel bedforms such as fish nests. *River Research and Applications*, *22*(6), 691–701. https://doi.org/https://doi.org/10.1002/rra.930

Carling, P., Taylor, P., Hankin, B., & Benson, I. (1999). *Fluid Exchange and Oxygen Flux Through Salmonid Redds*. R&D Technical Report W225.

Chapman, D. W. (1988). Critical review of variables used to define effects of fines in redds of large salmonids. *Transactions of the American Fisheries Society*, *52*(8), 567. https://doi.org/10.1097/00006324-197508000-00010

Chapman, D. W., Weitkamp, D. E., Welsh, T. L., Dell, M. B., & Schadt, T. H. (1986). Effects of River Flow on the Distribution of Chinook Salmon Redds. *Transactions of the American Fisheries Society*, *115*(4), 537–547. https://doi.org/10.1577/1548-8659(1986)115<537:eorfot>2.0.co;2

Chen, X., Cardenas, M. B., & Chen, L. (2015). Three-dimensional versus two-dimensional bed form-induced hyporheic exchange. *Water Resources Research*, *51*(4), 2923–2936. https://doi.org/https://doi.org/10.1002/2014WR016848

Coble, D. W. (1961). Influence of water exchange and dissolved oxygen in redds on survival of steelhead trout embryos. *Transactions of the American Fisheries Society*, *90*(4), 469–474. https://doi.org/https://doi.org/10.1577/1548-8659(1961)90[469:IOWEAD]2.0.CO;2

Cooper, A. C. (1965). The effect of transported stream sediments on the survival of sockeye and pink salmon eggs and alevins. Int. Pac. *Salmon Fishery Commission Bulletin Bulletin*, *18*, 18.

Cooper, J. R., & Tait, S. J. (2009). Water-worked gravel beds in laboratory flumes – a natural analogue? *Earth Surface Processes and Landforms*, *34*, 613–628. https://doi.org/10.1002/esp.1743

Crisp, D. T., & Carling, P. A. (1989). Observations on siting, dimensions, and structure of salmonid redds. *Journal of Fish Biology*, *34*, 119–134.

Deverall, K. R., Kelso, J. R. M., & James, G. D. (1993). Redd characteristics and implications for survival of chinook salmon (Oncorhynchus tshawytscha) embryos in the Waitaki river, New Zealand. *New Zealand Journal of Marine and Freshwater Research*, *27*(4), 437–444. https://doi.org/10.1080/00288330.1993.9516585

DeVries, P. (1997). Riverine salmonid egg burial depths: Review of published data and implications for scour studies. *Canadian Journal of Fisheries and Aquatic Sciences*, *54*(8), 1685–1698. https://doi.org/10.1139/f97-090

DeVries, P. (2012). Salmonid influences on rivers: A geomorphic fish tail. *Geomorphology*, *157–158*, 66–74. https://doi.org/10.1016/j.geomorph.2011.04.040

Dudunake, T., Tonina, D., Reeder, W. J., & Monsalve, A. (2020). Local and reach-scale hyporheic flow response from boulder-induced geomorphic changes. *Water Resources Research*, *56*(10). https://doi.org/10.1029/2020WR027719

Dutta, R., & Xing, T. (2018). *Five-equation and robust three-equation methods for solution verification of large eddy simulation*. 23–33.

Elliott, A. H. (1990). *Transfer of solutes into and out of streambeds*. WM Keck Laboratory of Hydraulics and Water Resources, Calif. Inst. of Technol.

Elliott, A. H., & Brooks, N. H. (1997a). Transfer of nonsorbing solutes to a streambed with bed forms: laboratory experiments. *Water Resources Research*, *33*(1), 137–151.

Elliott, A. H., & Brooks, N. H. (1997b). Transfer of nonsorbing solutes to a streambed with bed forms: Theory. *Water Resources Research*, *33*(1), 123–136. https://doi.org/10.1029/96WR02784

Elliott, J. M. (1984). Numerical changes and population regulation in young migratory trout salmo trutta in a lake district stream , 1966-83. *Journal of Animal Ecology*, *53*(1), 327–350. https://www.jstor.org/stable/4360

Evenson, D. F. (2001). *Egg pocket depth and particle size composition within chinook salmon redds in the trinity river*. Humboldt State University.

Fehlman, H. M. (1985). *Resistance Components and Velocity Distributions of Open Channel Flows Over Bedforms*.

Fox, A., Laube, G., Schmidt, C., Fleckenstein, J. H., & Arnon, S. (2016). The effect of losing and gaining flow conditions on hyporheic exchange in heterogeneous streambeds. *Water Resources Research*, *52*(9), 7460–7477. https://doi.org/10.1002/2016WR018677

Geist. (2005a). A conceptual spawning habitat model to aid in ESA recovery plans for snake river fall chinook salmon. *BPA Report DOE/BP*, *00000652–2*(September), i–iii, 1–16.

Geist, D. R. (2000). Hyporheic discharge of river water into fall chinook salmon (Oncorhynchus. *Methods*.

Geist, D. R. (2005b). *Conceptual spawning habitat model to aid in ESA recovery plans for Snake River fall Chinook salmon*. Bonneville Power Administration.

Geist, & Dauble, D. D. (1998). Redd site selection and spawning habitat use by fall chinook salmon: The importance of geomorphic features in large rivers. *Environmental Management*, *22*(5), 655–669. https://doi.org/10.1007/s002679900137

Gottesfeld, A. S., Hassan, M. A., Tunnicliffe, J. F., & Poirier, R. W. (2004). Sediment dispersion in salmon spawning streams: The influence of floods and salmon redd construction. *Journal of the American Water Resources Association*, *40*(4), 1071–1086. https://doi.org/10.1111/j.1752-1688.2004.tb01068.x

Greig, S. M., Sear, D. A., & Carling, P. A. (2005). The impact of fine sediment accumulation on the survival of incubating salmon progeny: Implications for sediment management. *Science of the Total Environment*, *344*(1–3), 241–258. https://doi.org/https://doi.org/10.1016/j.scitotenv.2005.02.010

Greig S. M., Sear D. A., & Carling, P. A. (2006). A review of factors influencing the availability of dissolved oxygen to incubating salmonid embryos. *Hydrological Processes*, *21*, 323–334. https://doi.org/10.1002/hyp.6188 A

Greig, S., Sear, D., & Carling, P. (2007). A field-based assessment of oxygen supply to incubating Atlantic salmon (Salmo salar) embryos. *Hydrological Processes*, *21*(22), 3087–3100. https://doi.org/10.1002/hyp.6635

Groot, C., & Margolis, L. (1991). *Pacific salmon life histories*. Columbia Press.

Hanrahan, T. P., Geist, D. R., & Arntzen, E. V. (2005). Habitat quality of historic snake river fall chinook salmon spawning locations and implications for incubation survival part 1: Substrate quality. *River Research and Applications*, *21*(5), 455–467. https://doi.org/10.1002/rra.823

Harrison, L. R., Bray, E., Overstreet, B., Legleiter, C. J., Brown, R. A., Merz, J. E., Bond, R. M., Nicol, C. L., & Dunne, T. (2019). Physical Controls on Salmon Redd Site Selection in Restored Reaches of a Regulated, Gravel-Bed River. *Water Resources Research*, *55*(11), 8942–8966. https://doi.org/10.1029/2018WR024428

Hassan, M. A., Gottesfeld, A. S., Montgomery, D. R., Tunnicliffe, J. F., Clarke, G. K. C., Wynn, G., Jones-Cox, H., Poirier, R., MacIsaac, E., Herunter, H., & Macdonald, S. J. (2008). Salmon-driven bed load transport and bed morphology in mountain streams. *Geophysical Research Letters*, *35*(4), 1–6. https://doi.org/10.1029/2007GL032997

Hassan, M. A., Tonina, D., & Buxton, T. H. (2015). Does small-bodied salmon spawning activity enhance streambed mobility? *Water Resources Research*, *51*(9), 7467–7484. https://doi.org/10.1002/2015WR017079

Hawke, S. P. (1978). Stranded redds of quinnat salmon in the mathias river, South Island, New Zealand. *New Zealand Journal of Marine and Freshwater Research*, *12*(2), 167–171. https://doi.org/10.1080/00288330.1978.9515737

Hendry, A. P., Morbey, Y. E., Berg, O. K., & Wenburg, J. K. (2004). Adaptive variation in senescence: Reproductive lifespan in a wild salmon population. *Proceedings of the Royal Society B: Biological Sciences*, *271*(1536), 259–266. https://doi.org/10.1098/rspb.2003.2600

Heritage, G. L., & Milan, D. J. (2009). Terrestrial laser scanning of grain roughness in a gravel-bed river. *Geomorphology*, *113*(1–2), 4–11. https://doi.org/10.1016/j.geomorph.2009.03.021

Hervant, F., & Malard, F. (1999). Oxygen supply and the adaptations of animals in groundwater. *Freshwater Biology*, *41*(1), 1–30. https://doi.org/10.1046/j.1365-2427.1999.00379.x

Heyrani, M., Mohammadian, A., Nistor, I., & Dursun, O. F. (2021). Numerical modeling of venturi flume. *Hydrology*, *8*(1), 1–17. https://doi.org/10.3390/hydrology8010027

Hirt, C. W., & Nichols, B. D. (1981). Volume of fluid (VOF) method for the dynamics of free boundaries. *Journal of Computational Physics*, *39*, 201–225.

Huettel, M., & Gust, G. (1992). Impact of bioroughness on interfacial solute exchange in permeable sediments. *Marine Ecology Progress Series*, *89*(2–3), 253–267. https://doi.org/10.3354/meps089253

Janssen, F., Cardenas, M. B., Sawyer, A. H., Dammrich, T., Krietsch, J., & De Beer, D. (2012). A comparative experimental and multiphysics computational fluid dynamics study of coupled surface-subsurface flow in bed forms. *Water Resources Research*, *48*(8), 1–16. https://doi.org/10.1029/2012WR011982

Keulegan, G. H. (1938). Laws of turbulent flow in open channels. *Journal of Research of the National Bureau of Standards*, *21*(6), 707. https://doi.org/10.6028/jres.021.039

Kocaer, Ö., & Yarar, A. (2020). *Experimental and Numerical Investigation of Flow Over Ogee Spillway*. 3949–3965.

Kondolf, G. M. (2000). Assessing salmonid spawning gravel quality. *Transactions of the American Fisheries Society*, *129*(1), 262–281. https://doi.org/10.1577/1548-8659(2000)129<0262:assgq>2.0.co;2

Kondolf, G. M., & Wolman, M. G. (1993). The sizes of salmonid spawning gravels. *Water Resources Research*, *29*(7), 2275–2285. https://doi.org/10.1029/93WR00402

Launder, B. E., & Spalding, D. B. (1974). The Numerical Computation of Turbulent Flow Computer Methods. *Computer Methods in Applied Mechanics and Engineering*, *3*(March 1974), 269–289.

Lee, A., Aubeneau, A. F., & Cardenas, M. B. (2020). The sensitivity of hyporheic exchange to fractal properties of riverbeds. *Water Resources Research*, *56*(5), 1–15. https://doi.org/10.1029/2019WR026560

Lee, A., Aubeneau, A., Liu, X., & Cardenas, M. B. (2021). Hyporheic Exchange in Sand Dunes Under a Freely Deforming River Water Surface. *Water Resources Research*, *57*(3), 1–13. https://doi.org/10.1029/2020WR028817

Maekawa, K., & Hino, T. (1990). Spawning tactics of female Miyabe charr (Salvelinus malma miyabei) against egg cannibalism. *Canadian Journal of Zoology*, *68*(5), 889–894. https://doi.org/10.1139/z90-129

Malcolm, I. A., Soulsby, C., Youngson, A. F., Hannah, D. M., McLaren, I. S., & Thorne, A. (2004). Hydrological influences on hyporheic water quality implications for salmon egg survival. *Hydrological Processes*, *18*(9), 1543–1560. https://doi.org/10.1002/hyp.1405

Martin, B. T., Dudley, P. N., Kashef, N. S., Stafford, D. M., Reeder, W. J., Tonina, D., Del Rio, A. M., Scott Foott, J., & Danner, E. M. (2020). The biophysical basis of thermal tolerance in fish eggs: Thermal tolerance in fish eggs. *Proceedings of the Royal Society B: Biological Sciences*, *287*(1937).

https://doi.org/https://doi.org/10.1098/rspb.2020.1550

Martin, B. T., Pike, A., John, S. N., Hamda, N., Roberts, J., Lindley, S., & Danner, E. M. (2017). Phenomenological vs. biophysical models of thermal stress in aquatic eggs. *Ecology Letters*, *20*(1), 50–59.

Martins Segunda, V., Ormiston, S. J., & Tachie, M. F. (2018). Experimental and numerical investigation of developing turbulent flow over a wavy wall in a horizontal channel. *European Journal of Mechanics, B/Fluids*, *68*, 128–143. https://doi.org/10.1016/j.euromechflu.2017.12.001

Maturana, O., Tonina, D., McKean, J. A., Buffington, J. M., Luce, C. H., & Caamaño, D. (2013). Modeling the effects of pulsed versus chronic sand inputs on salmonid spawning habitat in a low-gradient gravel-bed river. *Earth Surface Processes and Landforms*, *39*(7), 877–889. https://doi.org/10.1002/esp.3491

McNeil, W. J., & Ahnell, W. H. (1964). Success of pink salmon spawning relative to size of spawning bed materials. *US Fish and Wildlife Service, Special Scientific Report-Fisheries No. 469*, *157*, 1–15. http://spfgtsn.krisweb.com/biblio/gen_usfws_mcneiletal_1964.pdf

Mendoza, C., & Zhou, D. (1992). Effects of porous bed on turbulent stream flow above bed. *Journal of Hydraulic Engineering*, *118*(9), 1222–1240.

Menter, F. R. (1994). Two-equation eddy-viscosity turbulence models for engineering applications. *AIAA Journal*, *32*(8), 1598–1605. https://doi.org/10.2514/3.12149

Menter, F. R. (2009). Review of the shear-stress transport turbulence model experience from an industrial perspective. *International Journal of Computational Fluid Dynamics*, *23*(4), 305–316. https://doi.org/10.1080/10618560902773387

Menter, F. R., & Egorov, Y. (2010). *The Scale-Adaptive Simulation Method for Unsteady Turbulent Flow Predictions . Part 1 : Theory and Model Description*. 113–138. https://doi.org/10.1007/s10494-010-9264-5

Merz, J. E., Setka, J. D., Pasternack, G. B., & Wheaton, J. M. (2004). Predicting benefits of spawning-habitat rehabilitation to salmonid (Oncorhynchus spp.) fry production in a regulated California river. *Canadian Journal of Fisheries and Aquatic Sciences*, *61*(8), 1433–1446. https://doi.org/10.1139/F04-077

Meselhe, E. A., & Odgaard, A. J. (1998). 3D Numerical Flow Model for Fish Diversion

    Studies at Wanapum Dam. *Journal of Hydraulic Engineering*, *124*(12), 1203–1214.

    https://doi.org/10.1061/(asce)0733-9429(1998)124:12(1203)

Mohotti, D., Wijesooriya, K., & Dias-da-costa, D. (2019). Comparison of Reynolds

    Averaging Navier-Stokes (RANS) turbulent models in predicting wind pressure on tall

    buildings. *Journal of Building Engineering*, *21*(March 2018), 1–17.

    https://doi.org/10.1016/j.jobe.2018.09.021

Monofy, A., & Boano, F. (2021). The Effect of Streamflow, Ambient Groundwater, and

    Sediment Anisotropy on Hyporheic Zone Characteristics in Alternate Bars. *Water

    Resources Research*, *57*(1), 1–22. https://doi.org/10.1029/2019WR025069

Monsalve, A., & Yager, E. M. (2017). Bed Surface Adjustments to Spatially Variable Flow

    in Low Relative Submergence Regimes. *Water Resources Research*, *53*(11), 9350–

    9367. https://doi.org/10.1002/2017WR020845

Monsalve, A., Yager, E. M., & Schmeeckle, M. W. (2017). Effects of Bed Forms and Large

    Protruding Grains on Near-Bed Flow Hydraulics in Low Relative Submergence

    Conditions. *Journal of Geophysical Research: Earth Surface*, *122*(10), 1845–1866.

    https://doi.org/10.1002/2016JF004152

Montgomery, D. R., Buffington, J. M., Peterson, N. P., Schuett-Hames, D., & Quinn, T. P.

    (1996). Stream-bed scour, egg burial depths, and the influence of salmonid spawning on

    bed surface mobility and embryo survival. *Canadian Journal of Fisheries and Aquatic

    Sciences*, *53*(5), 1061–1070. https://doi.org/10.1139/f96-028

Moreto, J. R., Reeder, W. J., Budwig, R., Tonina, D., & Liu, X. (2022). Experimentally Mapping Water Surface Elevation, Velocity, and Pressure Fields of an Open Channel Flow Around a Stalk. *Geophysical Research Letters*, *49*(7), 1–10. https://doi.org/10.1029/2021gl096835

Moriasi, D. N., Arnold, J., Van Liew, M., Bingner, R., Harmel, D., & Veith, T. (2007). Model evaluation guidelines for systematic quantification of accuracy in watershed simulations. *Transactions of the American Society of Agricultural and Biological Engineers*, *50*(3), 885–900.

Mueller, R. (2005). *Deepwater Spawning of Fall Chinook Salmon (Oncorhynchus tshawytscha) near Ives and Pierce Island of the Columbia River, 2004-2005 Annual Report, Project No. 199900301*.

Nikora, V. I., Goring, D. G., & Biggs, B. J. F. (1998). *On gravel-bed roughness characterization*. *34*(3), 517–527.

Patankar, S. (1980). Numerical heat transfer and fluid flow: Computational methods in mechanics and thermal science. In *Hemisphere Publication Corporation, Washington, DC* (pp. 1–197).

Peterson, N. P., & Quinn, T. P. (1996). Persistence of egg pocket architecture in redds of chum salmon, Oncorhynchus keta. *Environmental Biology of Fishes*, *46*(3), 243–253. https://doi.org/https://doi.org/10.1007/BF00004999

Rahimzadeh, H., Maghsoodi, R., Sarkardeh, H., & Tavakkol, S. (2012). Simulating flow over circular spillways by using different turbulence models. *Engineering Applications of Computational Fluid Mechanics*, *6*(1), 100–109. https://doi.org/10.1080/19942060.2012.11015406

Reeder, W. J. J., Quick, A. M. A. M., Farrell, T. B. T. B., Benner, S. G. S. G., Feris, K. P. K. P., & Tonina, D. (2018). Spatial and Temporal Dynamics of Dissolved Oxygen Concentrations and Bioactivity in the Hyporheic Zone. *Water Resources Research*, *54*(3), 2112–2128. https://doi.org/10.1002/2017WR021388

Reidenbach, M. A., Limm, M., Hondzo, M., & Stacey, M. T. (2010). Effects of bed roughness on boundary layer mixing and mass flux across the sediment-water interface. *Water Resources Research*, *46*(7). https://doi.org/10.1029/2009WR008248

Riebe, C. S., Sklar, L. S., Overstreet, B. T., & Wooster, J. K. (2014). Optimal reproduction in salmon spawning substrates linked to grain size and fish length. *Water Resources Research*, *50*(2), 898–918. https://doi.org/10.1002/2013WR014231

Roche, K. R., Blois, G., Best, J. L., Christensen, K. T., Aubeneau, A. F., & Packman, A. I. (2018). Turbulence Links Momentum and Solute Exchange in Coarse-Grained Streambeds. *Water Resources Research*, *54*(5), 3225–3242. https://doi.org/10.1029/2017WR021992

Shih, T.-H., Liou, W., Shabbir, A., Yang, Z., & Zhu, J. (1995). A new k-ε eddy viscosity model for high reynolds number turbulent flows. *Computers & Fluids*, *24*(3), 227–238. https://doi.org/https://doi.org/10.1016/0045-7930(94)00032-T

Simsek, O., Akoz, M. S., & Soydan, N. G. (2016). Numerical validation of open channel flow over a curvilinear broad-crested weir. *Progress in Computational Fluid Dynamics*, *16*(6), 364. https://doi.org/10.1504/pcfd.2016.10000916

Smart, G., Aberle, J., Duncan, M., & Walsh, J. (2004). Measurement and analysis of alluvial bed roughness. *Journal of Hydraulic Research*, *42*(3), 227–237. https://doi.org/10.1080/00221686.2004.9728388

Soulsby, C., Malcolm, I. A., & Youngson, A. F. (2001a). Hydrochemistry of the hyporheic zone in salmon spawning gravels: a preliminary assessment in a degraded agricaltural stream. *Regulated Rivers: Research & Management*, *17*(6), 651–665.

Soulsby, C., Malcolm, I. A., & Youngson, A. F. (2001b). Hydrochemistry of the hyporheic zone in salmon spawning gravels: A preliminary assessment in a degraded agricultural stream. *River Research and Applications*, *17*(6), 651–665. https://doi.org/10.1002/rrr.625

Soulsby, C., Youngson, A. F., Moir, H. J., & Malcolm, I. A. (2001). Fine sediment influence on salmonid spawning habitat in a lowland agricultural stream: a preliminary assessment. *Science of The Total Environment*, *265*(1–3), 295–307. https://doi.org/10.1016/S0048-9697(00)00672-0

Stonedahl, S. H., Harvey, J. W., Wörman, A., Salehin, M., & Packman, A. I. (2010). A multiscale model for integrating hyporheic exchange from ripples to meanders. *Water Resources Research*, *46*(12), 1–14. https://doi.org/10.1029/2009WR008865

Stuart, T. A. (1953a). Spawning migration, reproduction and young stage of loch trout (Salmo trutta L.). In *Freshwater and Salmon Fisheries Research*. Department of Agriculture and Fisheries.

Stuart, T. A. (1953b). Water currents through permeable gravel and their significance to spawning salmonids, etc. *Nature*, *172*, 407–408.

Tappel, P. D., & Bjornn, T. C. (1983). A new method of relating size of spawning gravel to salmonid embryo survival. *North American Journal of Fisheries Management*, *3*(2), 123–135. https://doi.org/10.1577/1548-8659(1983)3<123:anmors>2.0.co;2

Tonina, D., & Buffington, J. M. (2009a). A three-dimensional model for analyzing the effects of salmon redds on hyporheic exchange and egg pocket habitat. *Canadian Journal of Fisheries and Aquatic Sciences*, *66*(12), 2157–2173. https://doi.org/10.1139/F09-146

Tonina, D., & Buffington, J. M. (2009b). Hyporheic exchange in mountain rivers I: Mechanics and environmental effects. *Geography Compass*, *3*(3), 1063–1086. https://doi.org/10.1111/j.1749-8198.2009.00226.x

Tonina, D., & Buffington, J. M. (2009c). Hyporheic exchange in mountain rivers II: Effects of Channel Morphology on Mechanics, Scales, and Rates of Exchange. *Geography Compass*, *3*(3), 1038–1062. https://doi.org/https://doi.org/10.1111/j.1749-8198.2009.00225.x

Tonina, D., & Buffington, J. M. (2009d). A three-dimensional model for analyzing the effects of salmon redds on hyporheic exchange and egg pocket habitat. *Canadian Journal of Fisheries and Aquatic Sciences*, *66*(12), 2157–2173. https://doi.org/https://doi.org/10.1139/F09-146

Tonina, D., & Jorde, K. (2013). Hydraulic Modelling Approaches for Ecohydraulic Studies: 3D, 2D, 1D and Non-Numerical Models. In *Ecohydraulics* (pp. 31–74). John Wiley & Sons, Ltd. https://doi.org/10.1002/9781118526576.ch3

Trauth, N., Schmidt, C., Maier, U., Vieweg, M., & Fleckenstein, J. H. (2013). Coupled 3-D stream flow and hyporheic flow model under varying stream and ambient groundwater flow conditions in a pool-riffle system. *Water Resources Research*, *49*(9), 5834–5850. https://doi.org/10.1002/wrcr.20442

Van Den Berghe, E. P., & Gross, M. R. (1984). Female size and nest depth in coho salmon (Oncorhynchus kisutch). *Canadian Journal of Fisheries and Aquatic Sciences*, *41*(1), 204–206. https://doi.org/10.1139/f84-022

Versteeg, H. K., & Malalasekera, W. (1995). *An Introduction to Computational Fluid Dynamics: The Finite Volume Method*. Prentice Hall.

Wang, X., Mohammadian, A., & Rennie, C. D. (2022). Influence of Negatively Buoyant Jets on a Strongly Curved Open-Channel Flow Using RANS Models with Experimental Data. *Water (Switzerland)*, *14*(3). https://doi.org/10.3390/w14030347

Whiting, P. J., & Dietrich, W. E. (1991). Convective accelerations and boundary shear stress over a Channel Bar. *Water Resources Research*, *27*(5), 783–796. https://doi.org/10.1029/91WR00083

Wiberg, P. L., & Smith, J. D. (1991). Velocity distribution and bed roughness in high-gradient streams. *Water Resources Research*, *27*(5), 825–838. https://doi.org/10.1029/90WR02770

Wilcox, D. C. (1998). *Turbulence Modeling for CFD* (3rd ed.). DCW Industries, Inc. La
  Canada, California.

Wilcox, D. C. (2008). Formulation of the k-ω turbulence model revisited. *AIAA Journal*,
  46(11), 2823–2838. https://doi.org/10.2514/1.36541

Wilson, R. V., Stern, F., Coleman, H. W., & Paterson, E. G. (2001). Comprehensive
  approach to verification and validation of CFD simulations—Part 2: Application for
  rans simulation of a cargo/container ship. *Journal of Fluids Engineering, Transactions
  of the ASME*, *123*(4), 803–810. https://doi.org/10.1115/1.1412236

Wörman, A., Packman, A. I., Marklund, L., Harvey, J. W., & Stone, S. H. (2007). Fractal
  topography and subsurface water flows from fluvial bedforms to the continental shield.
  Geophysical Research Letters, *34*(7), 1–5. https://doi.org/10.1029/2007GL029426

Xing, T. (2015). A general framework for verification and validation of large eddy
  simulations. *Journal of Hydrodynamics*, *27*(2), 163–175. https://doi.org/10.1016/S1001-
  6058(15)60469-3

Xing, T., Carrica, P., & Stern, F. (2008). Computational towing tank procedures for single
  run curves of resistance and propulsion. *Journal of Fluids Engineering*, *130*(10), 101102
  (14 pages). https://doi.org/10.1115/1.2969649

Xing, T., Matveev, K. I., & Wheeler, M. P. (2020). Numerical study of high-lift hydrofoil
  near free surface at moderate Froude number. *Journal of Hydrodynamics*, *32*(1), 44–53.
  https://doi.org/10.1007/s42241-019-0095-0

Xing, T., & Stern, F. (2010). Factors of safety for Richardson extrapolation. *Journal of Fluids Engineering, Transactions of the ASME*, *132*(6), 061403 (13 pages). https://doi.org/10.1115/1.4001771

Xing, T., & Stern, F. (2011). Closure to "discussion of 'factors of safety for Richardson Extrapolation'" (2011, ASME J. Fluids Eng., 133, p. 115501). *Journal of Fluids Engineering, Transactions of the ASME*, *133*(11), 115502 (6 pages). https://doi.org/10.1115/1.4005030

Yates, D., Galbraith, H., Purkey, D., Huber-Lee, A., Sieber, J., West, J., Herrod-Julius, S., & Joyce, B. (2008). Climate warming, water storage, and Chinook salmon in California's Sacramento Valley. *Climatic Change*, *91*(3–4), 335–350. https://doi.org/10.1007/s10584-008-9427-8

Yorke, C. P., & Coleman, G. N. (2004). Assessment of common turbulence models for an idealised adverse pressure gradient flow. *European Journal of Mechanics, B/Fluids*, *23*(2), 319–337. https://doi.org/10.1016/j.euromechflu.2003.07.002

Yu, S., Dai, H., Zhai, Y., Liu, M., & Huai, W. (2022). A Comparative Study on 2D CFD Simulation of Flow Structure in an Open Channel with an Emerged Vegetation Patch Based on Different RANS Turbulence Models. *Water (Switzerland)*, *14*(18). https://doi.org/10.3390/w14182873

Zhou, D., & Mendoza, C. (1993). Flow through porous bed of turbulent stream. *Journal of Engineering Mechanics*, *119*(2), 365–383.

Zhou, J. yin, Shao, X. jun, Wang, H., & Jia, D. dong. (2017). Assessment of the predictive

capability of RANS models in simulating meandering open channel flows. *Journal of*

Hydrodynamics, *29*(1), 40–51. https://doi.org/10.1016/S1001-6058(16)60714-X

Zimmermann, A. E., & Lapointe, M. (2005a). Intergranular flow velocity through salmonid

redds: Sensitivity to fines infiltration from low intensity sediment transport events. *River*

Research and Applications, *21*(8), 865–881. https://doi.org/10.1002/rra.856

Zimmermann, A. E., & Lapointe, M. F. (2005b). Sediment infiltration traps: Their use to

monitor salmonid spawning habitat in headwater tributaries of the Cascapédia River,

Québec. *Hydrological Processes*, *19*(20), 4161–4177. https://doi.org/10.1002/hyp.5879
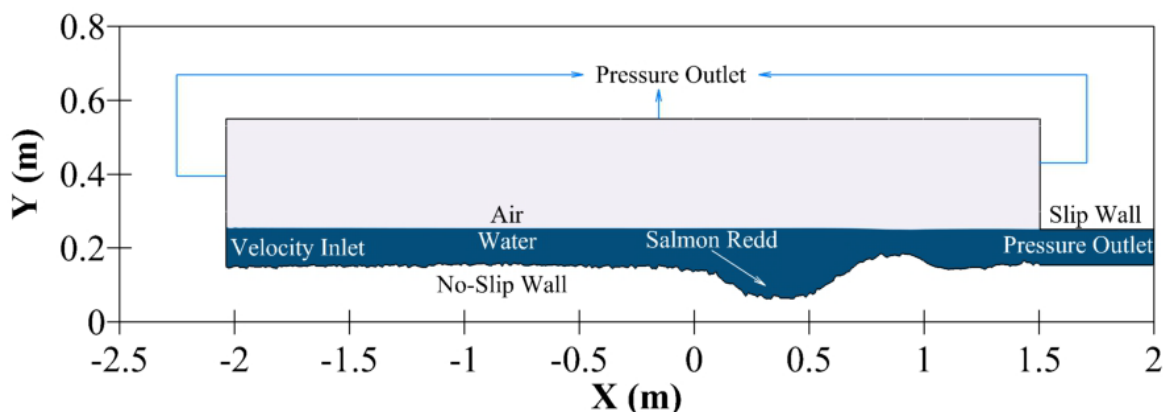
Appendix

Figure S1: Similar to figure 20a, but with the complete simulation domain, illustrating air (colored in grey) and water (colored in blue) along with the boundary conditions.
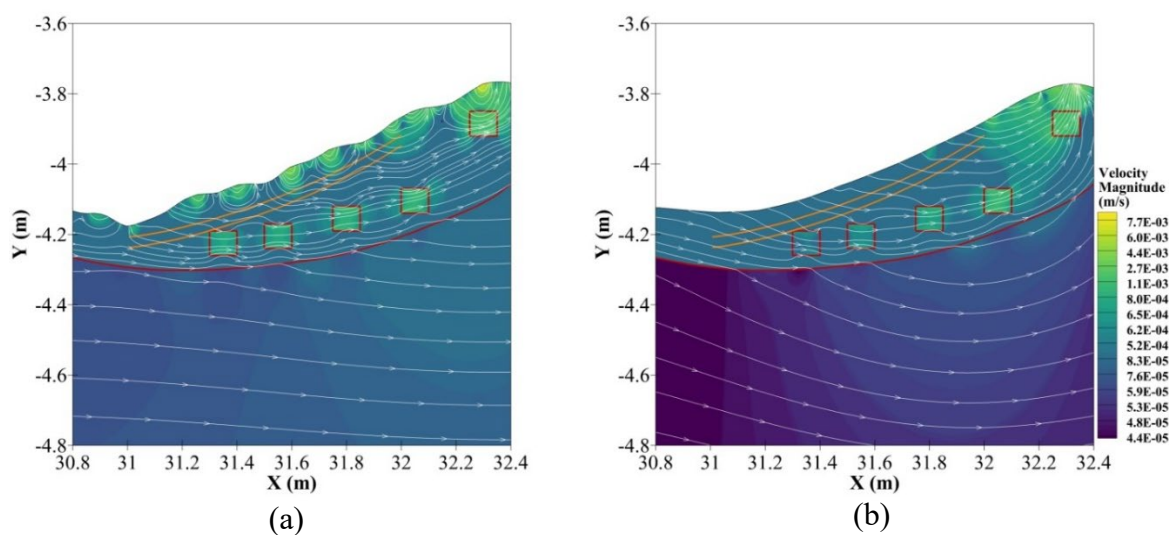

(a)   (b)

Figure S2: Subsurface flow characteristics for redds with the roughness of σ_E =13.3 mm. (a) R_1 and (b) R_2 with five egg pockets situated inside the redds. The orange curves indicate the locations at which downwelling fluxes are extracted at 2 times (top) and 3 times the D_{50} of a 3 cm rough waterbed. Flow is from left to right.